# Fabrication and characterization of a hybrid quantum device for single spin microwave detection

Jéssica Fernanda Da Silva Barbosa

Thèse de doctorat

NNT : 2020UPASP003

université PARIS-SACLAY

# Fabrication and characterization of a hybrid quantum device for single spin microwave detection

**Thèse de doctorat de l'université Paris-Saclay**

École doctorale n°564 : physique en l'Ile-de-France (PIF)

Spécialité de doctorat : Physique
Unité de recherche : Service de Physique de l'Etat Condensé, Université Paris-Saclay, CEA, CNRS, 91191 Gif-sur-Yvette
Référent : Faculté des sciences d'Orsay

**Thèse présentée et soutenue à Paris-Saclay, le 28 août 2020, par**

**Jéssica Fernanda DA SILVA BARBOSA**

## Composition du Jury

| | |
|---|---|
| **Jean-François ROCH**<br>Professeur, Laboratoire Aimé Cotton | Président |
| **Fedor JELEZKO**<br>Professeur, Ulm University | Rapporteur et examinateur |
| **Franck BALESTRO**<br>Maître de conférences (HDR), Institut NEEL | Rapporteur et examinateur |
| **Diana SERRANO**<br>Chercheuse CNRS, Institut de Recherche de Chimie Paris-Chimie ParisTech | Examinatrice |
| **Patrice BERTET**<br>Directeur de recherche, SPEC - CEA/Université Paris-Saclay | Directeur de thèse |
| **Reinier HEERES**<br>Ingénieur, SPEC – CEA/Université Paris-Saclay | Co-encadrant |

*Para Célia, João e Vítor*: saudades...
*Per Andrea*: *Έρως ανίκατε μάχαν*...
*To our Miguelito!*

# Acknowledgements

These years spent on Quantronics was an amazing experience on both personal life and carrier and here I would like to thank those who has contributed to this.

First of all, I am deeply grateful for Patrice for the unique opportunity he gave me to participate on an exciting and challenging project, for his continued support, guidance, as well as his optimism, sympathy and kindness.

Thanks to Reinier for his guidance and for teaching me so many notions in a variety of areas ranging from the confocal microscope to Python, always with enthusiasm and a smile! ("It is what it is!"). Thanks Philippe for teaching me several experimental techniques during the initial stage of the project and for your friendly attitude. Thanks also to Moonjoo and Manu (man!) for their contribution on resonator design and fabrication. Thanks Vishal, Marianne (Professora!), Dan, Milos and Leandro for all your help with the fridge stuff and for so many pleasant and stimulating discussions.

I also would like to acknowledge all collaborators for their valuable contributions without which this work would not have been possible: Pierre Jamonneau (Laboratoire Aime Cotton) for the work with the confocal microscope, Teraji Tokuyuki (Namiki, Tsukuba) for the careful growth of $^{12}C$ diamond purified layer on the samples, Sébastien Pezzagna (Leipzig University) for inviting to participate in the nitrogen implantation process, Anne Forget (SPEC) for the NV annealing and José Palomo (ENS) for the optical lithography processing used to fabricate the resonator.

Quantronics has always been an ambient where we feel free to express ourselves, to ask for help and that often organize marvelous gourmet meetings, with delicious cakes, French cheese and wine! A special thank to the permanent members: Daniel, Denis, Cristian, Hugues, Marcelo, Hélène, Philippe J., Pief, Sebastian and Pascal for creating such a friendly atmosphere.

Thanks Bartolo (Professore!) and Emanuele (Grande!) for having taught me Italian and for creating such a friendly and pleasant place! Thanks also to Anil, Nicolas, Cyril, Eric, Léo, Jonas, Imen, Zubair, Ambroise, Maëlle, Ramiro, Sebastian and Audrey for their true friendship and kindness.

Moreover, I would also like to warmly thank Nathalie, Claudine, Nadine, Thomas and Elodie for all the assistance they provided in a professional manner regarding administration, security and logistics, as well as the mechanical and the cryogenic workshops and the SPEC direction.

Finally, I thank my family and friends in Brazil, Italy and France for their support! A special thank to Isa and Peter for all the nice dinners together and to Açaí and the Abadá Capoeira group for the amazing trainings and for the friendly atmosphere. Thank you, Andrea, for always bringing me happiness and lovely risotti (or ravioli Rana)!

# Contents

**Acknowledgements** **v**

**Résumé détaillé** **1**

**1 Introduction** **7**

**2 Proposal for detecting a single spin with microwaves** **13**
2.1 Single spin detection: state-of-art . . . . . 13
2.2 Dynamics of a spin driven by a classical field . . . . . 14
2.3 Coupling of a spin to a quantized microwave field . . . . . 18
2.4 Single spin detection proposal . . . . . 19

**3 NV centers in diamond** **25**
3.1 Structure and charge state . . . . . 25
3.2 Ground state electron spin energy levels . . . . . 27
3.3 Optical transitions and ODMR . . . . . 29
3.4 Room temperature setup . . . . . 30
3.5 Hyperfine interaction . . . . . 33
3.6 Magnetometry using NV centers . . . . . 37
3.7 Relaxation times . . . . . 40
3.8 Shallow NV centers and charge state stability . . . . . 41

**4 Realization of an array of precisely placed NV centers with long coherence times** **43**
4.1 Alignment strategy . . . . . 43
4.2 Fabrication process . . . . . 44
4.3 The substrate . . . . . 45
4.4 NV implantation . . . . . 46
4.5 Annealing . . . . . 50
4.6 Sample cleaning . . . . . 50
4.7 Experimental setup . . . . . 51
4.8 Characterization at room temperature . . . . . 53
4.9 Annealing and PL stability . . . . . 56
4.10 Small ensembles of NV center . . . . . 56
4.11 Substrate microwave losses . . . . . 59

**5 Measuring the position of a spin relative to a nanowire** **61**
5.1 Principle of the experiment . . . . . 61
5.2 Nanowire fabrication . . . . . 63

5.3 Measurements at room temperature . . . . . 66
5.4 Analysis . . . . . 69
5.5 Final comments . . . . . 72

**6 The resonator** **73**
6.1 Introduction . . . . . 73
6.2 Design and electromagnetic simulations . . . . . 74
6.3 Resonator fabrication . . . . . 75
6.4 Low temperature characterization . . . . . 76

**7 Conclusions and perspectives** **83**
7.1 Actual state of the project . . . . . 83
7.2 Future directions . . . . . 84

**A** **85**
A.1 Fabrication Recipies . . . . . 85
A.2 Analytical expression of the magnetic field generated by infinite wire with rectangular cross section . . . . . 86
A.3 Vector magnetometry of NV2 and NV3 . . . . . 87

# Résumé détaillé

La spectroscopie par résonance magnétique permet une compréhension approfondie de la matière et de sa structure au niveau atomique. Son application est partout dans notre vie quotidienne, tout particulièrement dans les sciences de la vie et la médecine. La spectroscopie de résonance de spin électronique (ESR) [1] est une branche de la résonance magnétique qui détecte les spins d'électrons non appariés. Elle est largement utilisée en biologie moléculaire, en science des matériaux et en chimie pour analyser les structures paramagnétiques et pour caractériser des produits et des molécules, comprendre leur structure et leurs propriétés. Le moyen le plus courant de détecter la spectroscopie ESR consiste à utiliser l'absorption micro-ondes d'un ensemble de spins lorsqu'ils sont accordés en résonance avec un résonateur auquel ils sont couplés, une méthode appelée détection inductive. La spectroscopie ESR est généralement réalisée à température ambiante. Cependant, le bruit thermique associé au faible couplage spin-photon se traduit par une mauvaise sensibilité des spectromètres ESR. En bande X, de l'ordre de $\sim 10^{13}$ spins sont nécessaires pour obtenir un signal suffisant en une seule séquence de mesure.

Il existe une recherche active visant à améliorer la sensibilité de la spectroscopie inductive ESR [2, 3, 4, 5, 6, 7, 8], motivée par le progrès des circuits quantiques supraconducteurs et de l'électrodynamique quantique des circuits (cQED)[9] où la détection haute fidélité des signaux micro-ondes faibles est essentielle pour la mesure et la manipulation des qubits. Des résultats prometteurs ont été obtenus récemment en utilisant les amplificateurs paramétriques Josephson (JPA) [10] dont l'amplification n'ajoute aucun bruit supplémentaire. La spectroscopie ESR à la limite quantique de sensibilité a été rapportée par Bienfait à. al., qui a démontré une sensibilité de 1700 spins / $\sqrt{Hz}$ [6, 11].

À la lumière de cela, il a été théoriquement prédit par Haikka et. al. [12] qu'il devrait être possible d'atteindre une sensibilité suffisante pour détecter un seul spin en combinant des micro-résonateurs supraconducteurs à facteur de haute qualité et des amplificateurs paramétriques Josephson. De plus, il a été montré qu'en optimisant la conception du résonateur supraconducteur, la sensibilité était augmentée jusqu'à 65 spins / $\sqrt{(Hz)}$ [13].

C'est le contexte de cette thèse dont la motivation est de réaliser expérimentalement la proposition [12], c'est-à-dire d'améliorer la spectroscopie ESR vers la limite de la détection de spin unique en médiant le couplage d'un seul spins avec un rayonnement photonique à l'aide d'un LC high résonateur supraconducteur à facteur de qualité.

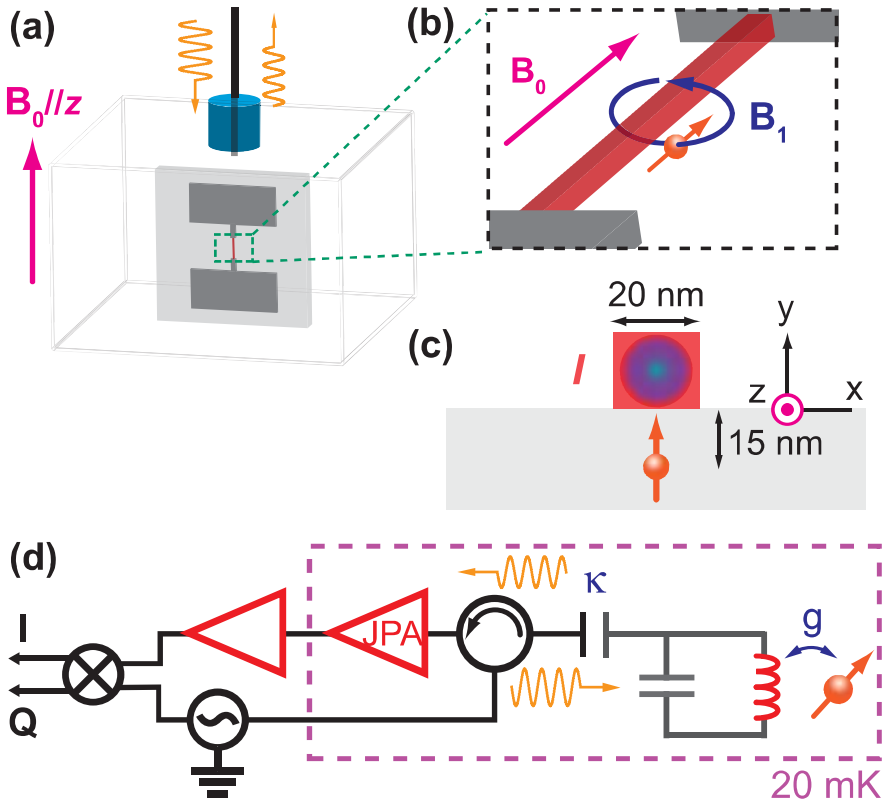


Figure 1: **Configuration proposée**. **a.** Résonateur LC supraconducteur composé de deux plots (condensateur C) et d'un fil (inductance L) placés dans une cavité micro-onde tridimensionnelle. **b.** Constriction à l'échelle nanométrique faite au centre du fil d'inductance, en dessous de laquelle un seul spin est situé à 15 nm. **c.** Coupe transversale de la structure. **d.** Schéma du circuit de mesure considéré. Le signal qui s'échappe de la cavité est d'abord amplifié par un amplificateur paramétrique Josephson limité quantique (JPA), suivi par des amplificateurs cryogéniques à faible bruit HEMT et à température ambiante. [12]

Après un bref résumé de cette thèse dans le premier chapitre, le deuxième chapitre décrit les détails de la proposition [12] et vise à fournir les outils conceptuels nécessaires pour comprendre les mesures. Nous expliquons d'abord les principes de la dynamique de spin pilotée par un champ micro-onde classique, ainsi que les séquences d'impulsions utilisées pour la caractérisation du spin. Ensuite, nous présentons le couplage spin-résonateur hamiltonien. Le paramètre essentiel est la constante de couplage spin-photon $g$. Compte tenu des pertes du résonateur (à un taux $\kappa$), le spin peut émettre spontanément des photons hyperfréquences, via l'effet Purcell. Nous terminons le chapitre en estimant le temps de mesure d'un seul spin couplé à un résonateur

$$T_{meas} = \frac{\kappa^2 \Gamma_2^*}{g^4}, \tag{1}$$

où nous avons considéré l'amplification micro-ondes idéale, et $(\Gamma_2^*)^{-1} \equiv T_2^*$ est le temps de cohérence de spin. Pour des paramètres raisonnables, un temps de mesure inférieur à la milliseconde est réalisable. Cependant, cela nécessite un alignement

précis (de l'ordre de 10 nm) du spin avec un nanofil inséré dans le résonateur, ainsi qu'un temps de cohérence suffisamment long.

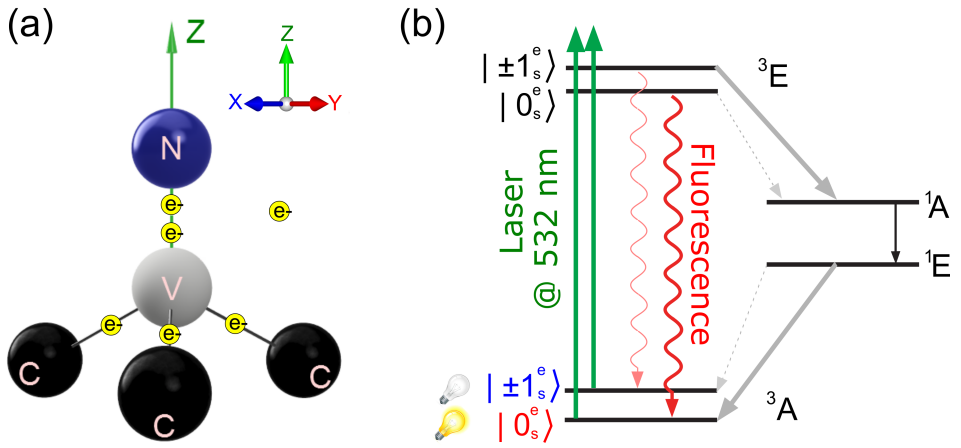


Figure 2: **Système de spin utilisé dans cette thèse. a.** Le schéma de la NV: symétrie trigonale formée par 3 atomes de carbone (noir), 1 atome d'azote (bleu) et la vacance du carbone (blanc). L'axe symétrique, Z, est représenté en vert. En jaune sont représentés les 6 électrons $NV^-$ impliqués dans le système $NV^-$ . **b.** NV illuminée avec un laser vert émet une photoluminescence rouge (PL). ${}^3A_{m_s=0}$ l'excitation conduit à PL après $\sim 12ns$ avec ${}^3A_{m_s=\pm1}$ l'excitation se désintègre très probablement de manière non radiative vers l'état métastable ${}^1A$ résultant en une occupation de $m_s^g = 0$ après $\sim 300\,ns$. La dépendance au spin des relaxations électroniques du spin permet l'initialisation du spin et la lecture à température ambiante.

Le troisième chapitre décrit la physique des centres NV dans le diamant (Fig.1.2a), qui sont le système de spin modèle utilisé dans cette thèse. La spécificité des centres NV dans le diamant est qu'ils peuvent être implantés à des endroits bien définis, et entièrement caractérisés à température ambiante par détection optique de résonance magnétique (ODMR), Fig.1.2b.

Le quatrième chapitre rapporte l'un des principaux résultats de cette thèse. Nous démontrons la fabrication d'un échantillon avec un réseau de centres NV individuels, situés à une position précise par rapport aux marques d'alignement gravées dans le substrat, et avec de longs temps de cohérence (jusqu'à 52 $\mu$s), comme le montre la Fig. 2. Ceci a été obtenu par implantation à travers un masque de résine percé de trous de taille nanométrique.

Nous procédons ensuite en testant notre capacité à aligner précisément un seul centre NV et un nanofil métallique déposé sur le diamant. Pour cela, dans le cinquième chapitre, nous réalisons une expérience où nous utilisons une magnétométrie vectorielle à NV unique pour déterminer a posteriori la position de plusieurs centres NV par rapport à des nanofils d'aluminium à travers lesquels nous passons du courant continu. Nous déterminons la position relative avec une précision $\sim 10$ nm. Nous trouvons un décalage d'ordre systématique 100 nm, malgré tous nos efforts, comme le montre la Fig. 3. Sur la base de ces résultats, nous avons décidé

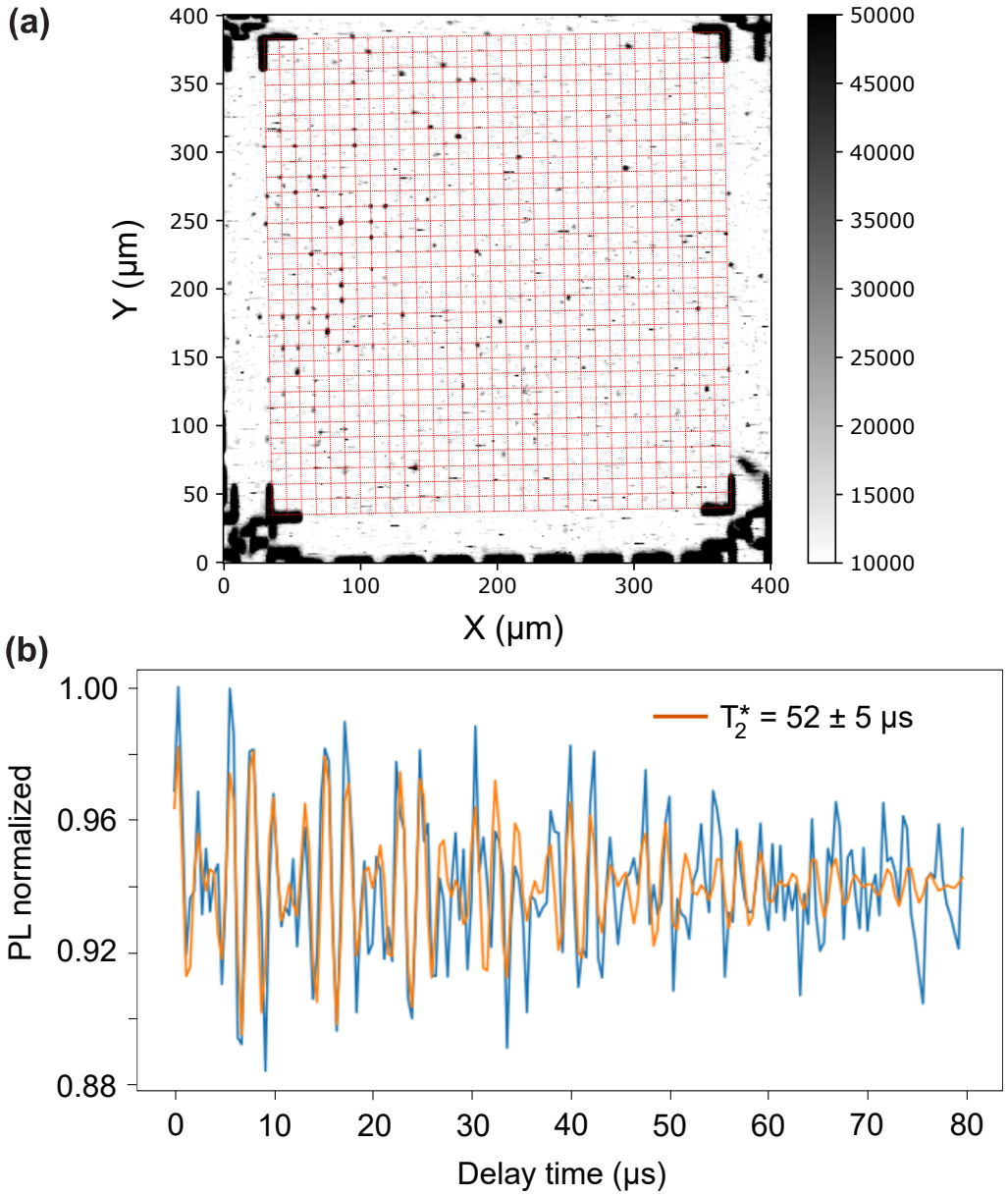


Figure 3: **Réalisation d'un réseau de centres NV placés précisément avec de longs temps de cohérence. a.** Image au microscope confocal d'un seul centre NV. L'échelle de couleur indique le nombre de photons collectés par seconde. **b.** Mesure Ramsey d'une seule NV. $T_2^* = 52\mu s$

de cibler le couplage du résonateur à un petit ensemble de centres NV implantés, où la précision d'alignement est moins critique.

Dans le dernier chapitre de la thèse, nous rendons compte de la conception, de la fabrication et de la caractérisation du résonateur à des températures millikelvin. Le taux de perte du résonateur est suffisamment faible pour réaliser l'expérience envisagée, comme le montre la Fig. 4. Malheureusement, la résilience du champ magnétique du résonateur était insuffisante pour régler la NV avec le résonateur; en conséquence, le signal de spin n'a pas été mesuré.

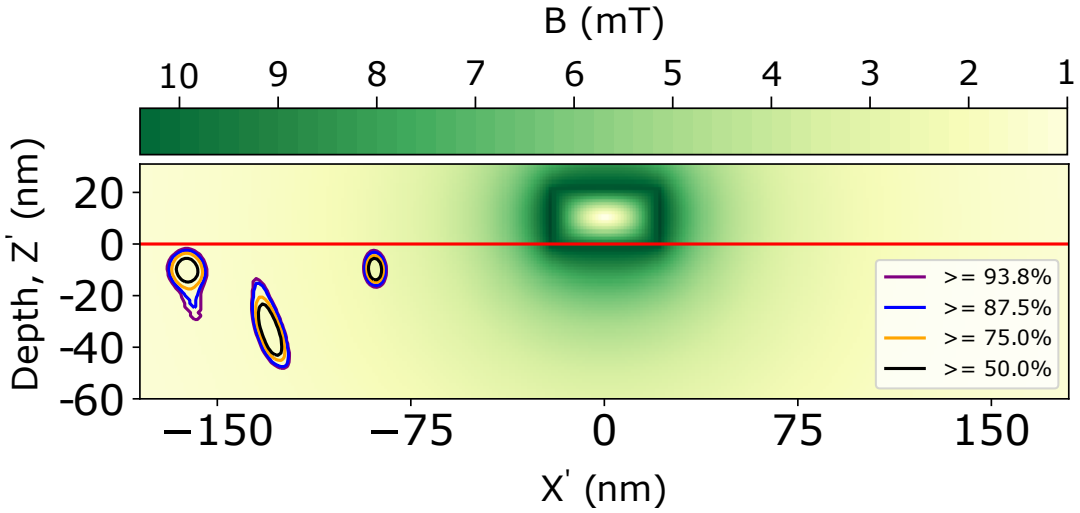


Figure 4: **Estimation des positions des centres NV individuels.** Résultat analytique. La carte des couleurs représente l'amplitude du champ magnétique $\mathbf{B}_0$ dû à un courant continu passant à travers le nanofil. La ligne rouge continue en profondeur = -10 nm correspond à la surface du diamant. Les lignes pointillées représentent la probabilité carte de densité de la position du NV.

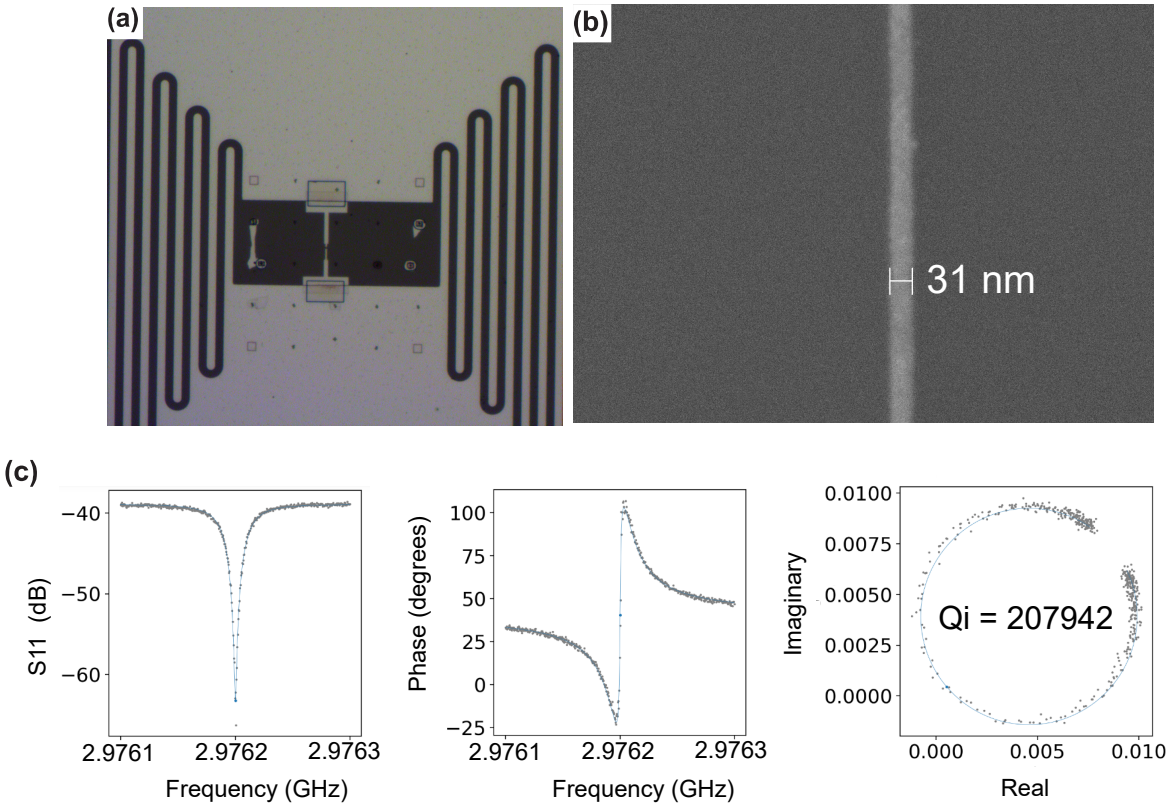


Figure 5: **Résonateur**: **a.** Image au microscope optique; **b.** Image SEM du nanofil; **c.** Caractérisation des micro-ondes: ajustement pour déterminer la fréquence de résonance $\omega_0/2\pi$ et le facteur de qualité du résonateur $(Q_i; Q_c; Q_t)$

# Chapter 1

# Introduction

The field of magnetic resonance allows a deep understanding of the matter and its structure at the atomic level. Its application is everywhere in our everyday life, with a remarkable emphasis in life science and medicine. Electron Spin Resonance (ESR) spectroscopy [1] is a branch of magnetic resonance that detects unpaired electron spins. It is widely used in molecular biology, material science and chemistry to analyze paramagnetic structures and to characterize products and molecules, understanding their structure and properties. The most usual way to detect ESR spectroscopy is via the microwave absorption of an ensemble of spins when they are tuned in resonance with a resonator to which they are coupled, a method called inductive detection. ESR spectroscopy is usually performed at room temperature. However, the thermal noise associated with the weak spin-photon coupling results in a poor sensitivity of ESR spectrometers. At X-band, on the order of $\sim 10^{13}$ spins are required to obtain sufficient signal in a single measurement sequence.

There is an active research aiming at enhance the sensitivity of inductive ESR spectroscopy [2, 3, 4, 5, 6, 7, 8], triggered by the progress of superconducting quantum circuits and circuit quantum electrodynamics (cQED)[9] where high fidelity detection of weak microwave signals is essential for the measurement and manipulation of qubits. Promising results have been achieved recently by using Josephson Parametric Amplifiers (JPA) [10] whose amplification adds no extra noise. ESR spectroscopy at quantum-limit of sensitivity has been reported by Bienfait at. al., who demonstrated a sensitivity of 1700 spins/$\sqrt{(}Hz)$ [6].

In light of this, it has been theoretically predicted by Haikka et. al. [12] that single-spin sensitivity should be reachable by combining high quality factor superconducting micro-resonators and Josephson Parametric Amplifiers. Moreover, Probst at. al. has shown that by optimizing the superconducting resonator design, the sensitivity was enhanced up to 65 spins/$\sqrt{(}Hz)$ [13].

This is the context of this thesis whose motivation is to perform experimentally the Haikka proposal, i.e, to enhance the ESR spectroscopy towards the limit of single spin detection by mediating the coupling of a single spins with photon radiation using a LC high quality factor superconducting resonator.

After a brief summary of this thesis in the first chapter, the second chapter describes

the details of the Haikka proposal, and aims at providing the conceptual tools required to understand the measurements. We first explain the principles of the spin dynamics driven by a classical microwave field, as well as the pulse sequences used for spin characterization. Then, we present the spin-resonator coupling Hamiltonian. The essential parameter is the spin-photon coupling constant $g$. When taking into account the resonator losses (at a rate $\kappa$), the spin can emit spontaneously microwave photons, via the Purcell effect. We finish the chapter by estimating the measurement time of a single spin coupled to a resonator

$$T_{meas} = \frac{\kappa^2 \Gamma_2^*}{g^4}, \tag{1.1}$$

where we have considered ideal microwave amplification, and $(\Gamma_2^*)^{-1} \equiv T_2^*$ is the spin coherence time. For reasonable parameters, a sub-millisecond measurement time is achievable. However, this requires a precise alignment (of order 10nm) of the spin with a nanowire inserted in the resonator, as well as a sufficiently long coherence time.

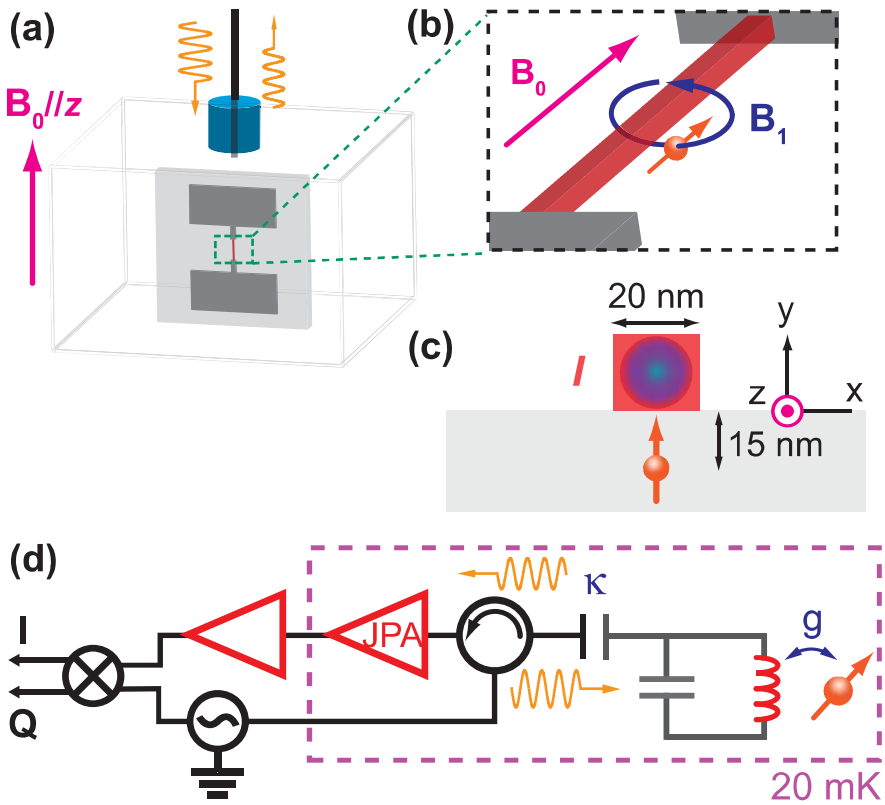


Figure 1.1: **Proposed setup**. **a.** Superconducting LC resonator consisting of two pads (capacitor C) and wire (inductance L) placed in a three-dimensional microwave cavity. **b.** Nanometer-scale constriction made at the center of the inductance wire, below which a single spin is located at 15 nm. **c.** Cross section of the structure. **d.** Schematic of the considered measurement circuit. The signal leaking out of the cavity is first amplified by a quantum-limited Josephson parametric amplifier (JPA), followed by cryogenic low-noise HEMT and room-temperature amplifiers.[12]

The third chapter describes the physics of NV centers in diamond (Fig.1.2a), which

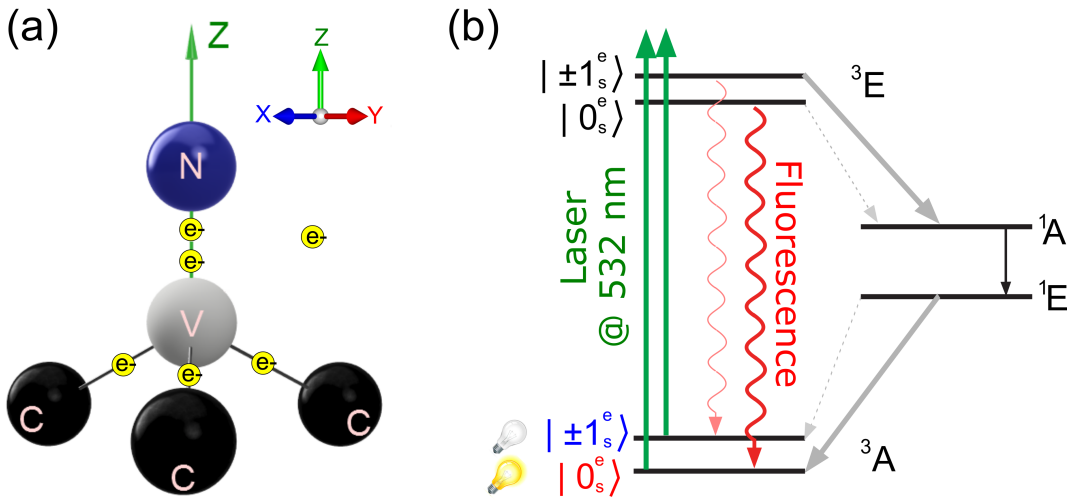


Figure 1.2: **Spin system used in this thesis. a.** Sketch of the NV: trigonal symmetry formed by 3 carbon atoms (black), 1 Nitrogen atom (blue) and the vacancy of carbon (white). The symmetric axis, Z, is shown in green. In yellow are shown the 6 $NV^-$ electrons involved in the $NV^-$ system. **b.**NV shined with green laser emits red photoluminescence (PL). ${}^3A_{m_s=0}$ excitation leads to PL after $\sim 12ns$ while ${}^3A_{m_s=\pm1}$ excitation most probably decays non-radiatively towards the metastable state ${}^1A$ resulting in an occupancy of $m_s^g = 0$ after $\sim 300\,ns$. The spin-dependence of the electronic spin relaxations enables the spin initialization and readout at room temperature

are the model spin system used in this thesis. The specificity of NV centers in diamond is that they can be implanted at well-defined locations, and fully characterized at room-temperature by Optical Detection of Magnetic Resonance (ODMR), Fig.1.2b.

The fourth chapter reports one of the main results of this thesis. We demonstrate the fabrication of a sample with an array of individual NV centers, located at precise position with respect to alignment marks that were etched into the substrate, and with long coherence times (up to 50$\mu$s), as shown in Fig.1.3. This was obtained by implantation through a resist mask pierced with nanometric-sized holes.

We then proceed by testing our ability to align precisely a single NV center and a metallic nanowire deposited on top of the diamond. For that, in the fifth chapter, we perform an experiment where we use single-NV vector magnetometry to determine a posteriori the position of several NV centers with respect to aluminum nanowires through which we pass some dc current. We determine the relative position with a $\sim 10\,$nm accuracy. We find a systematic shift of order 100 nm, despite our best efforts, as shown in Fig.1.4. Based on these results, we decided to target the coupling of the resonator to a small ensemble of implanted NV centers, where the alignment accuracy is less critical.

In the final chapter of the thesis, we report on the resonator design, fabrication, and characterization at millikelvin temperatures. The resonator loss rate is sufficiently low to perform the experiment envisioned, as demonstrated in Fig.1.5. Unfortu-

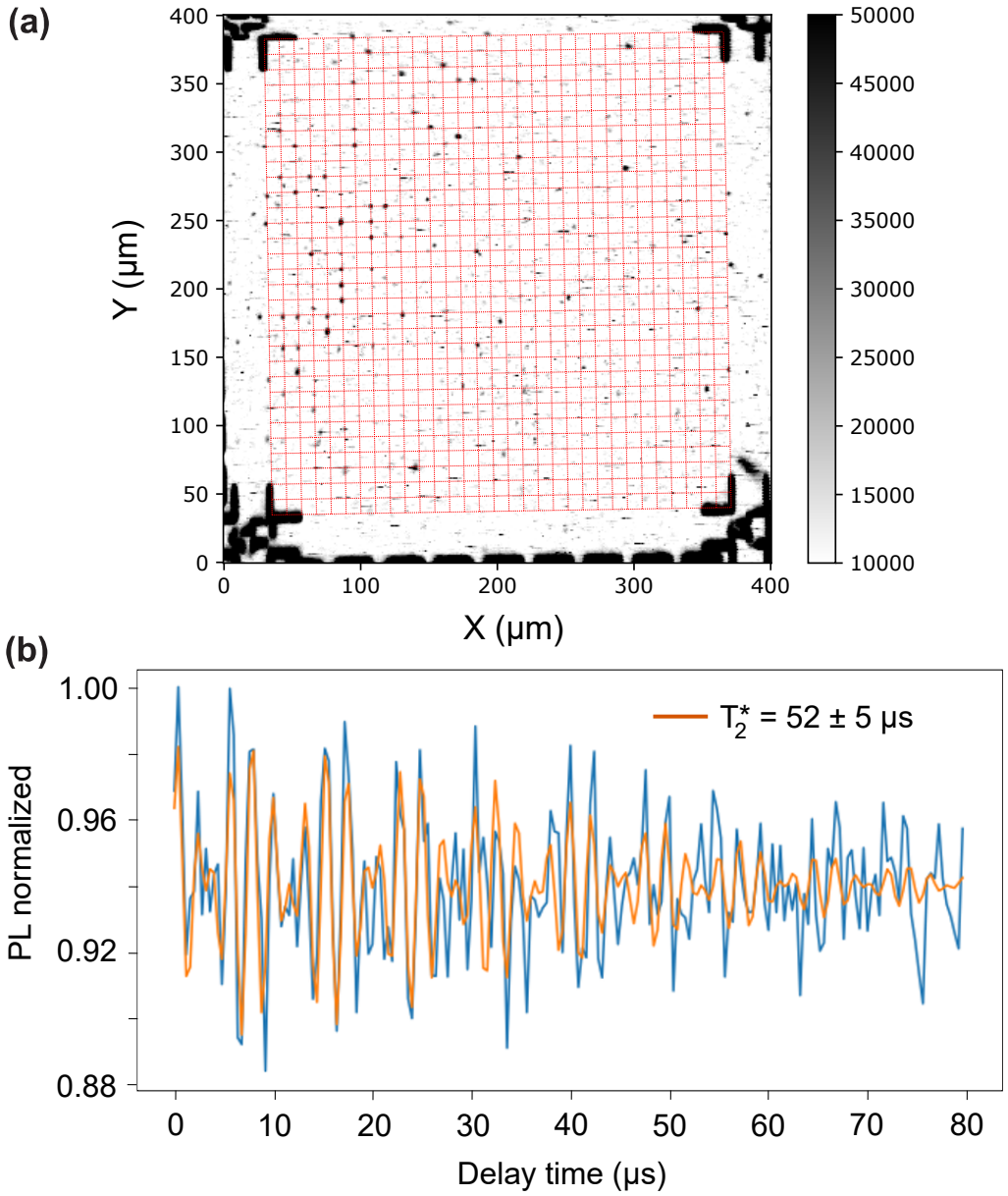


Figure 1.3: **Realization of an array of precisely placed NV centers with long coherence times. a.** Confocal microscope image of a single NV center. The color scale indicates the number of photons collected per second; **b.**Ramsey measurement of a single NV. $T_2^* = 52\mu s$

nately, the magnetic-field resilience of the resonator was insufficient to tune the NV with the resonator; as a result, the spin signal was not measured.

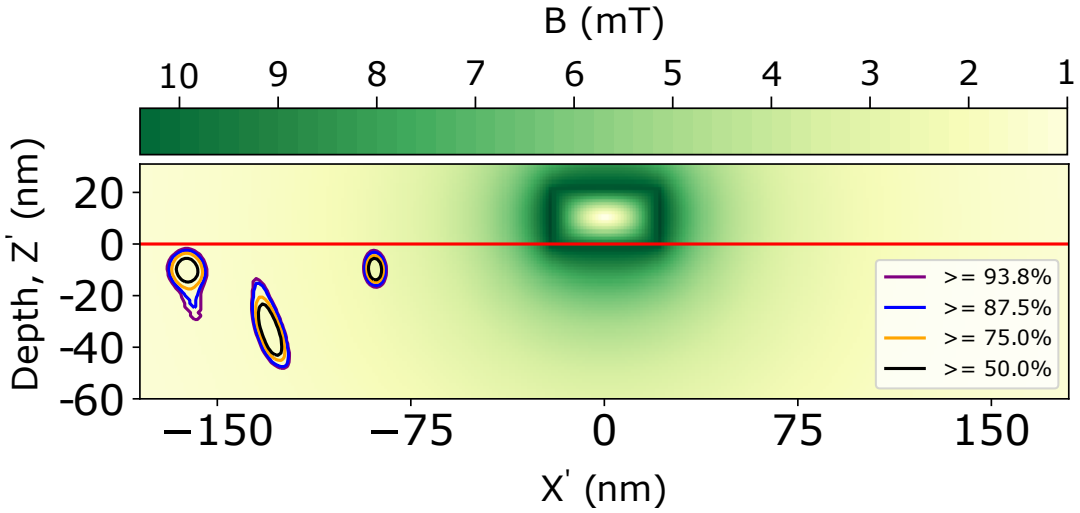


Figure 1.4: **Estimating single NV centers' positions.** Analytical result. The color map represents the magnitude of the magnetic field $\mathbf{B}_0$ due to a DC current passing through the nanowire. The continuous red line at depth = -10 nm corresponds to the diamond surface. The dashed lines are the probability density map of the NV's position

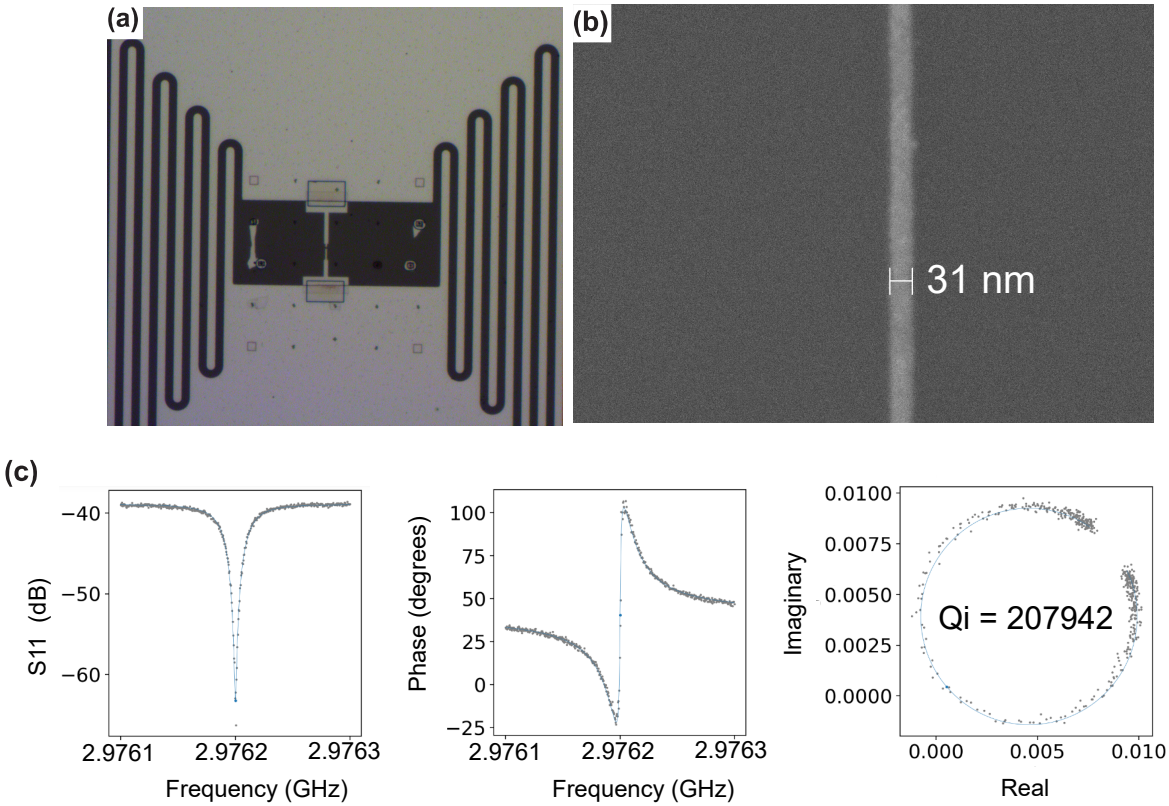


Figure 1.5: **Resonator**: **a.** Optical microscope image, **b.** SEM image of the nanowire; **c.** Microwave characterization: Fit to determine the resonance frequency $\omega_0/2\pi$ and the resonator quality factor $(Q_i; Q_c; Q_t)$

# Chapter 2

# Proposal for detecting a single spin with microwaves

Although there are alternative ESR techniques that can reach the nanoscale, there is still a strong interest to increase inductively-detected ESR spectroscopy sensitivity due to versatility of such spectrometers [5, 14, 15, 16]. This chapter gives theory elements needed to understand the context of our experimental work. The final goal of this work is to realize experimentally a theoretical proposal [12], which consists in performing single-spin detection with microwave signals at low temperatures.

We will start with a simple description of the dynamics of a spin driven by a classical field, including pulse sequences used for characterizing their coherence properties. In a second part, we will turn to the quantum-mechanical description of the interaction of a spin with a quantum field in a cavity. This will enable us, in a third paragraph, to estimate the time needed to obtain a measurable signal from a spin coupled to a nanowire cavity, i.e. to present the proposal that motivates the experimental work described in the following chapters. The main result is that, with an experimentally achievable value of the spin-photon coupling constant, single spin detection is possible with an integration time of a few milliseconds.

## 2.1 Single spin detection: state-of-art

Owing to the weak interaction between spins and electromagnetic fields, an inductively-detected ESR spectroscopy detection requires a large number of spins, leading to a poor sensitivity and thus, preventing the study on single spin samples such as single protein molecule or a nanoparticle.

Alternative techniques have been developed to overcome this limit and enhance the sensitivity of ESR towards the nanoscale. Some of them are illustrated on Fig.2.1. They involve scanning probe setups, optically (ODMR) or electrically (EDMR) detected magnetic resonance.

Single spin detection can be achieved by Magnetic Resonance Force Microscopy (MRFM) Fig.2.1a [17]. The atomic force microscope (AFM) cantilever has a magnetic tip that generates a magnetic field gradient such that the single spin can be detected by a very sensitive measurement of the cantilever displacement.

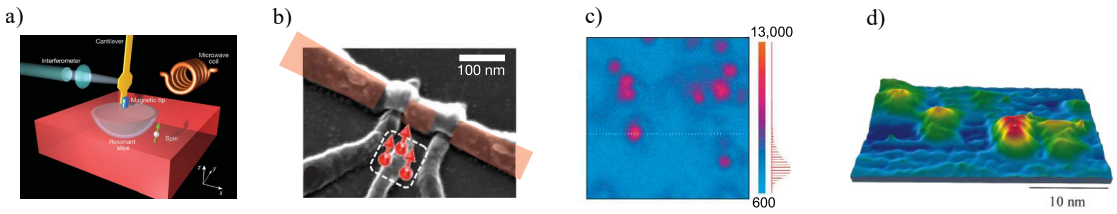


Figure 2.1: **Single-spin detection** reached using alternative techniques rather then inductive ESR spectroscopy. **a.** Single-spin detection using a MRFM setup. **b.** Single Si:P donor detection with a *SET*. **c.** Photoluorescence color map of a diamond comprising single NV centers, allowing for single-spin ODMR. **d.** Imaging of four BDPA molecules using a STM. Figures are extracted respectively from [17, 18, 19, 20]

The EDMR is based either on spin-dependent charge-carrier transport and recombination [21, 22] or on spin charge conversion. In the last one the charge is efficiently detected by a charge sensor such as: individual spin in quantum dots [23, 24], single electron transistor (SET) Fig.2.1b [25, 26, 18], field effect transistor [27] and individual magnetic molecules [28, 29]

The ODMR is based on spin-dependent photoluminescence, property of certain systems such as doped pentacene single molecules [30, 19], Nitrogen-Vacancy (NV) centers in diamond Fig.2.1c [19] and Silicon-Vacancy (SiV) in Diamond [31]. The single spin sensitivity is obtained by detecting optical photons after optical pumping. The ODMR on NV centers will be widely used thoughout this thesis and is explained in detail on Chapter 3.

Spin-polarized scanning tunneling microscopy (STM) has also been used to detect single spin in nanostructures. It is based either on detecting the increased noise of the tunnel current at the spin precession frequency [32, 33, 20, 34] or on spin-polarized detection of the atomic-scale tunneling magnetoresistance [34, 35]. The last method requires operation at cryogenic temperatures and can also achieve subnanometer spatial resolution.

Despite these considerable advances, single spin detection remains a challenge, requiring specific systems or elaborate setups. This motivates the need for pursued research on alternative single spin detection methods. Our proposed method, described in the remaining of this chapter, relies entirely on microwave signals for spin detection thanks to an enhanced spin-microwave coupling, with possible applications in quantum information processing.

## 2.2 Dynamics of a spin driven by a classical field

### System and Hamiltonian

We consider an electron spin system, subjected to a dc magnetic field $B_0$ applied along the $z$ axis. Its spin Hamiltonian $H_s(B_0)$ includes a Zeeman term $-\hbar\gamma_e \mathbf{S}\cdot\mathbf{B_0}$, where $\gamma_e$ is the electron gyromagnetic ratio and $\mathbf{S}$ the spin operator, and may also

include other terms such as zero-field splitting or hyperfine couplings. Diagonalizing this Hamiltonian yields the system eigenstates. We assume in the following that the system dynamics can be approximated correctly by restricting the equations to two states only (for instance, the ground and the first excited state), which we will denote as $|0\rangle$ and $|1\rangle$, with transition frequency $\omega_s(B_0) = (E_1 - E_0)/\hbar$. This effective spin-1/2 can be described by the Pauli operators; for instance, its Hamiltonian is $H_s(B_0) = -\hbar\omega_s/2\sigma_z$.

This spin system is additionally driven by some microwave field with a frequency $\omega$ close to the spin frequency $\omega_s$. In this section, we consider the field to be classical, described by $\mathbf{B_1}(t) = \mathbf{B_1}\cos\omega t$. This adds a term in the spin system Hamiltonian $H_1(t) = -\hbar\gamma_e \mathbf{S}\cdot\mathbf{B_1}(t)$.

In the frame rotating at $\omega$, and neglecting fast-rotating terms, the total spin Hamiltonian then writes

$$H = \frac{\delta}{2}\sigma_z + \frac{\Omega_R}{2}\sigma_x, \tag{2.1}$$

with $\delta = \omega - \omega_s$, and $\Omega_R = \gamma_e\langle 0|\mathbf{S}|1\rangle\cdot\mathbf{B_1}$ the Rabi frequency [36].

**Coherent evolution : Rabi oscillations**

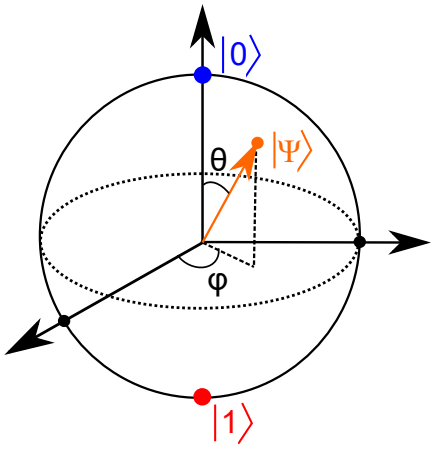


Figure 2.2: Bloch sphere sketch

A convenient representation for understanding spin dynamics is provided by the Bloch sphere. An arbitrary pure quantum state can always be written as $|\Psi\rangle = \cos(\theta/2)\,|0\rangle + e^{i\varphi}\cos(\theta/2)\,|1\rangle$. This can be mapped uniquely to a three-dimensional vector called the Bloch vector, defined as $(\sin\theta\cos\varphi, \sin\theta\sin\varphi, \cos\theta)$, whose location is a unit radius sphere called the Bloch sphere, as shown in Fig.2.2.

Hamiltonian Eq.2.1 describes rotations of the Bloch vector representing the spin around an axis located in the $(x, z)$ plane and defined by the angle it does with the $z$ axis $\theta_R$, with $\tan\theta_R = \Omega_R/\delta$. The rotation frequency is given by $\sqrt{\Omega_R^2 + \delta^2}$. Let us now give specific examples that will be used throughout this thesis.

**Free evolution** If no microwave drive is present ($\Omega_R = 0$), the spin quantum state undergoes a rotation at the Larmor frequency $\delta$ around the $z$ axis.

**Rabi oscillations** If a resonant microwave drive is applied to the spin ($\delta = 0$) for a duration $\Delta t$, oscillations around the $x$ axis occur at the Rabi frequency $\Omega_R$. These Rabi oscillations are widely used for manipulating the spin state, and for decoherence characterization as explained in the following. Two pulses are particularly interesting :

- When $\Omega_R \Delta t = \pi/2$, state $|0\rangle$ is transformed into a coherent superposition of states with equal weight $(|0\rangle + i\,|1\rangle)/\sqrt{2}$. This is called a $\pi/2$ pulse.
- When $\Omega_R \Delta t = \pi$, $|0\rangle$ is transformed into $|1\rangle$, and $|1\rangle$ into $|0\rangle$. This is called a $\pi$ pulse.

**Bloch equations and steady-state solutions**

To describe spin dynamics, one also needs to consider damping phenomena. Following Bloch, we consider a minimal damping model in which the spin population difference is damped at a rate $\Gamma_1$, and the spin phase coherence is damped at a rate $\Gamma_2$. Because spin relaxation also causes some decoherence, it can be shown that $\Gamma_2 \geq \Gamma_1/2$ [36]. We will give more details later on the physics of decoherence in the specific case of NV centers in diamond.

This leads to the following equations for the mean value of the spin operators

$$\dot{S}_x = -\delta S_y - \Gamma_2 S_x \tag{2.2}$$
$$\dot{S}_y = \delta S_x + \Omega_R S_z - \Gamma_2 S_y \tag{2.3}$$
$$\dot{S}_z = -\Omega_R S_y - \Gamma_1 (S_z - S_0), \tag{2.4}$$

where $S_0$ is the equilibrium value of $S_z$, which we will assume is the ground state $S_0 = -1/2$.

These equations were proposed phenomenologically by Bloch in 1949. The Rabi oscillations described in the previous paragraph appear as a coherent transient towards steady-state solutions, which are given by

$$S_x = \frac{\Omega_R \delta}{\Gamma_2^2 + \Omega_R^2 \Gamma_2/\Gamma_1 + \delta^2} S_0 \tag{2.5}$$
$$S_y = \frac{\Omega_R \Gamma_2}{\Gamma_2^2 + \Omega_R^2 \Gamma_2/\Gamma_1 + \delta^2} S_0 \tag{2.6}$$
$$S_z = \frac{\Gamma_2^2 + \delta^2}{\Gamma_2^2 + \Omega_R^2 \Gamma_2/\Gamma_1 + \delta^2} S_0 \tag{2.7}$$

**Decoherence characterization with Ramsey and echo sequences**

We now describe common pulse sequences used to characterize the spin coherence time.

The Ramsey pulse sequence, shown in Fig.2.3a, is used to measure $\Gamma_2$. The microwave frequency is purposely detuned from the spin frequency by a detuning $\delta$.

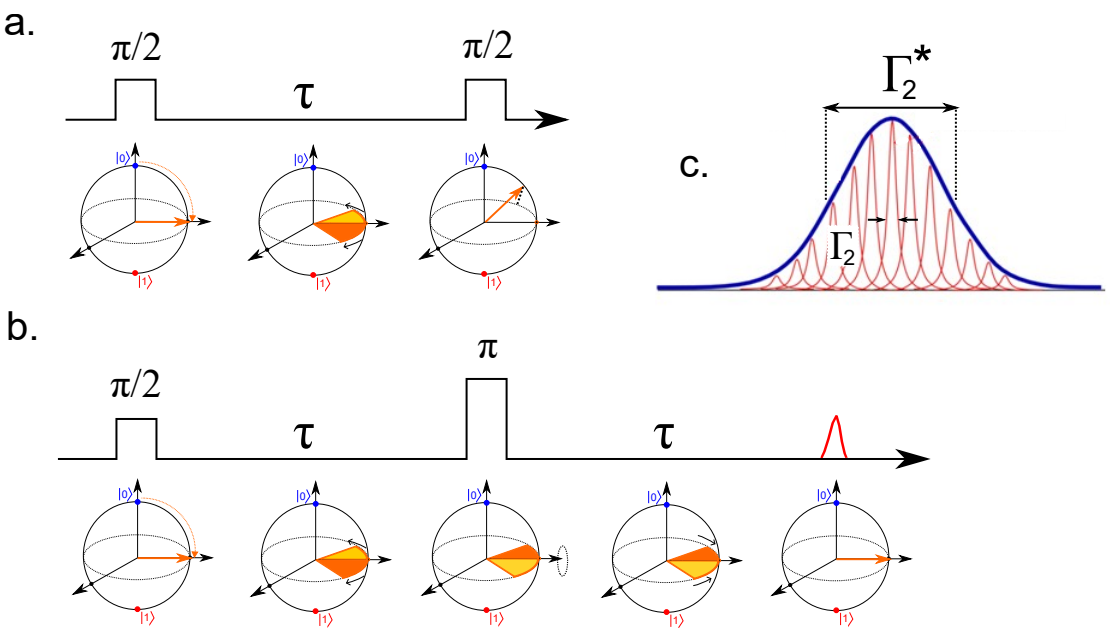


Figure 2.3: **Pulse sequence. a.** Ramsey sequence. **b.** Echo sequence. **c.** Spin inhomogeneous linewidth

The spin system is prepared at time $t = 0$ in a superposition of states $(|0\rangle + i\,|1\rangle)/\sqrt{2}$ by a $\pi/2$ pulse (note that the pulse is applied with a Rabi frequency $\Omega_R \gg \delta$, thus the detuning has no impact on the Rabi rotation achieved). Then, the spin is left to evolve freely for a duration $T$. It therefore undergoes a rotation at frequency $\delta$ on the equator of the Bloch sphere. A second $\pi/2$ pulse is then applied, achieving a second rotation around $x$, and the spin state is finally measured, yielding the probability to find the spin in the ground state $P_0(T)$. Due to the free evolution, $P_0(T)$ oscillates with period $\delta$. Decoherence causes this oscillation to be damped, and the rate provides a direct measurement of $\Gamma_2$.

Spin decoherence is however more complex than this simplistic picture. In general, it cannot be described simply by a simple rate as is the case in the Bloch equations. The reason is that the environment causing spin decoherence is often non-Markovian, implying that it evolves slowly, because it consists of a bath of weakly interacting spins. Therefore, we need to distinguish two phenomena :

- Due to the very slow evolution of its environment, the spin resonance frequency $\omega_s$ at the beginning of each experiment is distributed with a certain probability density around its mean value, with a typical width $\Gamma_2^*$. The frequency stays fixed during one experimental sequence (one speaks of static inhomogeneous broadening). Because Ramsey fringes are measured by averaging a large number of sequences, they in fact give access to the static inhomogeneous linewidth $\Gamma_2^*$, Fig.2.3c.

- In order to measure the actual loss of phase coherence happening during one sequence, we therefore need to perform a different experiment from the Ramsey fringes. This is achieved with the spin-echo sequence [37], which is insensitive to static inhomogeneous broadening. This sequence is depicted in Fig.2.3b. It consists of a $\pi/2$ pulse at resonance, followed by a delay $\tau$, a $\pi$ pulse, a second

waiting time $\tau$, and a second $\pi/2$ pulse followed by a spin population measurement. The decay of the spin population gives access to the true decoherence rate $\Gamma_2$. In general, $\Gamma_2^* \gg \Gamma_2$.

## 2.3 Coupling of a spin to a quantized microwave field

To achieve single-spin detection with microwave signals, we need to enhance the spin-microwave interaction as much as possible. Therefore, we will use a high-quality-factor microwave resonator. We are interested in the changes of microwave field induced by the presence of one spin. Estimating this requires a quantum description of the interaction of the spin with the intra-resonator field.

### Jaynes-Cummings Hamiltonian

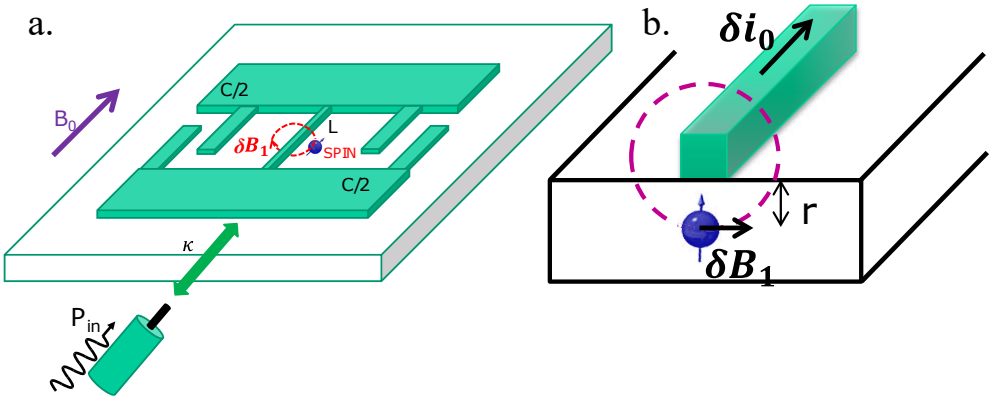


Figure 2.4: **Sketch of a LC resonator coupled with a single spin. a.** LC resonator capacitively coupled with a transmission line (input microwave power $P_{in}$) and $\kappa$ is the cavity energy damping rate. A static magnetic field $B_0$ is applied parallel to the inductive wire which, in turn, is coupled to the spin via the magnetic field quantum fluctuations ($\delta B_1$). **b.** Zoom in the inductive wire. $r$ is the spin-wire relative distance. The current quantum fluctuations $\delta i$ generates $\delta B_1$ that couples to the spin Lamor frequency.

The system that we consider is depicted in Fig.2.4. The spin is coupled to the magnetic component of the microwave field stored in a $LC$ resonator of frequency $\omega_0$. Compared with the previous section, we will now treat this field as a quantum-mechanical operator. The system Hamiltonian now includes, in addition to the spin Hamiltonian and its interaction with the microwave, also the microwave field Hamiltonian : $H = H_s(B_0) + H_0 + H_{int}$, with

$$H_0 = \hbar\omega_0 a^\dagger a \tag{2.8}$$

$$H_{int} = -\hbar\gamma_e \mathbf{S}\cdot\hat{\mathbf{B}}_\mathbf{1}. \tag{2.9}$$

Here, $a$ (resp. $a^\dagger$) is the field annihilation (resp. creation) operator, and $\hat{\mathbf{B}}_\mathbf{1} = \delta\mathbf{B}_\mathbf{1}(a + a^\dagger)$ is the magnetic field operator, where $\delta\mathbf{B}_\mathbf{1}$ is an important quantity that represents the rms fluctuations of the magnetic field when the microwave field is in

its ground state.

To go forward, we project $H$ on the two-level spin subspace, and perform the rotating-wave approximation. In the frame rotating at frequency $\omega_0$, we then obtain

$$H/\hbar = -\frac{\delta}{2}\sigma_z + g(\sigma_+ a + \sigma_- a^\dagger), \tag{2.10}$$

with $\sigma_\pm = (\sigma_x \pm i\sigma_y)/2$, and

$$g = -\gamma_e \langle 0|\mathbf{S}|1\rangle \cdot \delta\mathbf{B_1} \tag{2.11}$$

the so-called coupling constant.

The Hamiltonian Eq.2.10 describes the linear coupling of a two-level system nearly resonant with a single mode of the electromagnetic field, and is called the Jaynes-Cummings Hamiltonian [38]. It is encountered in particular in cavity and circuit quantum electrodynamics (QED), where real or artificial atoms are linearly coupled to a resonator[36]. Most cavity and circuit QED implementations rely on a dipolar electric coupling (Rydberg atoms or superconducting qubits coupled to a superconducting microwave resonator, quantum dots coupled to an optical microcavity, ...). Here, we apply cavity and circuit QED concepts to a single electronic spin.

**Purcell effect**

The dynamics of the spin-cavity system described by the Jaynes-Cummings is very different, depending on the ratio between the coupling constant $g$ and the cavity energy damping rate $\kappa$. The regime where $g < \kappa$ is called the weak coupling, whereas $g > \kappa$ is the strong coupling regime. For reasons that will be clarified later, the planned experiments are in the weak coupling regime, and we will concentrate on this case in the following.

In the weak coupling regime, the coupling of the cavity to the spin gives rise to a radiative relaxation channel for the spin, via the Purcell effect [39]. When the spin and cavity are resonant ($\omega_s = \omega_0$), the spin can return to its ground state by emitting a microwave photon in the cavity, which then leaks out towards the measurement line. The rate for this decay is given by the Purcell formula

$$\Gamma_P = 4g^2/\kappa. \tag{2.12}$$

This effect is essential in the present proposal, because the Purcell rate is the rate at which the spin scatters photons in the measurement line, and therefore also the rate at which we may acquire information about its presence or absence. The higher the Purcell rate, the faster the measurement, as will be clear in the following.

## 2.4 Single spin detection proposal

We now have sufficient background to describe the proposed experiment. Here we follow the main lines of [12], where more detail can be found if needed.

### Proposed experiment

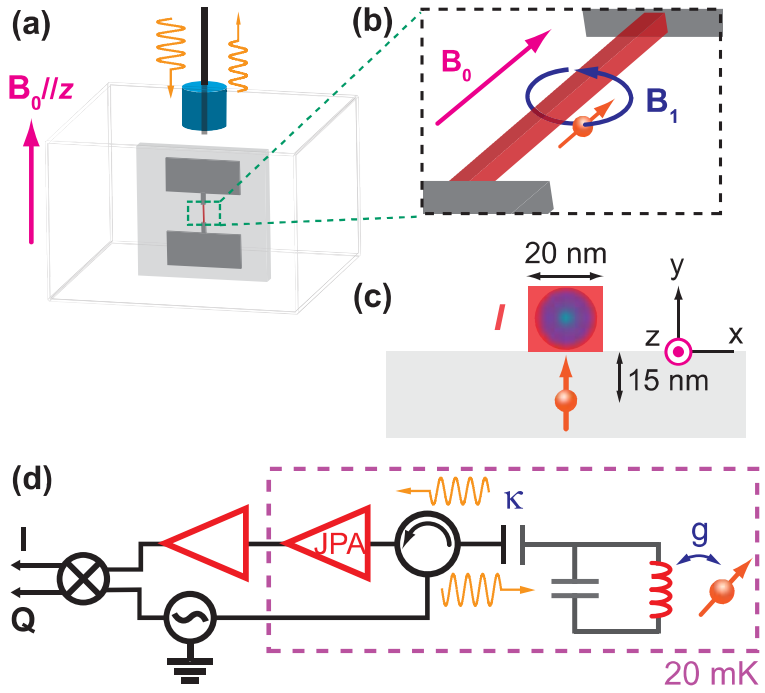


Figure 2.5: **Proposed setup**. **a.** Superconducting LC resonator consisting of two pads (capacitor C) and wire (inductance L) placed in a three-dimensional microwave cavity. **b.** Nanometer-scale constriction made at the center of the inductance wire, below which a single spin is located at 15 nm. **c.** Cross section of the structure. **d.** Schematic of the considered measurement circuit. The signal leaking out of the cavity is first amplified by a quantum-limited Josephson parametric amplifier (JPA), followed by cryogenic low-noise HEMT and room-temperature amplifiers.[12]

The heart of the experiment is shown in Fig.2.5. A spin is coupled (with constant $g$) resonantly to a microwave LC resonator ($\omega_s = \omega_0$), which is probed in reflexion via a measurement line coupled to the resonator at a rate $\kappa$. The probing tone is a continuous-wave microwave signal, with amplitude $\beta$, related to the incoming power by $P_{in} = \hbar\omega_0|\beta|^2$ so that $|\beta|^2$ represents the number of photons per second incident on the cavity input. The presence of a spin leads to some amount of microwave absorption, which constitutes the spin detection signal. The question we wish to answer is the measurement time : how long does it take for the signal-to-noise ratio to reach 1 to discriminate between the presence of a spin and its absence ?

We first estimate the amplitude of the spin signal. From the Jaynes-Cummings Hamiltonian, and taking into account cavity field driving and damping, one obtains the following equation for the field operator in the steady-state

$$\langle a \rangle = \frac{2}{\kappa}(-ig\langle\sigma_-\rangle + \sqrt{\kappa}\beta). \tag{2.13}$$

To compute the mean spin polarization, we furthermore assume that the spin is

in the weak coupling regime and that we can treat it as a small perturbation of the cavity field. In that limit, the spin is driven by the unperturbed intra-cavity field $\alpha_0 = 2\beta/\sqrt{\kappa}$. The spin operator mean value is obtained by the steady-state solution of the Bloch equations, with $\Omega_R = 2g\alpha_0$. This yields

$$\langle\sigma_-\rangle = -i\frac{g\alpha_0\Gamma_1}{4g^2\alpha_0^2 + \Gamma_1\Gamma_2^*}. \tag{2.14}$$

Maximizing the spin signal requires to maximize $\langle\sigma_-\rangle$. This is obtained at saturation, when $\alpha_0 = \sqrt{\Gamma_1\Gamma_2^*}/2g$. We then obtain

$$\langle\sigma_-\rangle_0 = -i\frac{g\alpha_0}{2\Gamma_2^*} = -\frac{i}{4}\sqrt{\frac{\Gamma_1}{\Gamma_2^*}} \tag{2.15}$$

The spin signal, as seen from the intra-cavity field, is then

$$\alpha_0 = -\frac{2ig\langle\sigma_-\rangle_0}{\kappa} = -\frac{g}{2\kappa}\sqrt{\frac{\Gamma_1}{\Gamma_2^*}} \tag{2.16}$$

For spins at low temperature, $\Gamma_1$ can become very low, in which case the spins are saturated at very low powers, and yield a very low absorption signal. This is why the Purcell effect is so essential, as it considerably increases $\Gamma_1$, even in conditions where the spin-lattice relaxation becomes negligibly small. Assuming $\Gamma_1 = \Gamma_P = 4g^2/\kappa$, the previous equation simplifies to

$$\alpha_0 = -\frac{g^2}{\kappa}\sqrt{\frac{1}{\kappa\Gamma_2^*}} \tag{2.17}$$

### Measurement time

We now determine how long it takes to measure this signal (the measurement time $T_{\text{meas}}$). For that, we consider that the signal leaking out of the cavity (the output field $a_{out} = \sqrt{\kappa}a$) is amplified by several stages of amplification, and then detected by mixing it with a local oscillator at room-temperature (which is called homodyne detection).

The total output noise has two distinct origins : first, the quantum fluctuations of the microwave field; then, the noise added by the imperfections of the amplification chain. This added noise is conveniently described by a parameter $\eta = 1/(1+N)$, $N$ being the number of photons added in a mode by the amplifiers. The quantum theory of amplifiers developed by C. Caves [40] predicts that $\eta = 1/2$ for the best possible amplifier if it equally amplifies all phases, whereas $\eta$ can reach 1 for an amplifier that amplifies only one signal phase (and de-amplifies the orthogonal other

one). Even the best commercial microwave amplifiers are however far from these numbers, barely reaching $\eta \simeq 0.01$. Reaching Caves limit has become possible in the recent years thanks to the development of superconducting amplifiers based on Josephson junctions, the so-called Josephson Parametric Amplifiers (JPA) [41, 42], that are used as first amplifiers in the detection chain (see Fig.2.5).

The output signal measured during time $\Delta t$, after amplification and homodyne detection, is modelled by

$$dY = \eta(a_{out} + a_{out}^{\dagger})dt + \sqrt{\eta}dW. \tag{2.18}$$

The last term describes the field quantum fluctuations by a Wiener noise term $dW$, with zero mean and variance $dt$. This output signal is integrated for a time $T$. Assuming the local oscillator phase is chosen to maximize the spin signal, this yields

$$\zeta(T) = \frac{1}{\sqrt{T}} \int_0^T dY = 2\eta\sqrt{T}a_{out} + \sqrt{\eta}\Delta W, \tag{2.19}$$

where $\Delta W$ is a Gaussian-distributed with zero mean and unit variance. When no spin is present, $\zeta(T)$ has a Gaussian distribution centered on 0 and with variance $\eta$; when a spin is present, $\zeta(T)$ has a mean of $2\eta\sqrt{T}a_{out}$ and a variance of $\eta$. The signal-to-noise reaches unity when the separation between the two distributions is equal to twice their standard deviation, which is reached in our case for

$$T_{meas} = \frac{\kappa^2\Gamma_2^*}{\eta g^4}. \tag{2.20}$$

To minimize the measurement time, it is thus essential to maximize the spin-photon coupling $g$, minimize resonator losses, have long spin coherence time $\Gamma_2^{*-1}$, and use the best Josephson parametric amplifiers.

**Realistic estimates, and targeted parameters**

We now provide realistic estimates of the parameters involved in the experiment.

The first and most essential parameter is the spin-photon coupling constant $g$. As shown in Eq.2.11, this requires estimating the rms magnetic field fluctuations at the spin location, $\delta B_1$. In order to maximize $\delta B_1$, our approach is to bring the spin as close as possible to the resonator, and to concentrate the magnetic field around a narrow constriction.

The geometry that we consider is shown in Figs.2.4 and 2.5. The resonator consists of a planar lumped-element resonator, with a capacitor $C$ shunted by an inductor $L$ that includes a short section of a nanowire, with width $w$ and thickness $t$. The spin is located at a depth $d$ below the surface, in the middle of the nanowire, at a

distance $r = d + t/2$ from the nanowire. A biasing field $B_0$ is applied parallel to the sample surface. The microwave magnetic field $\mathbf{B_1}$ is then perpendicular to $B_0$, along the $x$ direction.

The rms current fluctuations $\delta i$ through the resonator inductor are given by

$$\delta i = \omega_0 \sqrt{\frac{\hbar}{2Z_0}}, \tag{2.21}$$

with $Z_0 = \sqrt{L/C}$ the resonator impedance. A simple estimate of $\delta B_1$ is then obtained by modelling the nanowire as infinitely thin, yielding $\delta B_1 = \mu_0 \delta i/(2\pi r)$. An analytical formula is also available for the rectangular wire, as explained in the Appendix A and in [12].

The resonator design is discussed in detail in Chapter 6. Its target frequency is 3 GHz, close to the resonance frequency of NV centers in diamond as explained in the next chapter, with an impedance $Z_0 \simeq 11\Omega$.

Using the above formula, and considering $w = 20\,\text{nm}$, $t = 15\,\text{nm}$, and $d = 15\,\text{nm}$, we obtain $\delta i = 35\,\text{nA}$, and $\delta B_1 = 0.33\mu\text{T}$. For NV centers in diamond, $\langle 0|S_x|1\rangle = 1/\sqrt{2}$ as explained in the next chapter, and we thus obtain $g/2\pi = 6.5\,kHz$.

In order to minimize the energy losses, the planar resonator must be patterned out of a superconducting metal, and the microwave losses should be minimized. A loss rate $\kappa \sim 10^5 \text{s}^{-1}$ is commonly reached in Circuit QED experiments, and this is the value we consider here. Note that we are indeed in the weak coupling regime, since $g \ll \kappa$. This yields a Purcell rate $\Gamma_P = 4g^2/\kappa = 3 \cdot 10^4 \text{s}^{-1}$.

For spin decoherence, we consider $\Gamma_2^* = 10^5 \text{s}^{-1}$ as a realistic target value (see next chapter). Using a parametric amplifier, noiseless amplification can be achieved, so that we can suppose $\eta = 1$. With these figures, a measurement time $T_{meas} = 0.4\,\text{ms}$ is predicted. This prediction is the motivation for this PhD work.

Summarizing the requirements of this experiment, we need individual spins with long coherence times, close to the sample surface, and aligned as well as possible (with an accuracy of order 10 nm) with a nanowire resonator patterned on top of the sample. In the following chapter, we will see that NV centers in diamond are well suited to satisfy these requirements. The specific interest of our proposal is that it enables in principle the detection of any sort of spin as long as its coherence time is sufficiently long, whereas usual single-spin detection methods are system-specific, as shown previously in this chapter, relying for instance on the existence of optical transitions with suitable spin properties.

# Chapter 3

# NV centers in diamond

We now describe the spin system used throughout this thesis: NV centers in diamond. They consist in a substitutional Nitrogen atom into the diamond lattice with an adjacent carbon vacancy.

Despite studies on NV centers have been performed since 60's [43], the research interest in NV centers has widely increased after 1997 when Gruber et. al [44] first isolated individual NV centers using an optical confocal microscope. NV centers present a robust photostability which allows them to be used as a stable source of single photons [45, 46]. Moreover, NV centers are paramagnetic and their spin magnetic resonance is optically detected at room temperature (ODMR) [47]. The ability of initializing and reading the NV' spins, associated with their long coherence times [48], have triggered the interest of researchers in the field of quantum computing, quantum communication [49, 50, 51, 52, 53, 54] quantum memories [55] as well as quantum sensors [56, 57, 58], magnetic resonance spectroscopy [59, 60] and probing of magnetic structures [61, 62, 63, 64] at the nanoscale. NV centers are also promising for the implementation of quantum networks [65, 54, 66, 67].

This chapter is a review about the NV center useful properties to the understanding of the experimental work. In what follows, we will give a brief description of the NV structure, charge state and Hamiltonian of the NV ground state spin before describing their optical properties and ODMR. We will comment on their Hyperfine interaction as well as the magnetometry based on NV centers. Finally we will discuss the principal sources of NV spin decoherence and comment on the specific properties of NV centers located close to the diamond surface ("shallow NVs").

## 3.1 Structure and charge state

Diamond is a semiconductor whose conduction and valence bands are separated by 5.49 eV [68], in the ultraviolet domain. Its large bandgap favors the existence of optically active defects called color centers. Among the numerous color defects that can be found in the diamond lattice, NV centers have been widely investigated in recent years due to their optical and spin properties.

NV centers belong to the $C_{3v}$ symmetry group [69] i.e., they have a trigonal structure where the symmetric axis, Z axis, is defined along the Nitrogen and the Vacancy,

green arrow as seen in Fig. 3.1 b. When the NV is formed in a bulk diamond, there are only four possible NV orientations, and they are along the four ⟨111⟩ crystallographic graphic axis of the diamond, as schematically shown in figure Fig. 3.1 a. Throughout this thesis, we will use only samples with the surface oriented perpendicular to the ⟨100⟩ crystallographic axis, which is shown in Fig. 3.1a as a yellow plane. The green arrow in Fig. 3.1a corresponds to the NV Z axis, that are represented on each configuration. Note that the referential used to describe the NV Hamiltonian is (X, Y, Z), different from the host diamond coordinate system (x', y', z').

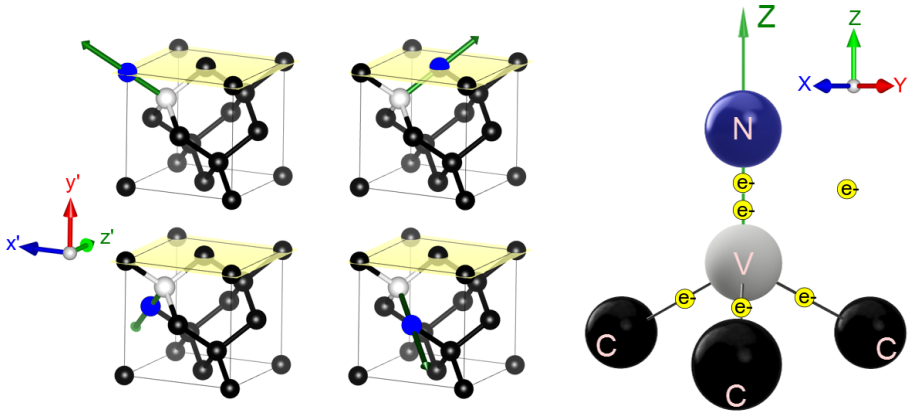


Figure 3.1: **NV Center Structure**. **a.** Sketch showing the 4 possible orientations of the NV ⟨111⟩ crystallographic axis of the diamond. The yellow surface is oriented perpendicular to ⟨111⟩.; **b.** Sketch of the NV: trigonal symmetry formed by 3 carbon atoms (black), 1 Nitrogen atom (blue) and the vacancy of carbon (white). The symmetric axis, Z, is shown in green. In yellow are shown the 6 $NV^-$ electrons involved in the $NV^-$ system.

NV centers can be found in three distinct charge states:

- *The neutral charge state*, $NV^0$ , which presents 5 electrons (1 from each carbon dangling bound, the other 2 arising from the dangling bounds of the Nitrogen).
- *The positive charge state*, $NV^+$, which happens if $NV^0$ loses an electron.
- *The negative charge state*, $NV^-$ , that occurs when $NV^0$ captures an extra electron from the environment. It presents a electronic spin triplet [49] and it is the only NV charge state whose spin can be controlled and optically measured at room temperature.

The charge state of interest for this work is $NV^-$ , whose structure is shown in Fig. 3.1b. From now on, we will refer to $NV^-$ by simply NV.

The NV spin system possesses an electronic and nuclear spin and its properties are governed by its structure and symmetry [70]. *The electronic spin* derives from its 2 unpaired electrons. The spin quantization axis is along the NV Z axis, while X and Y axes are in the normal plane regarding to the NV symmetric axis. Thus, the electronic spin S = 1 can be decribed using the operator $\mathbf{S} = (\hat{S_X}, \hat{S_Y}, \hat{S_Z})$ which

are:

$$\hat{S}_X = \begin{pmatrix} 0 & 1 & 0 \\ 1 & 0 & 1 \\ 0 & 1 & 0 \end{pmatrix}; \hat{S}_Y = \begin{pmatrix} 0 & -i & 0 \\ i & 0 & -i \\ 0 & i & 0 \end{pmatrix}; \hat{S}_Z = \begin{pmatrix} 1 & 0 & 0 \\ 0 & 0 & 0 \\ 0 & 0 & -1 \end{pmatrix} \tag{3.1}$$

*The nuclear spin* is due to the Nitrogen atom. The Nitrogen isotope of the NV center can be either $I^{^{14}N} = 1$ or $I^{^{15}N} = 1/2$. The NV centers studied in this thesis were formed by $^{15}N$ whose nuclear spin is described by $\mathbf{I}^{^{15}N} = (\hat{I}_X^{^{15}N}, \hat{I}_Y^{^{15}N}, \hat{I}_Z^{^{15}N})$.

## 3.2 Ground state electron spin energy levels

In the presence of a magnetic field $\mathbf{B}_0$ , the ground state of the NV electronic spin Hamiltonian is:

$$H_{NV}/\hbar = H_{ZF}/\hbar + H_{Zeeman}/\hbar \tag{3.2}$$

where $H_{ZF}$ is the zero field splitting Hamiltonian and $H_{Zeeman}$ is the Zeeman shift Hamiltonian. Each of these components are described below.

***The Zero field splitting*** is a spin-spin interaction which arises from the exchange energy between the 2 unpaired electrons of the NV center [70]. It results in a splitting of the energy levels $|m_s = 0\rangle$ and $|m_s = \pm 1\rangle$ even in the absence of external magnetic field. The Hamiltonian depends on the zero field splitting tensor $\bar{\mathbf{D}}$:

$$\begin{aligned} H_{ZF}/\hbar &= \mathbf{S} \cdot \bar{\mathbf{D}} \cdot \mathbf{S} \\ &= D_X \hat{S}_X^2 + D_Y \hat{S}_Y^2 + D_Z \hat{S}_Z^2 \end{aligned} \tag{3.3}$$

Due to the axial symmetry of the NV center, the Hamiltonian can be rewritten as:

$$H_{ZF}/\hbar = D S_Z^2 \tag{3.4}$$

where $D/2\pi = 2.87GHz$ in the ground state. The presence of local electric field or strain would result in an additional term of the form $E({S_X}^2 - {S_Y}^2)$. In this thesis, however, this effect is negligible and we consider E = 0.

***The Zeeman effect*** describes the interaction of the electron spin with the magnetic field $\mathbf{B}_0$ . Thus, the Hamiltonian is given by:

$$\begin{aligned} H_{Zeeman}/\hbar &= \frac{-g_e \mu_B}{\hbar} \mathbf{B}_0 \cdot \mathbf{S} \\ &= -\gamma_e \mathbf{B}_0 \cdot \mathbf{S} \end{aligned} \tag{3.5}$$

where, $g_e = 2$ is the NV Landé factor; $\mu_B$ is the Bohr magneton and $\gamma_e = -2\pi \times 2.8MHz/G$ is the gyromagnetic ratio of the NV electron spin.

In the absence of strain, X and Y are equivalent directions. We will therefore in the following assume that the magnetic field $\mathbf{B}_0$ is applied in the plane (X,Z). The matrix form of the Hamiltonian in eq. 3.2 is:

$$H = \begin{pmatrix} D - \gamma_e B_0 \cos\theta & -\gamma_e B_0 \sin\theta & 0 \\ -\gamma_e B_0 \sin\theta & 0 & -\gamma_e B_0 \sin\theta \\ 0 & -\gamma_e B_0 \sin\theta & D + \gamma_e B_0 \cos\theta \end{pmatrix} \tag{3.6}$$

where $\theta$ is the angle between $\mathbf{B}_0$ and the NV axis Z. The electron spin energy spectrum is determined by diagonalizing the Hamiltonian, eq.3.6. Fig. 3.2 shows the Hamiltonian eigenvalues calculated as a function of the applied magnetic field oriented:

- *Parallel to the NV:* ($\theta = 0°$) The electron spin energy levels are linearly dependent of the magnetic field, Fig. 3.2a.
- *Perpendicular to the NV:* ($\theta = 90°$) the energy levels have a parabolic dependence with the applied magnetic field, Fig. 3.2b.

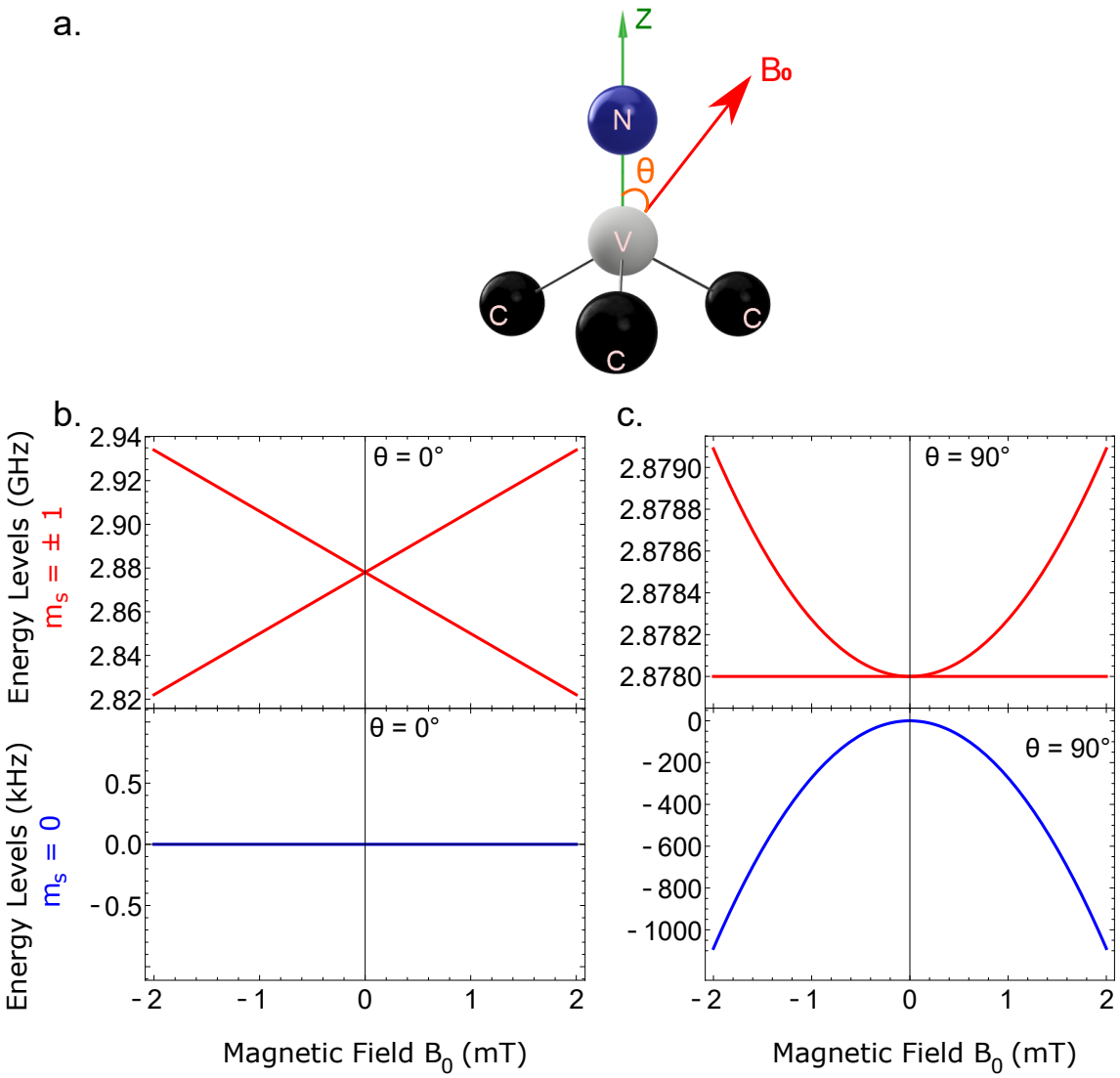


Figure 3.2: **Energy levels of the electron spin Hamiltonian**. **a.** Applied magnetic field $\mathbf{B}_0$ forming an angle $\theta$ with the NV Z axis; **b.** $\theta = 0°$; **c.** $\theta = 90°$

Beyond those two cases, we are also interested in another particular configuration that will be widely explored throughout this thesis, which is: external magnetic field parallel to the diamond surface and forming an angle of $\theta_0 = 54.7°$ with the NV center Z axis.

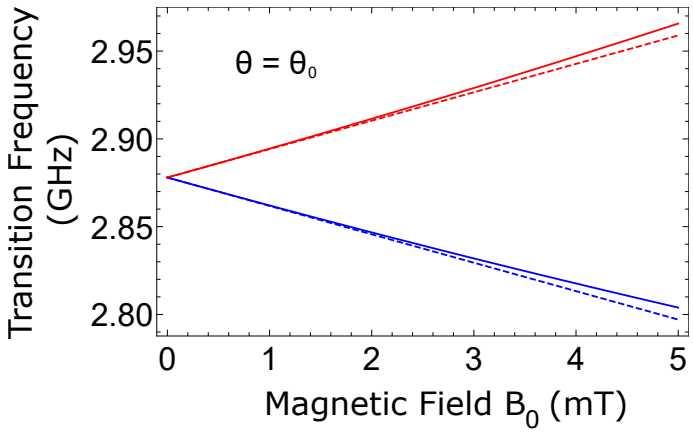


Figure 3.3: *NV*$^-$ **ground state transition energy spectrum**. Comparison between $\mathbf{B}_0$ applied along *NV*$^-$ axis Z and $\mathbf{B}_0$ an applied parallel to the diamond surface $\theta_0 = 54.7°$.

The energy levels in this case are shown in Fig. 3.3 (solid lines), and compared to the energy levels obtained by neglecting the component of $\mathbf{B}_0$ perpendicular to Z. We see that as long as $\mathbf{B}_0 < 1$mT, the error is smaller than 2%. Throughout this thesis, we will neglect this deviation, and make the approximation that the Zeeman shift of the NV electron spin states is simply given by the projection of the $\mathbf{B}_0$ field along Z, $\mathbf{B}_0\ cos\theta$.

## 3.3 Optical transitions and ODMR

In addition to its ground state ($^3A$), NV also possesses several other orbital states of higher energy: an excited state ($^3E$), which is also a spin triplet and can be populated via green laser pumping; and two metastable spin singlet states ($^1A$ and $^1E$).

Optical transitions between $^3A$ and $^3E$ are spin-conserving. The relaxation from $^3E$ towards $^3A$ gives rise to the interesting NV electron spin properties. Indeed, the $^3E_{m_s=0}$ relaxes radiatively towards the ground state $^3A_{m_s=0}$ in $\sim 10ns$. However, the excited $^3E_{m_s=\pm1}$ relaxes with a high probability towards a metastable singlet state $^1A$ by intersystem crossing, which then relaxes towards the $^3A_{m_s=0}$ ground state via a second metastable state $^1E$ in $\sim 300ns$ (see Fig. 3.4). Thus, this spin-dependence relaxation mechanism has two consequences:

1. Under green laser illumination, NV electronic spin is efficiently pumped towards the $^3A_{m_s=0}$ ground state. This enables spin initialization;

2. In the first 300ns [71], the NV electronic spin emits more photoluminescence (PL) in the $^3A_{m_s=0}$ than in the $^3A_{m_s=\pm1}$, because of its high chance to become "trapped" in the dark metastable state. This enables spin readout.

That is the principle of *Optically Detected Magnetic Resonance*, ODMR, whose spectrum can be measured using a 532 nm laser to polarize and readout the spin [72]. The PL emitted by the NV is in the visible range, in the red. The PL contrast

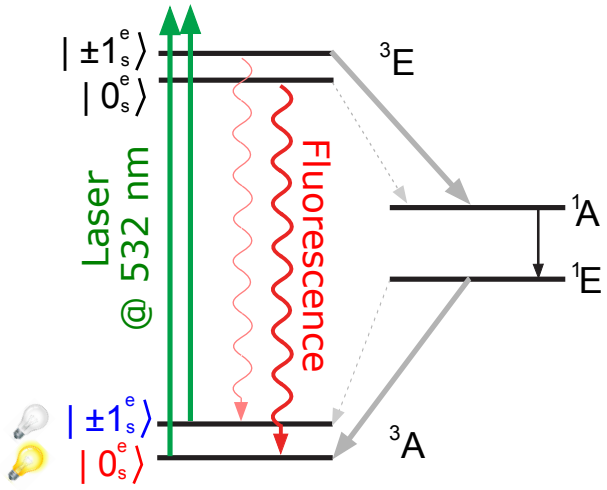


Figure 3.4: **ODMR**. NV shined with green laser emits red photoluminescence (PL). ${}^3A_{m_s=0}$ excitation leads to PL after $\sim 12ns$ while ${}^3A_{m_s=\pm1}$ excitation most probably decays non-radiatively towards the metastable state ${}^1A$ resulting in an occupancy of $m_s^g = 0$ after $\sim 300\,ns$. The spin-dependence of the electronic spin relaxations enables the spin initialization and readout at room temperature.

is the figure of merit of the ODMR intensity and it is defined as:

$$C(T) = \frac{N_0(T) - N_1(T)}{N_0(T)} \tag{3.7}$$

where $N_0(T)$ $[N_1(T)]$ is the total number of collected photons during an integration time T for the NV electron spin initially prepared in $|0_e\rangle$ $[|\pm 1_e\rangle]$.

Fig. 3.5 shows the time-resolved PL during a readout laser pulse of a single NV center initially prepared either on $|0_e\rangle$ (black) or $|\pm 1_e\rangle$ (red). One can see not only the contrast but also the steady state saturation value. The last one is due to initialization process that occurs within the characteristic metastable life-time. Therefore, although continuous laser can be used to perform ODMR, owing to the steady-state the contrast decreases for integration times longer than 300 ns. That is why we have used green laser pulses of 300 ns, to optimize the PL contrast [71].

A typical ODMR sequence includes:

- A first 532 nm laser pulse to initialize the spin in ${}^3A_{m_s=0}$
- A sequence of microwave pulses designed to measure the desired spin property (spectroscopy, Rabi, ...)
- A second 532 nm laser pulse to readout the spin state, during which the photoluminescence is integrated over the first 300 ns to determine the spin state. Note that this laser pulse also re-initializes the spin for the next sequence.

## 3.4 Room temperature setup

All the experiments at room temperature are based on the collection of the Photoluminescence (PL) emitted by the NV centers. To collect the PL we have used a

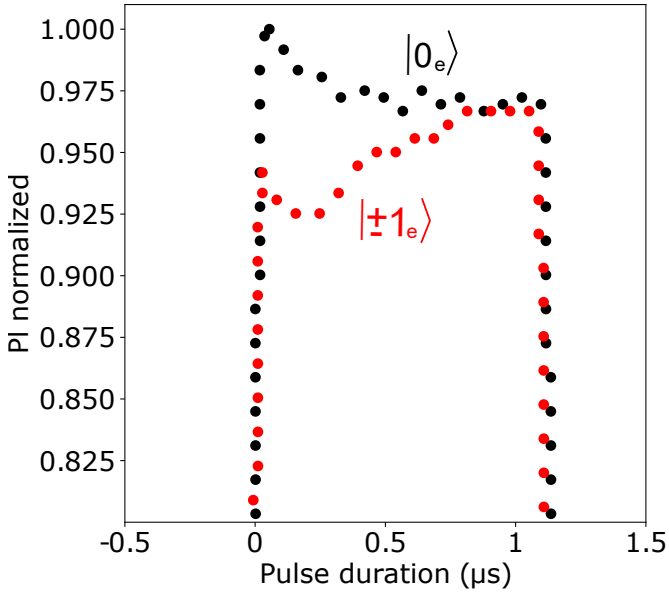


Figure 3.5: **Time resolved Photoluminescence during a laser pulse readout of a single NV center.** The black (red) dots corresponds to the PL collected for an electronic spin prepared in $m_s = 0$ ($m_s = \pm 1$).

home-built confocal microscope [73], see Fig. 3.6, which is described below.

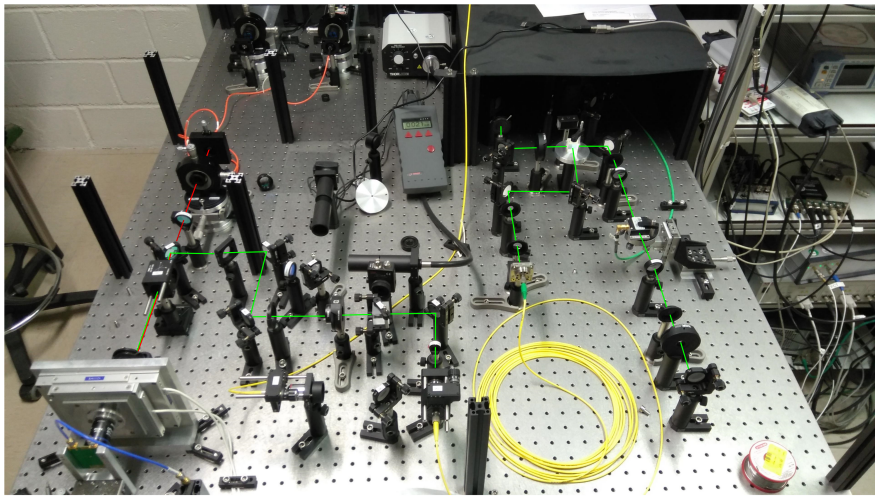

Figure 3.6: **Optical Table**. Photograph of our home made optical table.

We have used a commercial continuous wave doubled-frequency Nd:YAG green laser ($\lambda = 532nm$). Following the green laser path on Fig. 3.7 we can identify the main components of the optical table. The laser intensity that impinges the sample is controlled by $\lambda/2$ wave plate. An acousto-optic modulator associated with a $\lambda/4$ and mirror is used to perform the laser pulses. A dichroic mirrors reflects the green laser towards the objective. The objective is focused at the diamond sample surface which, in turn, is attached to piezoelectric allowing to scan the diamond surface.

There is a considerable difference between the refractive index ($\eta$) of the air and diamond, 1 and 2.4 respectively. This hampers the PL collection. To overcome this

difficulty we use oil with a typical $\eta \sim 1.5$. Moreover, the sample holder is a Printed Circuit Board (PCB) which allowed us to pass a microwave near the diamond surface. More details about the PCB can be found later in Chapter 4.

Once the green laser illuminates a NV center, it becomes excited and emits PL through the objective. The dichroic mirror reflects the green but it is transparent to the red PL. The PL reaches, then, the so-called confocal microscope. Here, it is composed by a lens, a pinhole at the lens focus and a optical fiber at twice the focus distance. The PL will cross the confocal if, and only if, the emitter NV center was at the focus of the objective, been filtered out otherwise. The Avalanche Photo Detector (APD) collects the fluorescence which is digitized and plotted as a color scale graphic.

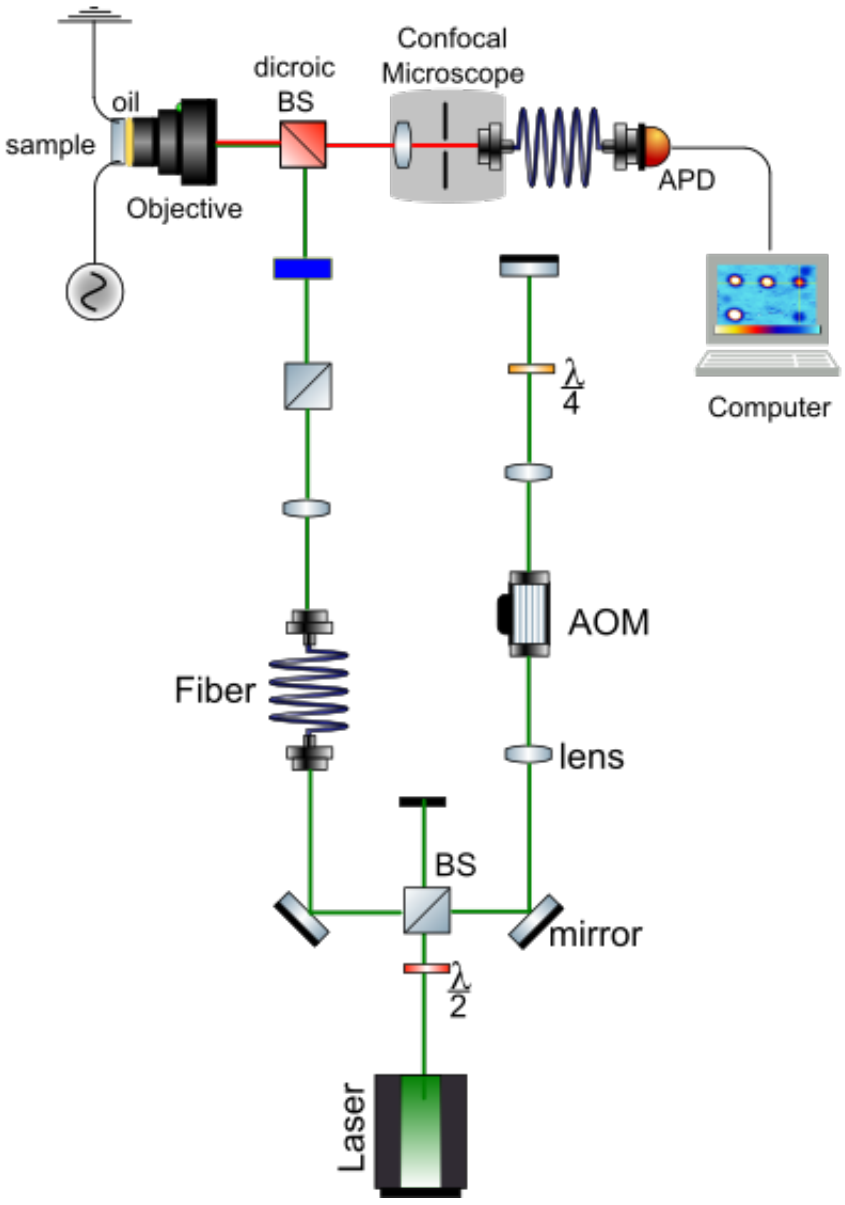


Figure 3.7: **Sketch of the room temperature optical setup.**

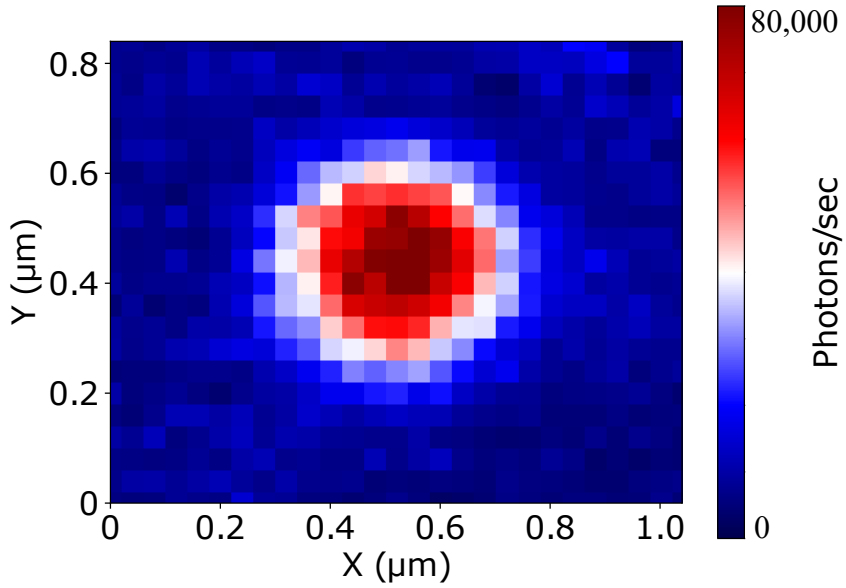


Figure 3.8: **Confocal image of a single NV center**. .

A typical confocal microscope image is shown in Fig. 3.8. The number of Photons collected from a single NV depends on the sample background, the laser power and the photon collection efficiency. In our system, at 0.3mW laser power, the PL collected for a single NV is around $7 \cdot 10^4 - 10^5$ photons per second.

## 3.5 Hyperfine interaction

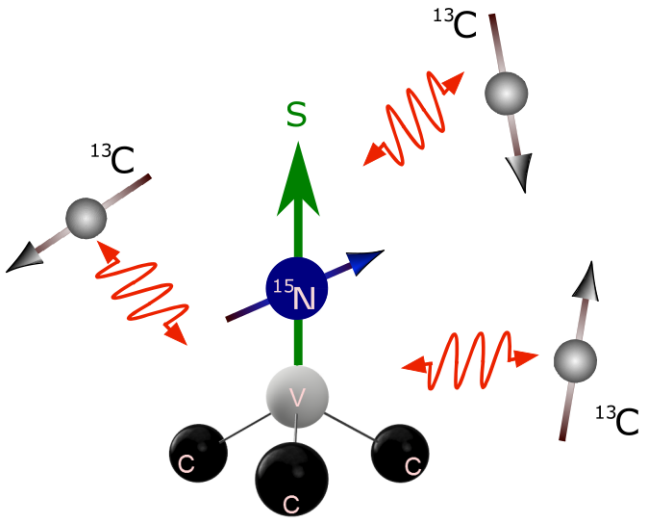


Figure 3.9: **Hyperfine Interaction**. Schematic representation of the NV electronic spin interaction with the environment nuclear spins.

The electron spin of the NV center is coupled to nuclear spins present in the diamond lattice by the hyperfine interaction. First, the nitrogen atom itself possesses

a nuclear spin, I=1/2 for the $^{15}N$ isotope, or I=1 for the $^{14}N$ isotope. Then, the carbon atoms forming the diamond lattice can possess a nuclear spin if they are from the $^{13}C$ isotope, present at 1.1% abundance in natural carbon.

The location of $^{13}C$ atoms is random, therefore the configuration of $^{13}C$ atoms around a NV is different between NV centers, which leads to intrinsic variations in frequency and coherence times in-between individual NVs. On the other hand, all NV centers have the same hyperfine coupling to the Nitrogen nuclear spin, which thus needs to be considered as an integral part of the NV spin Hamiltonian because of the important role it plays in its dynamics. In the following we thus study the energy levels resulting from the NV spin Hamiltonian including the hyperfine interaction with the N nuclear spin. We will concentrate on the case of the $^{15}N$ isotope, since this is the one that we use throughout this thesis, as explained in Chapter 4.

$$H_{^{15}N}/\hbar = H_{NV}/\hbar + \gamma_n \mathbf{B}_0 \cdot \mathbf{I}^{^{15}N} + \mathbf{S} \cdot \bar{\mathbf{A}}^{^{15}N} \cdot \mathbf{I}^{^{15}N} \tag{3.8}$$

The first term corresponds to the NV electronic spin Hamiltonian 3.2. The second term is the Zeeman Hamiltonian of the $^{15}N$ nuclear spin. The gyromagnetic ratio of the Nitrogen nuclear spin, $I^{^{15}N}$ is $\gamma_n/2\pi = -4.3$ MHz/T. The nuclear spin operators are:

$$\hat{I}_X = \begin{pmatrix} 0 & 1 \\ 1 & 0 \end{pmatrix}; \hat{I}_Y = \begin{pmatrix} 0 & -i \\ i & 0 \end{pmatrix}; \hat{I}_Z = \begin{pmatrix} 1 & 0 \\ 0 & -1 \end{pmatrix} \tag{3.9}$$

The last term of the Hamiltonian 3.8 is the hyperfine interaction between the NV electronic spin and $I^{^{15}N}$, where $\bar{\mathbf{A}}$ is the hyperfine interaction tensor:

$$\bar{\mathbf{A}}^{^{15}N} = \begin{pmatrix} A_\perp & 0 & 0 \\ 0 & A_\perp & 0 \\ 0 & 0 & A_\parallel \end{pmatrix}$$

and the measured values of this matrix components are: $A_\perp/2\pi = 3.65$ MHz and $A_\parallel/2\pi = 3.03$ MHz.

The matrix form of the Hamiltonian eq. 3.8 is:

$$H = \begin{pmatrix} \alpha_1 & \beta & 0 & \delta & 0 & 0 \\ \beta & \alpha_2 & \beta & \frac{A_\perp}{\sqrt{2}} & \delta & 0 \\ 0 & \beta & \alpha_3 & 0 & \frac{A_\perp}{\sqrt{2}} & \delta \\ \delta & \frac{A_\perp}{\sqrt{2}} & 0 & \alpha_4 & \beta & 0 \\ 0 & \delta & \frac{A_\perp}{\sqrt{2}} & \beta & -\alpha_2 & \beta \\ 0 & 0 & \delta & 0 & \beta & \alpha_5 \end{pmatrix} \tag{3.10}$$

Where,

$\alpha_1 = D + \frac{A_\parallel}{2} + B_0 \cos\theta(\gamma_e + \frac{\gamma_n}{2})$
$\alpha_2 = \frac{B_0 \cos\theta\gamma_n}{2}$
$\alpha_3 = D - \frac{A_\parallel}{2} + B_0 \cos\theta(-\gamma_e + \frac{\gamma_n}{2})$
$\alpha_4 = D - \frac{A_\parallel}{2} + B_0 \cos\theta(\gamma_e + \frac{-\gamma_n}{2})$

$\alpha_5 = D + \frac{A_\parallel}{2} - B_0 \cos\theta(\gamma_e + \frac{\gamma_n}{2})$
$\beta = -\frac{B_0 \sin\theta\gamma_e}{\sqrt{2}}$
$\delta = -\frac{B_0 \sin\theta\gamma_n}{2}$

Diagonalizing the eq. 3.10 determines the NV spin energy spectrum. They are plotted on Fig. 3.10 and Fig. 3.11 for three specific configurations of external magnetic field: $\theta = 0°$ (Fig. 3.10a), $\theta = 90°$ (Fig. 3.10b) and $\theta_0 = 54.7°$ (Fig. 3.11). The red [blue] curves corresponds to $m_s = \pm 1$ [$m_s = 0$].

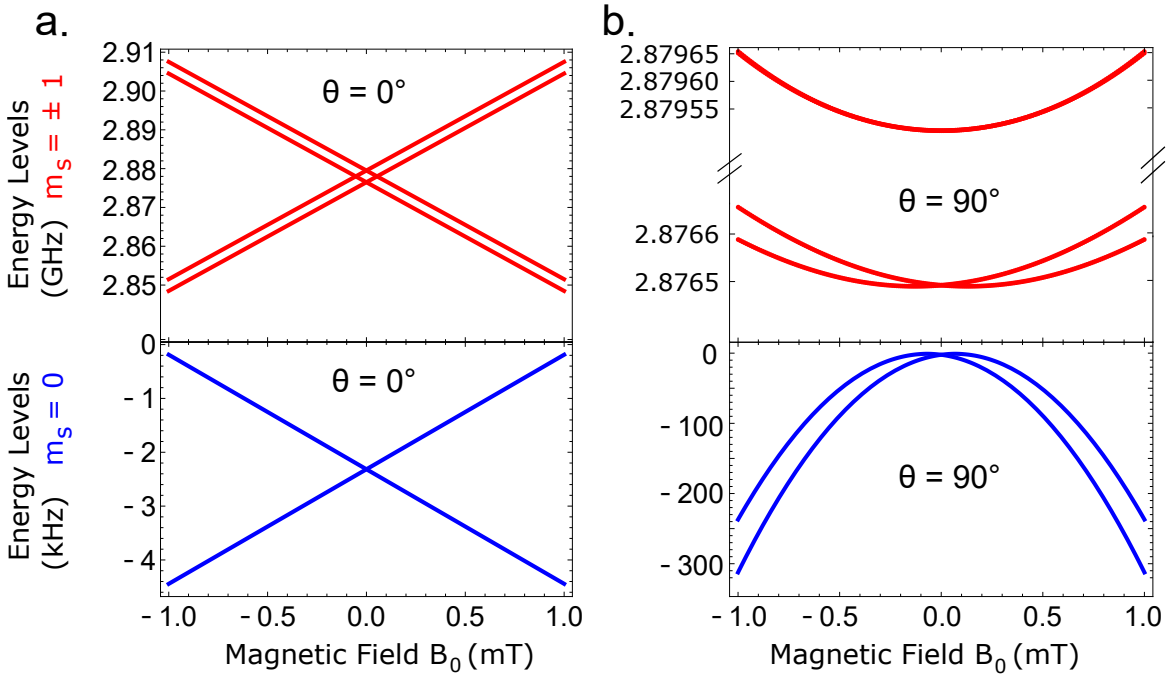


Figure 3.10: $NV^-$ **hyperfine energy spectrum**. **a.** NV Hamiltonian Eigenvalues with a external magnetic field oriented at $\theta = 0°$; **b.** $\theta = 90°$

### Eigenstates and ESR-allowed transitions

The most relevant scenario for our experiments is the low-field limit where $\gamma_e B_0 << A_\parallel/2\pi$. In a such case, the eigen-states depend on the electronic spin state. When $m_s = \pm 1$, $\mathbf{S} \cdot \bar{\mathbf{A}}^{^{15}N} \cdot \mathbf{I}^{^{15}N}$ dominates the Hamiltonian leading to an alignment of the nuclear spin with the electronic spin, both along the Z axis. Thus, its eigen-basis are: $|\pm 1_e, \uparrow_N\rangle$ and $|\pm 1_e, \downarrow_N\rangle$.

When $m_s = 0$, on the other hand, the nuclear Zeeman energy remains but the hyperfine term vanishes to first order.

When $\mathbf{B}_0$ is applied along Z ($\theta = 0°$), the nuclear spin eigenstates are also $|\uparrow_N\rangle$ and $|\downarrow_N\rangle$. Their energy is determined by the nuclear Zeeman shift, as seen in Fig. 3.10a, with $\gamma_n$ as the gyromagnetic ratio. When $\mathbf{B}_0$ is applied along X ($\theta = 90°$) the nuclear spin eigenstates in $m_s = 0$ are $|\rightarrow_N\rangle$ and $|\leftarrow_N\rangle$. Interestingly, the gyromagnetic ratio is however no longer the bare NV gyromagnetic ratio, as can be seen in Fig. 3.12 where the difference in frequency between $|m_S = 0, \rightarrow_N\rangle$ and

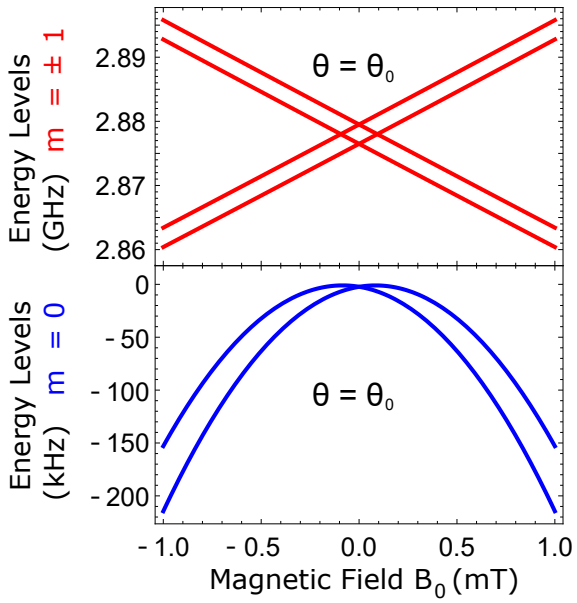


Figure 3.11: $NV^-$ **hyperfine energy spectrum**. For $\mathbf{B}_0$ applied along $\theta = \theta_0$. The red corresponds to $m_s = \pm 1$, and the blue $m_s = 0$.

$|m_s = 0, \leftarrow_N\rangle$ is plotted (blue curve), showing a much larger energy splitting than expected from $\gamma_n$ (red curve). This is due to the non-secular terms of the hyperfine interaction, which lead to a renormalization of the gyromagnetic ratio when $\mathbf{B}_0$ is applied along X [49, 74]. This effective gyromagnetic ratio is $\gamma_{n\perp}/2\pi = -75.0247$ MHz/T as can be seen from Fig. 3.12.

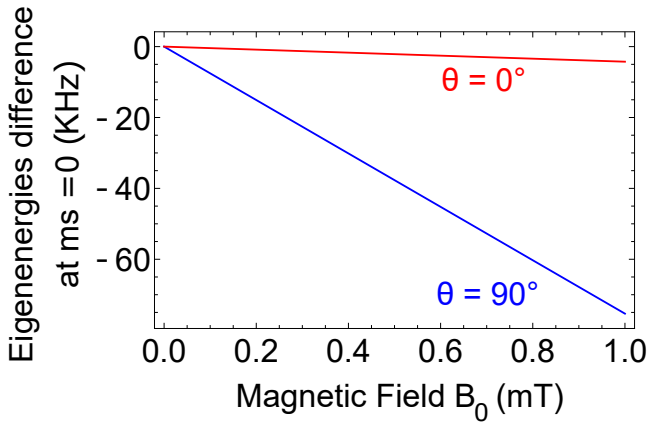


Figure 3.12: **Effective perpendicular nuclear gyromagnetic ratio**

In the $m_S = 0$ state, the nuclear spin is thus described by an effective Zeeman Hamiltonian $H^{m_s=0}/\hbar = \gamma_n B_0 \cos\theta I_Z + \gamma_{n\perp} B_0 \sin\theta I_X$. The eigenstates of this Hamiltonian are

$$|+_N\rangle = \cos\psi\,|\uparrow\rangle + \sin\psi\,|\downarrow\rangle \tag{3.11}$$

$$|-_N\rangle = -\sin\psi\,|\uparrow\rangle + \cos\psi\,|\downarrow\rangle \tag{3.12}$$

with

$$tan\psi = \sqrt{1 + \frac{\gamma_n}{\gamma_{n\perp}}^2 \frac{1}{\tan\theta^2}} - \frac{\gamma_n}{\gamma_{n\perp}} \frac{1}{\tan\theta}$$

and the difference between their energy is

$$\hbar\omega_{NO} = \sqrt{\gamma_n^2(B_0\cos\theta)^2 + \gamma_{n\perp}^2(B_0\sin\theta)^2} \tag{3.13}$$

For the following, we note in particular that if the NV spin system is prepared in the states $|m_S = 0, \uparrow_N\rangle$ (resp $|m_S = 0, \downarrow_N\rangle$), it is not stationary and evolves periodically with frequency $\omega_{NO}$ towards state $|m_S = 0, \uparrow_N\rangle$ (resp $|m_S = 0, \uparrow_N\rangle$). In the rest of this thesis we will use both the stationary basis $|m_S = 0, \pm_N\rangle$, and also the non-stationary basis $|m_S = 0, \uparrow_N / \downarrow_N\rangle$, as depicted in Fig. 3.13.

As explained in Chapter 2, under a microwave drive, the Rabi frequency between two levels $|i\rangle$ and $|j\rangle$ is proportional to the matrix element $\langle i|S_X|j\rangle$, implying that only nuclear-spin-conserving transitions are allowed.

These transitions are shown in Fig. 3.13a, for the levels $m_S = 0$ and $m_S = +1$ by simplicity (the same is true with state $m_S = -1$). To understand spectroscopic consequences, we must give a few numbers. We will work at low magnetic fields $\mathbf{B}_0 < 2mT$ , so that the level splitting between $|+1, \uparrow_N\rangle$ and $|+1, \downarrow_N\rangle$ is $\sim$ 3MHz, whereas the level splitting between $|0, +_N\rangle$ and $|0, -_N\rangle$ is on the order of few tens of kHz, or <150kHz. On the other hand, the typical bandwidth of the microwave pulses used in this work is around 500kHz - 1MHz. Our pulses do not resolve the ground-state splitting, but easily resolve the excited state splitting. In a Ramsey fringe experiment in particular, the system is initialized in the electronic state $m_S = 0$, with the nuclear spin unpolarized. Pulses will therefore excite equally well both orange transitions (or both green transitions) shown in Fig. 3.13b. This leads to two Ramsey fringe patterns at frequencies separated by $\omega_{NO}$, and to beatings in the final signal, as seen in Chapter 4.

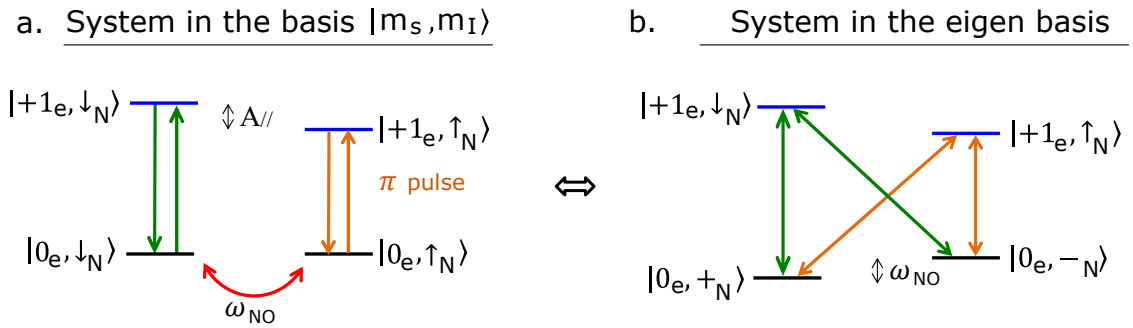


Figure 3.13: **Energy levels representation sketch**. Energy levels and transitions in $m_s = 0$ and $m_s = +1$ (a) in the $|m_s, m_i\rangle$ basis (b) in the energy basis (the $m_s = -1$ manifold are not shown, for clarity.). As the transitions are nuclear-spin conserving, 4 transitions are allowed when $\theta \neq= 0$.

## 3.6 Magnetometry using NV centers

Magnetometry using NV centers [75] has been widely used since the last decade because of NV center nanoscale spatial resolution as well as their optical and spin

properties at room temperature associated with long coherence times.

Maze et. al. [57] has used single NV near the surface of either a ultra-pure bulk single-crystal diamond or located within a diamond nanocrystal to sense an externally applied AC magnetic field. Sensitivity of $0.5\mu T/\sqrt{Hz}$ was achieved for diamond nanocrystal with diameter of 30 nm.

Balasubramania et. al. [76] Degen et. al. [56], Taylor at. al. [58] and Maletinsky et. al. [77] has used single NV in a diamond tip of an atomic force microscope (AFM) cantilever as a probe spin near a substrate to measure the presence of local magnetic fields on the surface. NV center magnetic field sensing proposed by Taylor at. al. [58] reached a sensitivity of $3nT\sqrt{Hz}$ using a single NV center of $T_2^* \sim 1\mu s$ and $T_2 \sim 300\mu s$. Maletinsky et. al. [77] has used high-purity diamond nanopillars as AFM tips and achieved coherence times as long as $\sim 75\mu s$. In [77] magnetic domains with width of 25 nm could be imaging and a sensitivity of $56nT/\sqrt{Hz}$ at 33 KHz was demonstrated.

Magnetometry by detection of the spin state of high-density nitrogen-vacancy ensembles in diamond at 75 K has been demonstrated by Acosta et. al. [78] with a noise floor of $7nT\sqrt{Hz}$ at 110 Hz.

What all these NV magnetometry have in common is the use of the Zeeman shift of the electron spin levels to infer $\mathbf{B}_0$ . As explained in Sec. 3.2, this method gives access only to the $\mathbf{B}_0$ component that is parallel to the NV axis, $B_0 \cos\theta$ , and not to its orthogonal component.

In this project, we have used the NV magnetometer properties to determine their position with respect to a nanometric wire. A full description of the local magnetic field requires, however, the determination of $B_0$ perpendicular to the Z axis, $B_0 \sin\theta$ , as well. Although $B_0 \sin\theta$ detection could be achieved using an ensemble of different NV centers orientations it has a price to pay: the reduction of the spacial resolution because the NVs have to be enough apart in order to be resolved optically.

In this Thesis we have rather opted for a single NV method, proposed by Chen et. al. [74] to determine both components of the magnetic field with respect to the NV Z axis. $B_0 \cos\theta$ is determined by Zeeman interaction, as usual, while $B_0 \sin\theta$ is inferred thanks to the Zeeman shift of the $^{15}N$ nuclear spin. Thus, the high resolution is guaranteed and we can determine the magnitude and angle of $\mathbf{B}_0$ .

Fig. 3.14 illustrates the pulse sequence used to determine $B_0 \sin\theta$ . After initialization of the electron spin in $|0_e\rangle$ by a green laser pulse, the NV is found with equal probability in states $|0_e, \uparrow_N\rangle$ and $|0_e, \downarrow_N\rangle$. A nuclear-spin-state-selective pulse is then applied to the electron spin. This pulse transfers all population from $|0_e, \uparrow_N\rangle$ into $|+1_e, \uparrow_N\rangle$. Whereas the $|+1_e, \uparrow_N\rangle$ is an eigen-state (and therefore does not evolve in time), $|0_e, \downarrow_N\rangle$ is coupled to $|0_e, \uparrow_N\rangle$, as seen in the previous section, leading to an oscillation at frequency $\omega_{NO}$. This yields the transverse $\mathbf{B}_0$ component

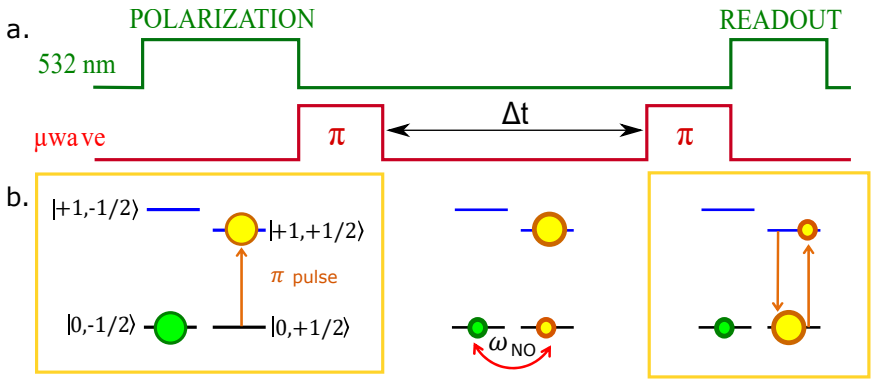


Figure 3.14: **Nuclear oscillation sequence a.** Laser (green) and microwave (red) pulse sequence, with $\Delta t$ the delay time between two pulses. **b.** Time evolution of spin state populations during the sequence.

through :

$$B_0 \sin\theta = \frac{\sqrt{\omega_{NO}^2/2\pi - \gamma_n^2 \cdot B_0 \cos\theta^2}}{\gamma_{n\perp}} \tag{3.14}$$

This oscillation is detected by letting the system evolve for a variable delay $\tau$, followed by another $\pi$ - pulse which maps the nuclear spin oscillation into an oscillation between $|0_e\rangle$ and $|1_e\rangle$ detectable by a pulsed laser readout. Throughout this thesis, we label these oscillation as 'Nuclear Oscillations'. Fig. 3.15a shows typical data curve of Nuclear Oscillations and Fig. 3.15b is the $B_0 \sin\theta$ inferred from this method. These image was extracted from Chen et. al. [74].

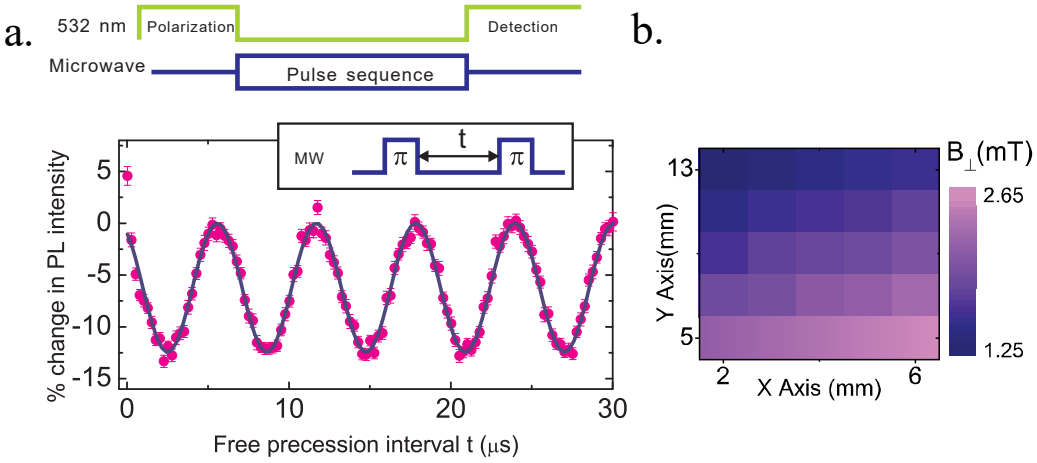


Figure 3.15: $NV^-$ **nuclear oscillations**. **a.** Top: Pulse sequence with green laser pulse initialization followed by a $\pi$ pulse, free induction time and the readout that consists in another $\pi$ pulse and green laser pulse. Bottom: Nuclear oscillation.; **b.** Magnetic field calculated from the Nuclear oscillations [74]

## 3.7 Relaxation times

Beyond the ODMR at room temperature, another attractive NV property is their long electronic spin coherence time. As discussed in Chapter 3, the spin coupling with the environment leads to decoherence. These losses are characterized by the time scales $T_1$ and $T_2$, longitudinal and transverse relaxation times respectively, which are the figure of merit of any quantum applications because they limit the operational time of the quantum protocols.

At room temperature, the most relevant $T_1$ relaxation mechanism involves spin-lattice interaction and it is typically $\sim 4ms$. In general, $T_2$ is shorter than $T_1$, and is dominated by magnetic interactions with the environment.

In a bulk diamond the spin phase coherence is limited by interaction with paramagnetic impurities bath or hyperfine interaction with the nuclear spin bath. The mains source of impurities are listed below:

1. Other NV centers with concentration [NV]

2. Neutral nitrogen atoms (non-converted to NV) implanted in the lattice. These "P1 centers" have a spin 1/2 [79]

3. $^{13}C$ Carbon 13 atoms in the lattice, with concentration [$^{13}C$ ]

4. Moreover, clusters of vacancies can be paramagnetic and therefore act as a decoherence source.

The impurities concentration depends on the diamond fabrication process that can be either *High Pressure High Temperature*, HPHT, or *Chemical Vapor Deposition* (CVD) techniques. The CVD NV environment is schematically shown in Fig. 3.16.

Although it is now possible to produce high purity diamonds via HPHT, typically diamond grown by HPHT has $[P1] \sim 10^2 ppm$ and coherence times values of $T_2^* \sim 300ns$ and $T_2 \sim 3\mu s$ [80, 81], while CVD growth can produce ultrapure diamond with $[N] \sim 1ppb$. At such low $[N]$, the coherence time becomes limited not by the electronic spin bath but rather by the nuclear spin bath of the natural concentration of $^{13}C$ (1.1%). NV centers into such diamonds posses coherence time values up to $T_2^* \sim 500\mu s$ [70] and $T_2 \sim 650\mu s$ [82]. Its environment is illustrated in Fig. 3.16 a.

To go beyond and enhance even more the coherence times, one can isotopically purify the diamond to reduce the nuclear spin bath. Thus, the coherence times can reach values as $T_2^* \sim 500\mu s$ and $T_2 \sim 2ms$ [83], Fig. 3.16 b. This isotopically purified layer is presented in some of our samples that were grown by T. Teraji at the National Institute for Material Science (NIMS) in Tsukuba.

Moreover, our strategy to obtain shallow NV center precisely positioned on the diamond surface involves ion implantation that gives rises to additional non-controlled defects in the diamond crystal such as the carbon Vacancies, for instance. Thus, it is also a source of decoherence.

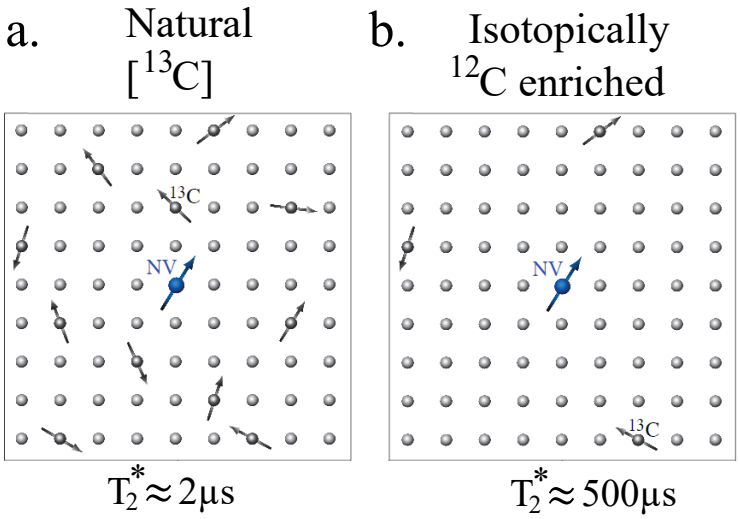


Figure 3.16: **Spin bath environment in diamond grown via CVD process**. **a.** The magnetic impurity bath is imitated to the natural concentration of $^{13}C$ nuclear spin bath. Typically, $T_2^* \sim 2\mu s$ and $T_2 \sim 500\mu s$ ; **b.** CVD diamond isotopically enriched with $^{12}C$ ($I^{^{12}C}$). NV centers into diamonds with $[^{13}C] \sim 0.01\%$ can reach $T_2^* \sim 500\mu s$ and $T_2 \sim 2ms$. Image adapted from [70]

## 3.8 Shallow NV centers and charge state stability

Unfortunately, shallow implanted NVs have been shown to have a number of properties degraded compared to NVs in the bulk [84] . First, shallow NVs were shown to have coherence times shorter than in the bulk. This was attributed to the presence of a bath of paramagnetic impurities located at the diamond surface [85], whose physico-chemical nature remains unknown. Second, shallow NVs were also shown to have their charge state less stable than bulk NVs [86]. A recent study demonstrated that this is due to the possible presence of an electron acceptor state at the diamond surface, which enables NV- ionization by tunneling from the NV to the surface state. This charge state instability has several undesirable consequences for our project. Here, the most noteworthy is that the contrast of the ODMR signal is reduced compared to bulk NV centers, and also can vary from NV to NV, as well as in time.

# Chapter 4

# Realization of an array of precisely placed NV centers with long coherence times

We now describe the realization of an array of shallow NV centers with long coherence time that was accurately positioned with respect to the etched marks on the diamond substrate. Those diamonds, in turn, were carefully cleaned to possess low microwave losses. Five diamond chips have been used and they were label as: *"d01"*, *"d02"*, *"d02a"*, *"d03"* and *"2sideimpl"*. The NV centers were created artificially via $^{15}N$ ion implantation followed by annealing.

In this chapter we will describe the chosen strategy NV alignment followed by all the fabrication process. Then we describe the experimental setup for the NV characterization, and we present the results.

## 4.1 Alignment strategy

NV centers in diamond may arise either from natural or artificial process. In the first case, atmosphere's Nitrogen incorporation into the diamond lattice results in NV centers mainly formed by $^{14}N$ and randomly spread out into the crystal. Artificial NV centers, however, allows us to better control the NV positioning and the Nitrogen isotope as well. Artificial NV centers can be formed Nitrogen ions implanted through masks of various types (pierced AFM tip [87, 88], resist masks [89], metallic masks [90]), or by direct implantation with a Focused-Ion-Beam [91]. Since the figure of merit of all this process is the alignment between the NV and the etched marks on the diamond chip, we have chosen ion implantation to produce single $NV^-$ [92] formed by $^{15}N$. The advantages of this process includes: simulate the ion depth a priory as well as to distinguish between the natural NV, at arbitrary depth, and the implanted shallow NV center, thanks to the N isotopes spectroscopy signature, as explained on the previous chapter.

With usual ion implantation, the ion position on the sample is random. The confocal microscope is used to measure the PL of the formed NV center. However, it would be necessary to determine the relative position of the Gaussian emission profile of a NV with respect to an alignment mark with $\sim$ 10nm resolution, which

seems difficult given the piezoelectric stack hysteresis and drifts. On the other hand, a resist mask can be used to restrict the ion implantation through nanometric size holes, providing a nanometric position resolution if the resist mask is patterned with electron-beam lithography. However, due to the small yield of N - NV conversion, this technique alone is not able to determine which hole contains the NV.

In light of this, among the different existing alignment techniques, we chose an hybrid strategy combining an e-beam mask and confocal microscope. More precisely, the strategy was to fabricate a resist mask with holes in the same machine (e-beam at 100 kV) that was used to pattern the alignment marks and thus, guarantee their alignment with the machine incertitude of $\sim 20nm$. The NV center were implanted through these holes and characterized at room temperature using the confocal microscope. In this way, we precisely measure the NV position, and we are moreover able to characterize the NV coherence time at room-temperature, enabling to select a good candidate for the low-temperature measurements.

Beyond the challenging positioning, we have to deal with the charge state instability of shallow NV centers. As commented in the previous chapter, the NV can get ionized due to the presence of acceptor traps at the surface on the surface.

To overcome this difficulty we have designed two different mask patterns. First, a grid of holes of $\sim 40nm$ of diameter, to produce single NV centers. Second, a grid of lines set. These lines were as narrow as 80 nm and as long as $3\mu m$ and the set is composed by four lines separated by 150 nm. The goal here was to guarantee the some NV centers will remain on its negative charge state even after the nanowire fabrication.

## 4.2 Fabrication process

The fabrication process is shown in Fig. 4.1 and the steps sequence is listed below:

1. Substrate, Fig. 4.1a:
   (a) $^{12}C$ isotopically purified layer,
   (b) Etched marks on Diamond, Fig. 4.1b.
2. NV implantation:
   (a) Electron beam lithography mask, Fig. 4.1c, and lithograpy Fig. 4.1d,
   (b) $^{15}N$ ion implantation, Fig. 4.1e.
3. Cleaning;
4. Annealing, Fig. 4.1f.

All these steps will be described in the following sections. In the fabrication process I did the resist mask used to etch the diamond and the cleaning; I also participated in the implantation and annealing process with Sébastien Pezzagna (Leipzig University) and Anne Forget (SPEC), respectively.

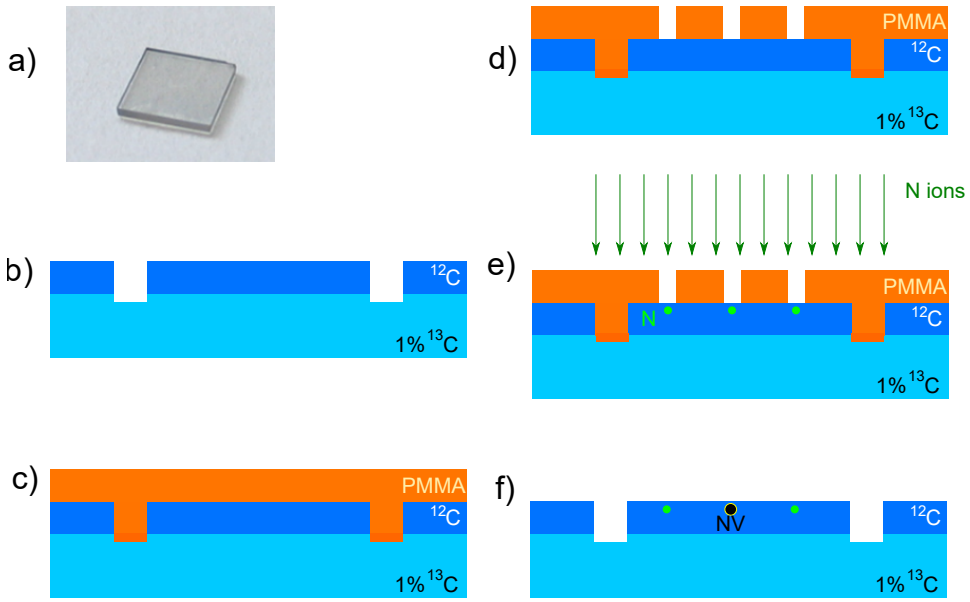


Figure 4.1: **NV implantation summary**. **a.**Photograph of the diamond chip. **b.** Profile of a CVD diamond sample with etched marks; **c.** Diamond covered by a resist (PMMA); **d.** PMMA profile after been exposed by electron beam lithography. Holes with nanometric dimensions are created at specific position regarding to the etched marks on diamond; **e.** N implantation. The energy and fluency of the Nitrogen ions are controlled such that they a blocked by the PMMA. The ions will be implanted into the diamond only if it pass though the nanometric holes on PMMA. **f.** The conclusion of the fabrication is reached by favoring an Carbon vacancy to move next to the implanted N. This is done by annealing the sample.

## 4.3 The substrate

The substrates of all samples were CVD grown diamond chips purchased from Element 6 with Nitrogen concentration $< 5ppb$ (ppb = parts per billion). On top of samples *d02a* and *d03*, a layer of thickness $\sim 1$ micron of diamond isotopically enriched in $^{12}C$ was grown by CVD by T. Teraji at NIMS. Because the low concentration of nuclear spins, those samples present long coherence times and therefore, are dedicated to the low temperature measurements.

### *Etched Marks in Diamond*

This project requires an absolute position referential marks in order to perform the alignment between the NV centers and the LC resonator inductive nanowire. Since these two process requires different lithography steps, those marks must resists to several chemicals treatments. That is why we decided to use etched marks on diamonds. The marks were fabricated in C2N. The patterning was done using an electron-beam writer with 100kV accelerating voltage. The etching was done with a proprietary recipe of oxygen etching in a RIE, using an aluminum mask. Three different types of marks are etched into the diamond:

1. *Alignment:* square marks $10\mu m$ x $10\mu m$ for e-beam lithography alignment;

2. *Identification:* array of $1\mu m$ x $1\mu m$ marks, designed with a code enabling the identification of the sample area in a confocal microscope scan;

3. *Label:* samples *d01*, *d02a* and *d03* have their names etched into the chip.

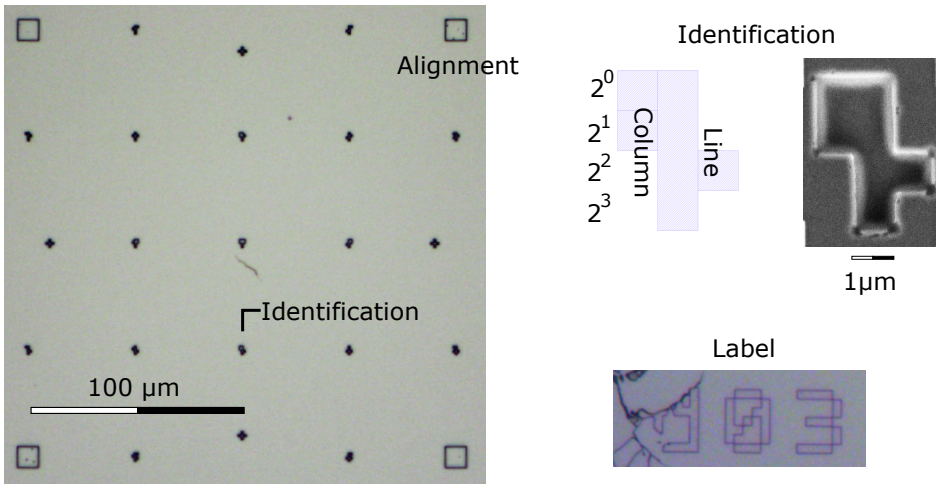


Figure 4.2: **Diamond Etched marks.** Left: Optical microscope of sample d03. Right: Zoom on identification marks (design and SEM image) and label mark (optical microscope).

## 4.4 NV implantation

The NV centers used in this thesis are created via ion implantation. Ion implantation consists in bombardment of a solid target with energetic ions (typically between 1keV - 1MeV). The ions are scattered inside the crystal. Their penetration pattern is not directional but rather three dimensional distribution, strongly dependent on their interaction with the target material, and usually represented by an Gaussian.

The figure of merit of this process are two: 1) the ion energy which determines the ion depth; and 2) the number of ions per unity of area, the so called fluency, which sets the number of formed NVs. For energy implantation in the 5-20keV as used in this thesis, the N to NV conversion yield is in general around a few percent [93].

We aimed at fabricating single and small ensembles of NVs well isolated in diamond. Thus, we chose to implant ions throughout nanometric holes (or lines) pierced in a resist mask because we want to protect all the diamond surface except at the desired NV position reducing, therefore, the probability of carbon vacancies creation nearby the NV which leads to to a considerable reduction in the coherence time.

The resist used is the polymethyl methacrylate (PMMA) and it can be patterned

with nanometric resolution via electron beam lithography. Nonetheless, the efficiency of this mask require a match of resist thickness and ion energy. At the beginning of my PhD, the project's state-of-the-art of the array of shallow $NV^-$ centers into a purified CVD diamond substrate $^{12}C$ - enriched with low microwave losses (*d00*) is shown in the PL color map image on Fig. 4.3. All the bright spots corresponds to at least one NV center. The resist thickness was not sufficient to stop the nitrogen ions, and as a result NV centers were found everywhere on the sample. In order to overcome this problem, this thesis begins with the testing several implantation parameters and characterizing the formed NV centers.

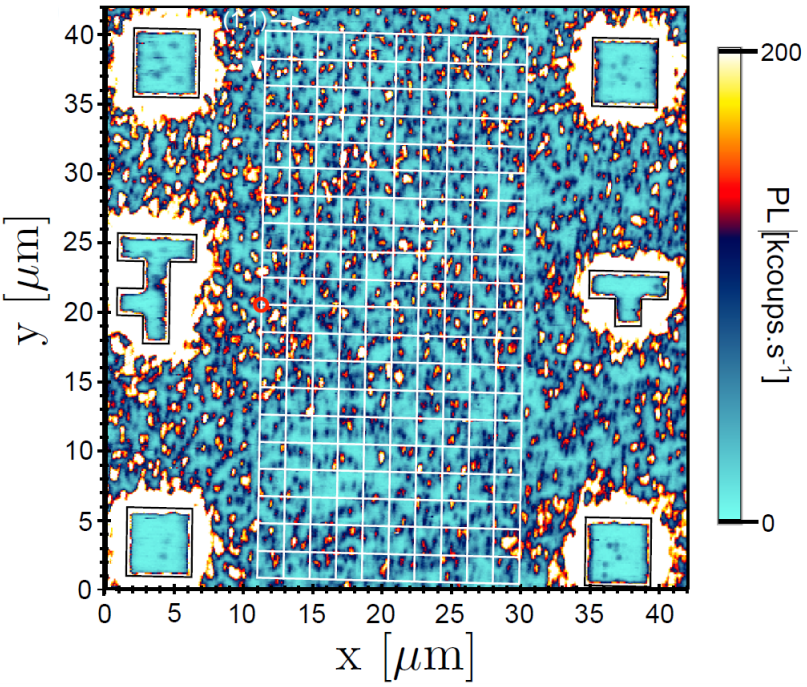


Figure 4.3: **Confocal microscope image of the sample d00**. Photoluminescence (PL) color scale graphic of d00 diamond sample surface. The light blue corresponds to few photons (basically the background) while the bright spots corresponds to at least on NV center. On the both sides, sharp geometric square-like forms corresponds to the etched marks on diamond. The white continuous line grid is a guide to the eyes in order to recognize where the NV centers were supposed to be formed. As one can see, the implantation has failed, because there are NV centers in everywhere.

### *Determining the implantation parameters*

Based on STRIM simulations, made by Reinier Heeres, that shown a typical penetration depth into PMMA of around 60 nm Fig. 4.4a at Nitrogen ions energy of 7.5 keV, we fixed the resist thickness as 120 nm to ensure that the ions would be stopped Fig. 4.4a. At the same energy, the ion passing through the holes is expected to be implanted in diamond no deeper than 20nm Fig. 4.4b.

We then performed a series of tests, using a natural-abundance CVD sample, to determine the implantation yield. An array of holes was implanted with a fluence of 2400 N/$\mu m^2$ and holes of 100nm diameter. Using the annealing at 900° C, we

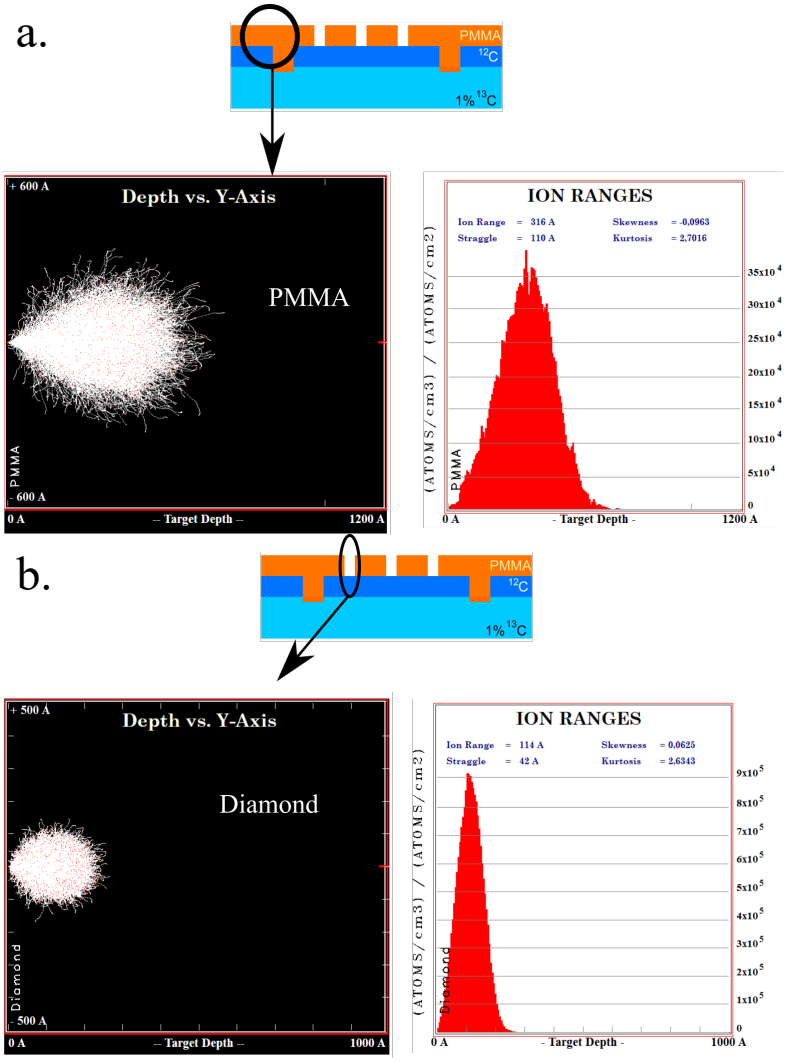


Figure 4.4: **STRIM simulations of penetration profile of the Nitrogen ions**. **a.** In the PMMA surface, the ion penetration depth is around 60 nm; **b.** In the diamond, with the same energy ions, the penetration depth is rather 20nm.

consistently found an implantation yield of 4-5%.

In light of this, we decided to implant on average one Nitrogen atom per hole. This should result in only 5% of the holes containing a NV center, which is not a problem since we characterize them a posteriori. In order to do that, we have changed the mask fabrication place to C2N where the electron beam lithography works at 100 keV and allowed us to produce holes of 20-30nm side. Finally, with an yield of $\sim 4-5\%$ and hole area of $400nm^2$ the Fluency should be around 3000 $\frac{N}{\mu m^2}$ to reach our target.

### *Implanted mask*

A sketch of the implantation mask is shown in Fig. 4.5. Here the design is composed by only two type of cells contain either a grid of holes or a grid of lines. The first is dedicated to single $NV^-$ detection and is based on holes of separated by 1.5 $\mu m$.

The grid of lines Fig. 4.5b aims at being more flexible on the alignment process. It consists is sets of 4 lines separated by 150 nm. As will be shown below, we verify our implantation mask by evaporating metal after ion implantation and just before mask removal. In this way we ensure that the implantation mask was as desired when the ions were implanted. Using a 100keV e-beam lithography machine located at C2N, we achieve holes of 20-30nm diameter (see Fig. 4.6. The lines turned out to be wider than desired, around 70nm, but this is not an issue since their goal is anyway to release the alignment requirements.

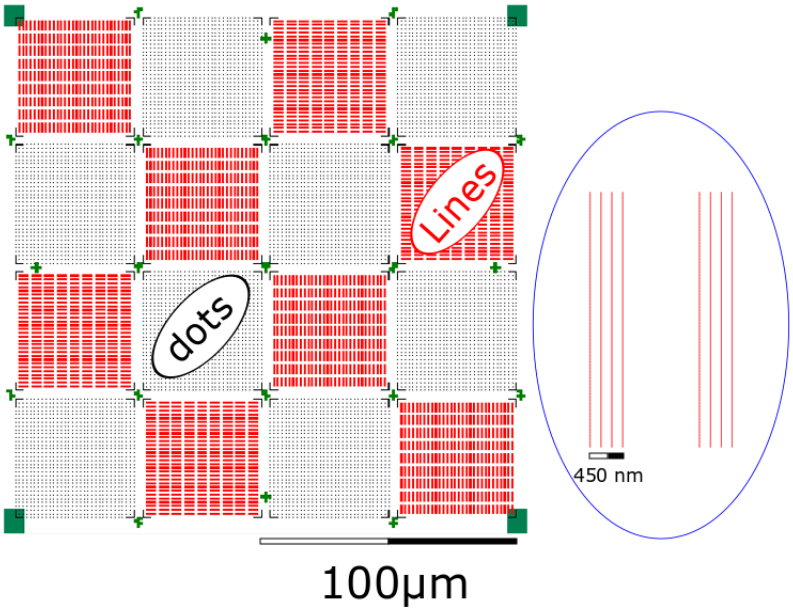


Figure 4.5: **Implantation mask design**. gds file sketch of the implantation mask. It is composed by 16 cells: half of them composed by a grid of holes and the other half made by a grid of lines.

The mask was made with PMMA coated with 20 nm of Aluminium used as a discharging layer. The pattern was written into the PMMA mask using a 100 kV electron beam machine with automatic alignment with respect to the etched marks. This is a very import step because it determines the absolute position of the NV centers on diamond. Moreover all the alignment afterwards is based on the same marks. After e-beam exposure, the aluminum discharging layer is first removed, followed by the mask development. The detailed mask recipe is shown in the Appendix A.

### *Ion implantation*

The ion implantation was done at the Department of Nuclear Solid State Physics, Leipzig University, Germany, with the collaboration of S.Pezzagna. Selected by an mass spectrometer, the ions arise from the $^{15}N_2$ isotope allowing us to distinguish the implanted NVs from the natural ones. The implantation energy was 7.5 keV since we target at a depth around 20 nm. The Nitrogen fluency was between 2210

and 2650 $N/\mu m^2$.

In order to ensure that the pattern had turned out properly, the PMMA mask was checked just after the ion implantation. For that, we evaporate 5 nm of Ti followed by 30 nm of Au throughout the mask before dissolving it in acetone and looked the gold pattern a *Scanning Electron Microscope* (SEM). Fig. 4.6 shows the SEM images. It turns out that the average holes diameters was around 22-25 nm while the lines appeared 70nm - 95nm thick. Finally, the Ti and Au was removed with Piranha acid followed by $K_2I_2$ solution.

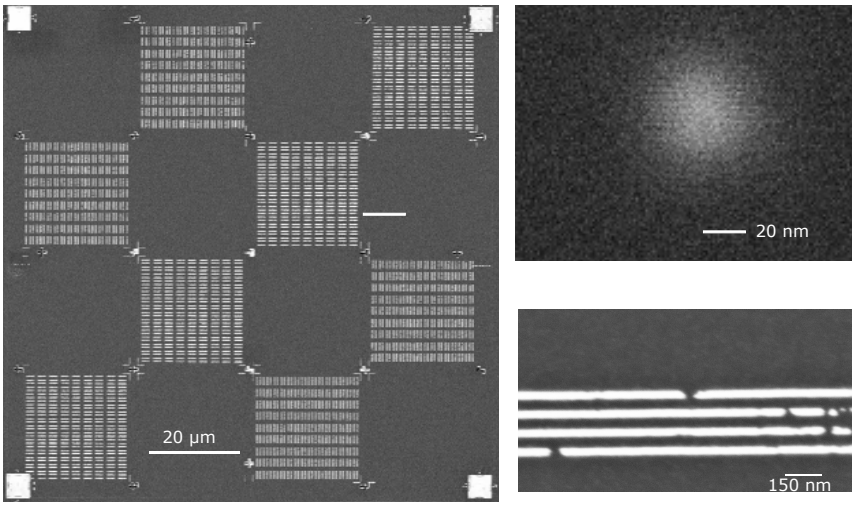


Figure 4.6: **Implantation mask validation.** SEM image of the implantation mask after gold evaporation and liftoff

## 4.5 Annealing

After the Nitrogen implantation, annealing is required in order to form the NV center by promoting the motion of vacancies created by implantation damage, and also to heal as well as possible implantation damage. Annealing parameters have been studied thoroughly. Although annealing temperatures of 900°C have been often used in the past, it was shown in recent years that a higher temperature enables better implantation damage healing; this is however delicate as it can lead to slow burning of the sample surface, which is detrimental for shallow NVs. Most of our samples were annealed at 900°C for 2 hours except d02a sample which was annealed at 1100°C for 2 hours. The annealing was performed at SPEC, in the chemistry lab of D. Colson and A. Forget.

## 4.6 Sample cleaning

The diamond chip cleaning is a very important procedure performed at different fabrication steps and thus, with different proposes. Here we list the indispensable ones:

1. *After* $^{12}C$ *purified layer* in order to remove the graphite produced during this process. We use a boiling mixture of three acids: Nitric, Sulfuric, and Perchloric, in proportion 3/4/1.

2. *Fabrication preliminaries*: The substrate must be perfectly clean on its surface in order to be coated with the resist. The usual sequence is: Hot Acetone, Alcohol Isopropanol, and bath in a specific acid which combines Sulfuric Acid ($H_2SO_4$) and Oxygen Peroxide ($H_2O_2$), known as *piranha solution* due to its high efficiency of cleaning.

3. *Before confocal Characterization*. The goal here is to reduce as much as possible the photoluminescence background on diamond surface after ion implantation. Additionally to the sequence above, we perform a n Oxygen Plasma to remove any eventual remnant PMMA residue.

4. *Reduce diamond microwave losses*. The same process that removes the Graphite.

## 4.7 Experimental setup

***Sample holder***

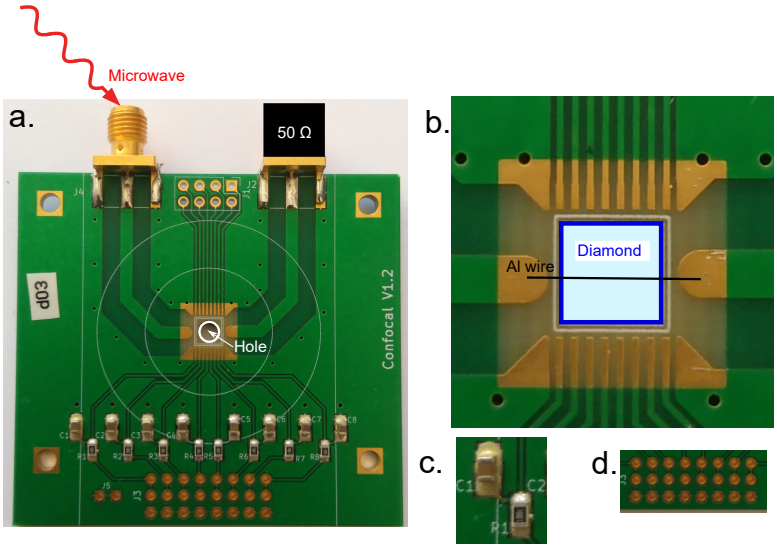


Figure 4.7: **Sample holder. a.** PCB used to control the NV centers on diamond chip, in green. In Black is represented the 50 Ω resistor used to avoid microwave reflections. **b.** Zoom. The diamond is represented in blue while the Al the wire bounding is shown in black. **c.** Condensors and resistors used to protect the on-chip nanowire. **d.** Vias used to ground and and pass a current.

In order to perform the optical measurements, we use a *Printed Circuit Border* (PCB) as a sample holder, designed by Reinier Heeres, as the one shown in Fig. 4.7a. The microwave (MW) pulses are sent through the SMA connector and are absorbed by a 50 Ω resistor after crossing the sample. Note that there is a hole on the center of the PCB and in the middle of the MW path. This hole was designed to be behind the sample in order to avoid any undesired laser reflection from the PCB.

The chip is glued in the center of the holder and it is represented in blue in Fig. 4.7b. To deliver the microwave signal to the NV centers, two configurations can be used. In the first one, we wire-bond a 30 $\mu m$ aluminum wire across the diamond, which does not need any waveguide patterning on the sample. In the second one, an on-chip waveguide is first deposited on the diamond, and wire-bonded to the PCB. The first configuration corresponds to the one used throughout this chapter and the second will be explored on the measurements of the next chapter.

As will be seen in the next chapter, we will also pass a DC current through a fragile Al nanowire. In order to protect it, the PCB includes RC filtering (see Fig. 4.7c). Finally, we have the PCB vias, Fig. 4.7c, dedicated to ground and feed the current.

### *Applied magnetic field*

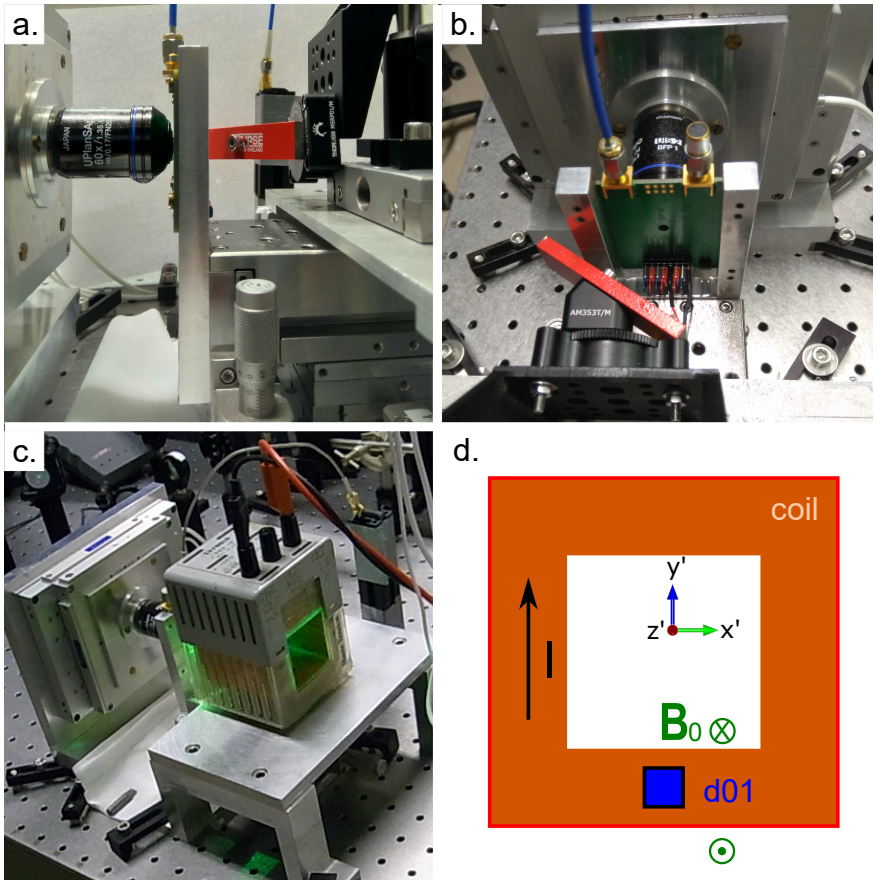


Figure 4.8: **Applied magnetic field setup in the confocal microscope at room temperature.a.** Magnet (lateral view). **b.**Magnet (top view). **c.** Square coil. **d.** Sketch of the magnetic field generated by the coil on the diamond chip.

The applied magnetic field configurations used throughout this thesis are:

- $\mathbf{B}_0$ at $\theta = 0°$. A photo of the experimental setup is shown on Fig. 4.8a and Fig. 4.8b. A permanent magnet was carefully place behind the sample holder in a rotational base station. Based on the diamond chip crystallography axis, the magnet was aligned parallel to one of the NV orientations.

- $\mathbf{B}_0$ at $\theta \sim 54.7°$. As show in Fig. 4.8c, the magnet is replaced by a square coil and the sample is in at the middle bottom of the coil, as illustrated in Fig. 4.8c. In such configuration, the resulting magnetic field applied in the sample is approximately parallel to y' axis at the diamond surface.

## 4.8 Characterization at room temperature

Now we present the first results of this work: the fabricated grid of implanted NV centers with long coherence time.

***NV center grid***

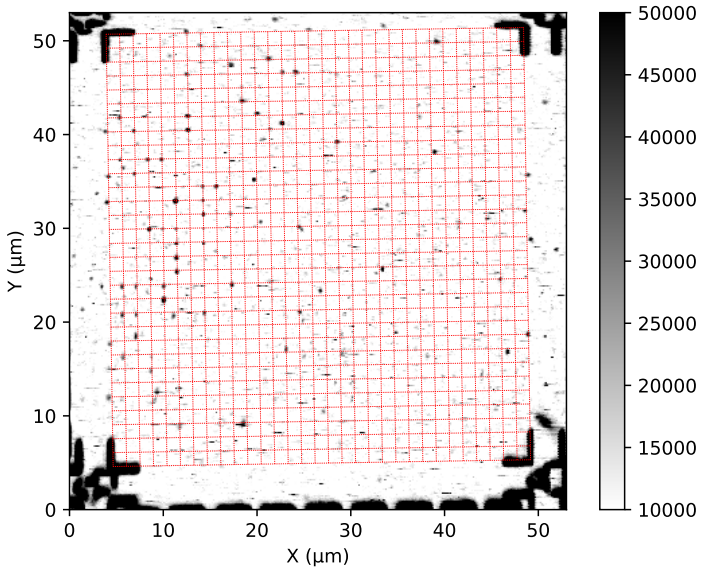


Figure 4.9: **Grid.** Confocal microscope color image in gray scale. The darker spots corresponds to at least one NV center. In red is shown a fit of the designed grid.

Fig. 4.9 shows a PL color map of one implantation cell of *d03* sample. In the same image it is shown in red the plot of the designed implantation mask grid. The NV centers are expected to be at the crosses of the red lines (a guide to the eyes). From these images one reach two conclusions: 1) The implantation mask has worked properly, since only a few NV centers are found, and a number of them are clearly located on the grid as desired. 2) The yield is $\sim 2\%$ in agreement with the literature.

***Single NV microwave characterization***

Now, let's focus on a single NV center in this grid. Fig. 4.10 shows its PL image. The typical collected PL color map corresponds to a two dimensional Gaussian in the plan of diamond surface whose spot size is limited by light diffraction and is around 300nm. Approximately 70 000 photons are collected per second.

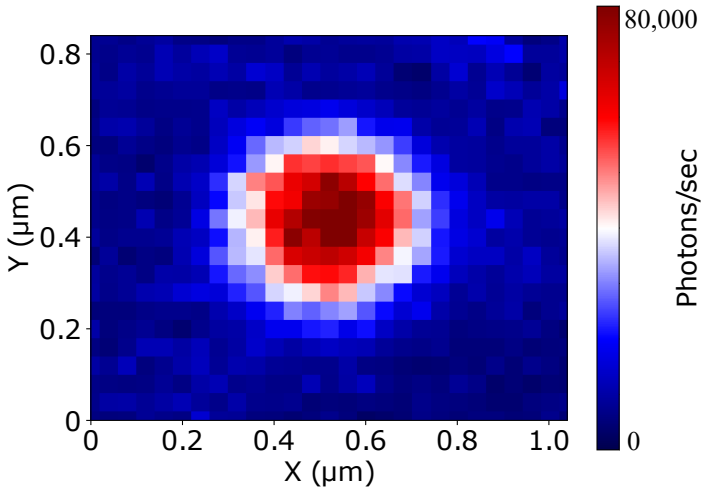


Figure 4.10: **Confocal microscope image of a single NV center**. The color scale indicates the number of photons collected per second

To determine whether a NV is unique we have measure the autocorrelation function $g_2(\tau)$ between the PL intensity detectors given by:

$$g_2(\tau) = \frac{\langle I_1(t) I_2(t+\tau) \rangle}{\langle I_1(t) \rangle^2} \tag{4.1}$$

where $I_1$ [$I_2$] in the PL intensity collected by detector 1 [2] at a time t [$t + \tau$].

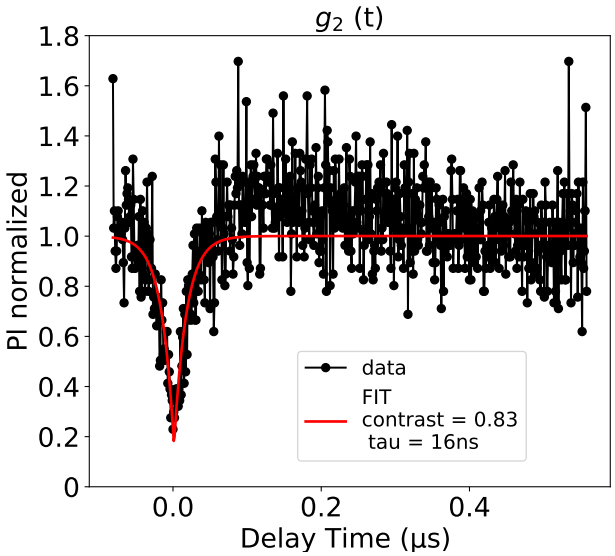


Figure 4.11: **Auto-correlation function $g_2(\tau)$ of a single NV**. The data are represented in black and the dip fit indicates a contrast of 83% at $g_2(\tau)$ indicating that the emitter is unique

Measuring g2 enables to determine the number of NV centers located in the laser spot. Indeed, it can be shown that for n emitters, we should have $g_2(0) = 1 - 1/n$.

Because the NV emission is accompanied by background photons, the measured $g_2(0)$ can be larger than this theoretical value. Therefore, we get an upper bound of the number n of emitters by determining n such that $1-1/n < g_2(0) < 1-1/(n+1)$. In particular, if $g_2(0) < 1/2$, we can be certain that only one NV center is measured. This is the case in the data shown in Fig. 4.10 for instance.

One can confirm by the spectroscopy shown in Fig. 4.12 that it is an implanted NV because its microwave transitions corresponds to the energy spectrum of NV electronic spin coupled with $I^{15}N$ via hyperfine interaction. Black corresponds to the data and the red is a Lorentzian fit. The spectroscopy contrast is $12 \pm 1\%$ with Full Maximum at Half Width (FMHW) $\sim 1$ MHz, limited by the microwave $\pi$ pulse duration ($1\mu s$). This why we can resolve only 4 dips instead of 8, which should correspond to all possible transitions described on Fig. 3.13, as explained in the previous section.

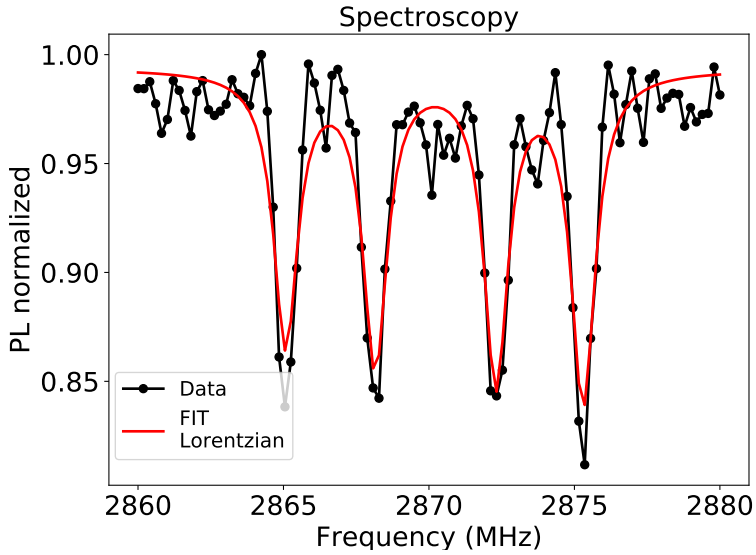


Figure 4.12: **NV Spectroscopy**. Photoluminescence (PL) as a function of the frequency $\omega$ of the applied microwave. The lowest (highest)-frequency two transitions are between $m_s = 0$ and $m_s = +1$ ($m_s = -1$).

The $\pi$ pulse duration, on its turn, is determined by Rabi measurement as the one shown in Fig. 4.13. Note that the Rabi amplitude was constant in time up to 20 $\mu s$. This was used as a criteria to selection of the NV whose coherence time would be measured: NV centers whose Rabi measurements presenting decay in time was excluded.

### *Coherence time*

The last characterization measurement is the Ramsey pulse sequence to determine the NV center coherence time. Fig. 4.14 and Fig. 4.15 show the Ramsey output for single NV centers implanted at two different samples: with (*d03*) and without (*d02*) the high isotopically purified $^{12}C$ respectively. The beating seen at Fig. 4.14 are due to the hyperfine interaction as explained in previous chapter.

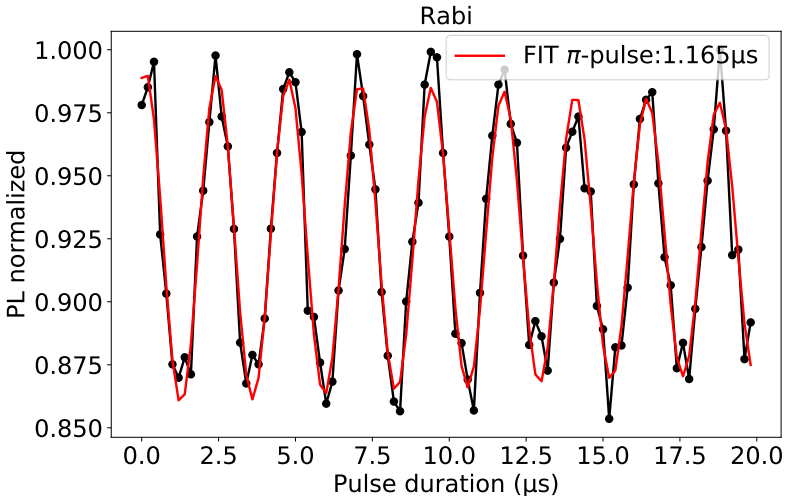


Figure 4.13: **Rabi measurement**. The PL oscillates as a function of the pulse duration, showing Rabi oscillations at a frequency $\Omega_R/2\pi = 450\,\text{kHz}$

The results shows $T_2^*$ $(d02)$= $1.2 \pm 1\mu s$ while $T_2^*$ $(d03)$ is up to = $52 \pm 5\mu s$. We have investigated others 16 NV center on sample *d02* been able to determine the coherence time of 7 NV centers. All of them presented $T_2^* < 3\mu s$.

In sample *d03*, on the other hand, among 10 NVs characterized, we have determine the $T_2^*$ of 6 NVs: three had $T_2^* < 5\mu s$ and the other three presented $T_2^*(a) = 24\pm3\mu s$, Fig. 4.14a, $T_2^*(b) = 30\pm3\mu s$, Fig. 4.14b and $T_2^*(c) = 52\pm5\mu s$, Fig. 4.14c. Therefore, these last 3 NV centers of *d03* sample are the best candidates for the low-temperature measurements.

## 4.9 Annealing and PL stability

Here we briefly comment on the NV fragility with respect to the Annealing. As has been described above, the sample *d02a* has been annealed at $1100°C$ in vacuum followed by an cleaning with the 3 acid bath. Nonetheless, an unexpected PL instability was observed.

The implanted NV centers of this chip were "revived", i.e., the Pl stability recovered, just after the second annealing, now at $460°C$ in an Oxygen atmosphere followed by Piranha acid cleaning. We believe that the second annealing was responsible to stabilize the NV charge state that was compromised during the first annealing because of it proximity to the surface [94].

## 4.10 Small ensembles of NV center

Fig. 4.16a shows the confocal microscope color map of a single set of lines. Its PL is around 10 times larger than the single NV PL, thus, we estimate that this line set has around 10 NV centers.

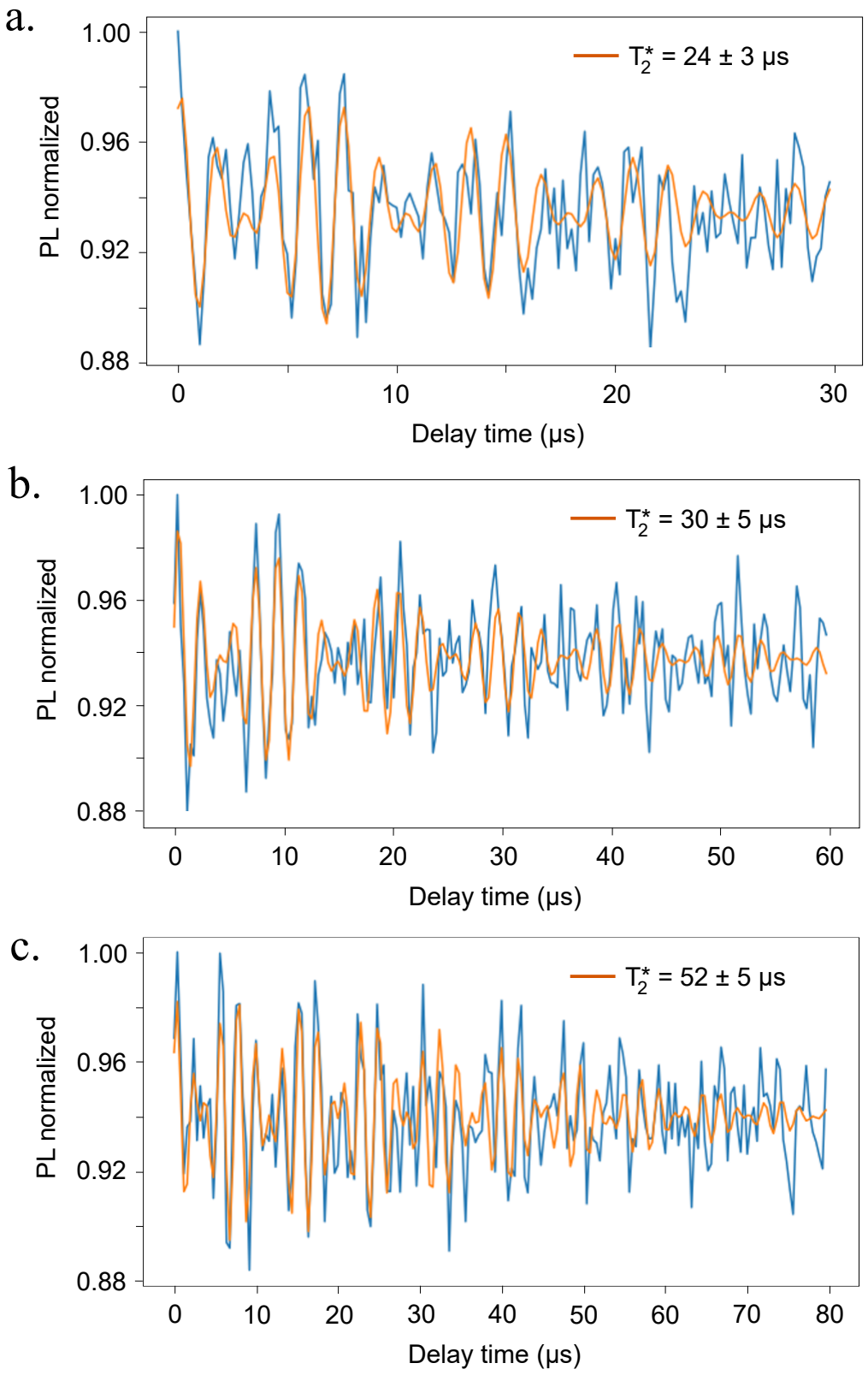


Figure 4.14: **Ramsey oscillations** measured for a sample enriched in $^{12}$C, showing **a.** $T_2^* = 24\mu$s **b.** $T_2^* = 30\mu$s **c.** $T_2^* = 52\mu$s.

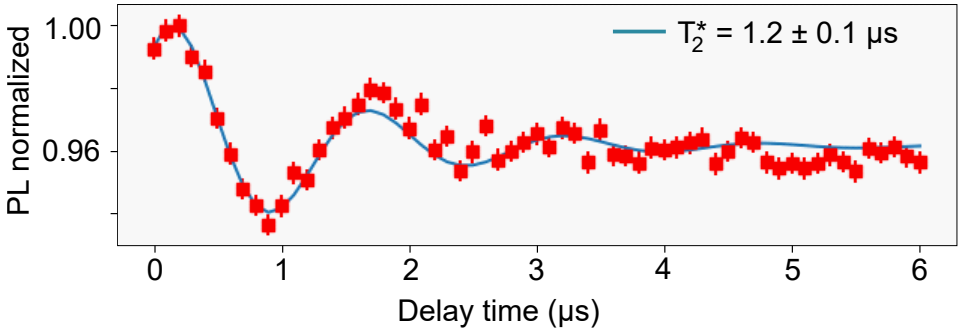


Figure 4.15: **Ramsey oscillations** measured for a sample with natural-abundance carbon, showing $T_2^* = 1.2\mu$s.

In the absence of applied magnetic field, a typical spectroscopy measurements of small NV ensembles (NV lines) is shown on Fig. 4.16b (orange). Note that the formed NVs have no preferential orientation given the diamond surface oriented perpendicular to $\langle 100 \rangle$ crystallographic plan. Plus, the earth magnetic field is large enough to shift the transition energies of few MHz. As a consequence, the curve of spectroscopy is broader and has a contrast of $\sim$ 12%. Applying, however, an external magnetic field as Fig. 4.8a, one can clearly distinguish the NV orientation one from another as shown in Fig. 4.16b (blue): there are several absorption lines, they are narrow and have $\sim$ 2% of contrast.

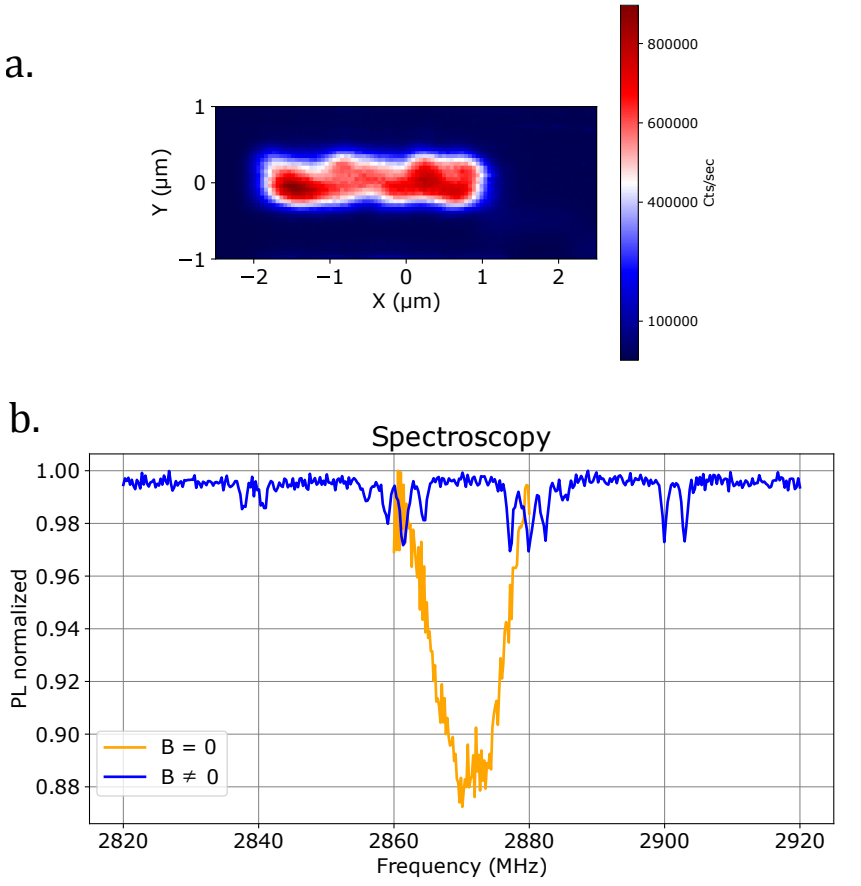


Figure 4.16: **Small NV ensembles**. Echo measurement of NV centers implanted in different diamond samples.

## 4.11 Substrate microwave losses

We finish this chapter discussing, briefly, about another characterization not performed in the confocal microscope. Among the different physical phenomena leading to resonator internal losses, the diamond chip mainly contribution involves dielectric losses. Thus, in order to roughly estimate this losses, we have measured the transmission signal $S_{12}$ of a Niobium box cavity with the diamond sample. Fig. 4.17 shows what we have obtained to sample d03 before and after cleaning it with 3 acid bath. We see that thorough cleaning enables to fully suppress the microwave losses caused by graphitization of the diamond surface.

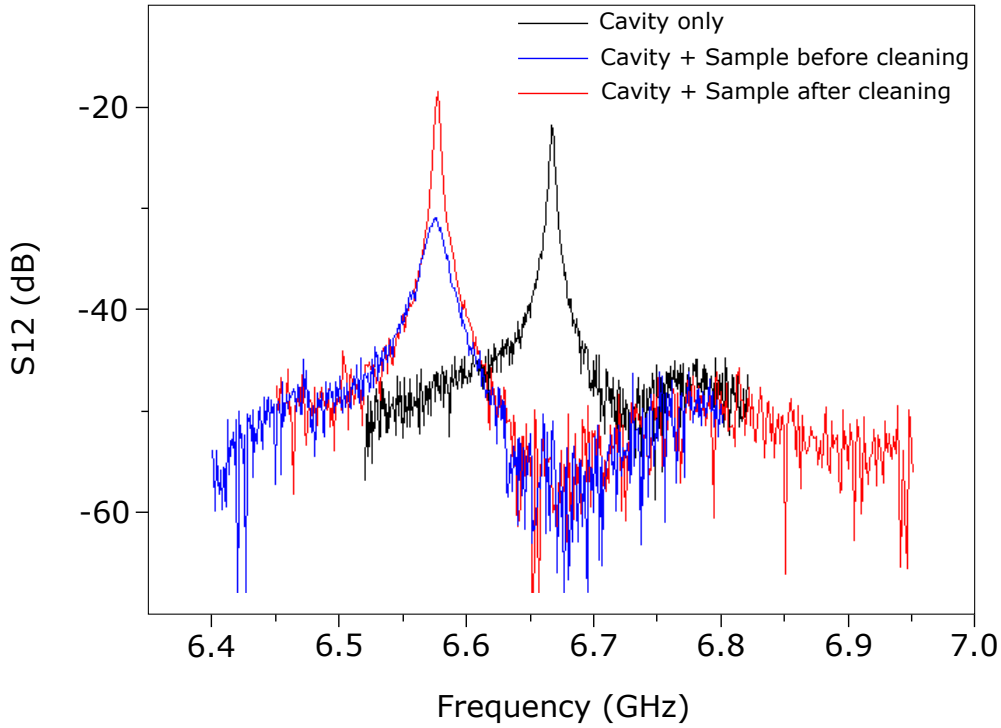


Figure 4.17: **Small NV ensembles**. (a) Photoluminescence of a small ensemble of NVs implanted along a line. (b) Spectroscopy of the NV ensemble, both in zero applied field and in a small applied field that resolves transitions from all NV orientations.

# Chapter 5

# Measuring the position of a spin relative to a nanowire

As explained in the previous chapters, for our purpose, the nanowire resonator should be positioned as precisely as possible above an individual NV center, with a typical precision of 10 nm. However, before turning to low-temperature measurements which take time and whose outcome is uncertain, we needed a rapid and efficient method to characterize the accuracy of our alignment method. This method is reported in this chapter, and has an interest on its own. Our method consists in passing a dc current through the nanowire at room-temperature, and using single-NV vector magnetometry to determine two components of the generated magnetic field at the NV position and deduce its relative position.

This chapter describes how we have selected the NV centers to be measured, followed by a description of the nanowire fabrication process and finally presents the measurements and analysed results.

## 5.1 Principle of the experiment

To explain the principle of the experiment, we consider a NV center interacting with the magnetic field $\mathbf{B}_0$ generated by passing a current I through a nanowire deposited on top of the diamond as illustrated in Fig. 5.1a. For now, we consider that the wire is infinitely long, so that $\mathbf{B}_0$ is located in the plane perpendicular to the wire. We will use two coordinate systems. The first, (x',y',z'), is defined with respect to the laboratory frame, Fig. 5.1a, with the nanowire being parallel to y' and $\mathbf{B}_0$ therefore located in the (x',z') plane. Because of invariance along the y' direction, we take y'= 0 at the NV location. The second, (x,y,z), is defined with respect to the NV center as explained in Ch.3 and shown in Fig. 5.1b. Note that $B_0 \cos\theta$ and $B_0 \sin\theta$ (shown in Fig. 5.1b) are defined with respect to the NV coordinates.

In the sample, the diamond edges are $\langle 110 \rangle$ and the surfaces are parallel to $\{100\}$ plane. Thus, in the lab's frame the NV orientations are given by:

$$NVA = \frac{1}{\sqrt{3}}\big(0, +\sqrt{2}, +1\big) \tag{5.1}$$

$$NVB = \frac{1}{\sqrt{3}}\big( +\sqrt{2}, 0, -1\big) \tag{5.2}$$

$$NVC = \frac{1}{\sqrt{3}}(-\sqrt{2}, 0, -1) \tag{5.3}$$

$$NVD = \frac{1}{\sqrt{3}}(0, -\sqrt{2}, +1) \tag{5.4}$$

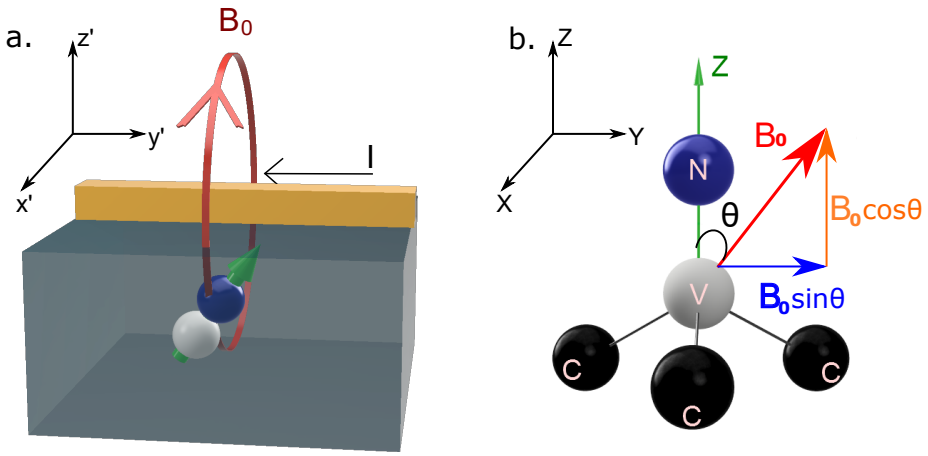


Figure 5.1: **Measurement sketch.a.** NV center in the diamond coupled with the induced magnetic field generated by the DC current through the nanowire at lab's referential frame. **b.** Induced magnetic field $\mathbf{B}_0$ and it parallel and perpendicular components with respect to the NV axis, in the NV's referential frame.

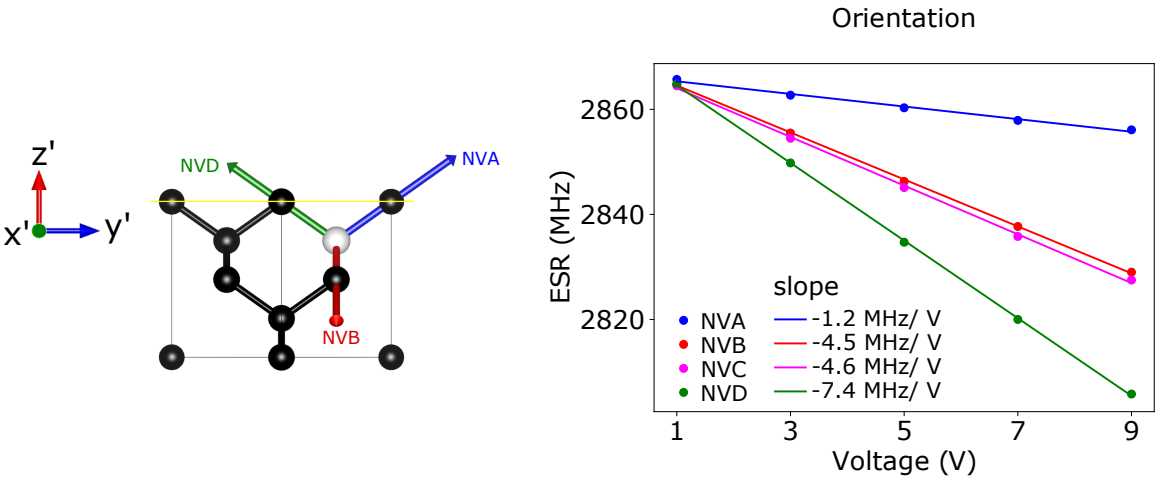


Figure 5.2: **NV center orientation**. **a.** Lateral view sketch of the diamond chip: edge $\langle 110 \rangle$ plane parallel to y' axis in lab's referential frame. Three of the NV orientations are emphasized. **b.** Electron spin resonance frequency as a function of the voltage applied in the coil that generates the magnetic field. The slope of the curves depends on the NV orientation.

Fig. 5.2a shows the NV families' sketch from lateral view of the diamond at the lab's referential frame. In the ideal alignment situation, the NV center would be located just below the nanowire (x'=0), so that also $\mathbf{B}_0$ would be horizontal and along the

x' axis. In this case, the field would be orthogonal to the NV axis for orientations A and D, which is therefore the desired configuration to maximize the NV-resonator coupling. Therefore, we decided to pre-select only NV centers with orientations A and D with respect to the nanowire.

For that, we had to determine each NV's orientation before nanowire fabrication. In order to do so a magnetic field $\mathbf{B}_0$ was generated by a rectangular coil placed behind the chip as described on Fig. 4.8c and Fig. 4.8d, in previous chapter. Performing spectroscopy as a function of $\mathbf{B}_0$ magnitude, we obtain the curves shown in Fig. 5.2b where the slope of each curve is proportional to the polar and azimuthal angles between the NV and $\mathbf{B}_0$ . Finally, using a Mathematica code we have identified the orientations from these curves. To perform the measurements, we have selected only NV D families.

## 5.2 Nanowire fabrication

The nanowire is fabricated using a liftoff process. A resist mask is patterned using electron-beam lithography, followed by metal deposition and liftoff. To ensure minimal alignment errors between the NV and the nanowire, we use the same 100keV electron-beam lithography system (Leika EBPG500+ at laboratory C2N in Marcoussis) to pattern both the implantation mask and the nanowire mask, with the same automatic alignment procedure using the eched marks on diamond.

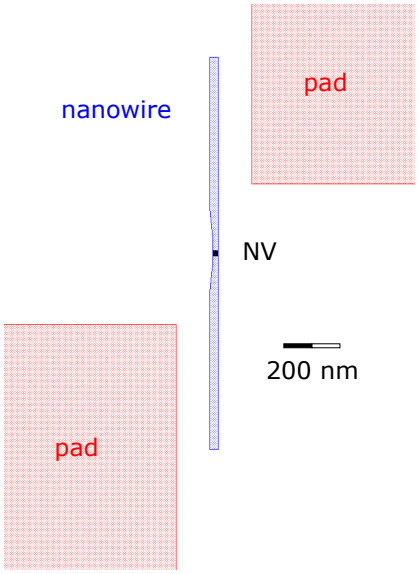


Figure 5.3: **Nanowire design.**

The design of the nanowire and the connector pads is shown in Fig. 5.3. Depositing the nanowire and pads in a single metal deposition step would imply that the film thickness would be uniform, which is not desirable. Indeed, the nanowire itself should be as thin as 15-20nm in order to maximize the coupling to the NV center. On the other hand, having such thin pads would be detrimental for a number of reasons. For the experiment itself, it would become hardly possible to bond the sample to the PCB. Moreover, having in mind the final experiment with the

resonator, a too thin resonator would suffer from large kinetic inductance, rendering its frequency more difficult to predict. We thus use a 3-angle evaporation process, which enables to modulate the thickness between the contact pads and the nanowire itself. Such a process is commonly used to fabricate Josephson junctions. In our case it relies on a suspended metallic mask, as shown in Fig. 5.3, fabricated as follows:

1. Lithography Mask: Sample Cleaning; $\sim$ 700 nm MMA; 20 nm Ge; $\sim$ 120 nm PMMA;

2. Lithography: PMMA patterned at a 100 KV electron beam lithography; Development;

3. Reactive ion etching (RIE) used to transfer the PMMA pattern to Germanium layer;

4. An oxygen plasma is used to create a MMA undercut which enables the suspension of Germanium mask as well as a proper cleaning of diamond surface where the Aluminum will be deposited.

The Al is then evaporated through this mask in 3 angles: 0°, producing the nanowire, and $\pm 25°$ to make the pads connection (as thick as 50 nm in the end of the fabrication). The result of this process is illustrated in Fig. 5.5 and Fig. 5.6, which show SEM images of the nanowire and pads. The nanowires are 500 nm long and $\sim$ 30-40nm wide and 20 nm thick.

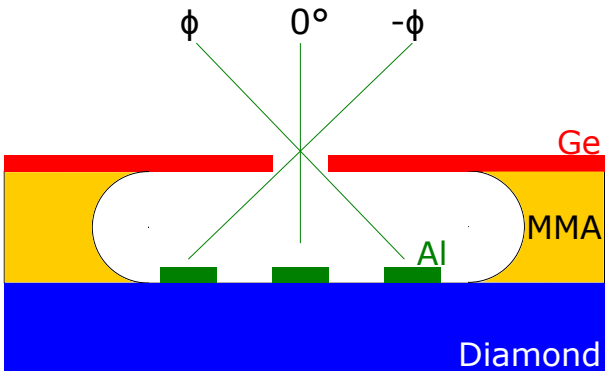


Figure 5.4: **Mask and Al evaporation**. The nanowire and pads were fabricate using the 3-angle evaporation process where the Al is evaporated through a suspended metallic mask.

We identified 7 NV centers and fabricated a nanowire on top of each of them. The fabrication result is shown in Fig. 5.5. One side of the nanowire is connected to a common ground electrode, and the other one to a separate dc pin on the PCB. In addition, a waveguide is patterned nearby to pass the microwave signals needed to drive the spins.

Fig. 5.6 shows a zoom SEM image of all the nanowires. As one can see, NW-g did not come out properly of the lithography process, for an unknown reason.

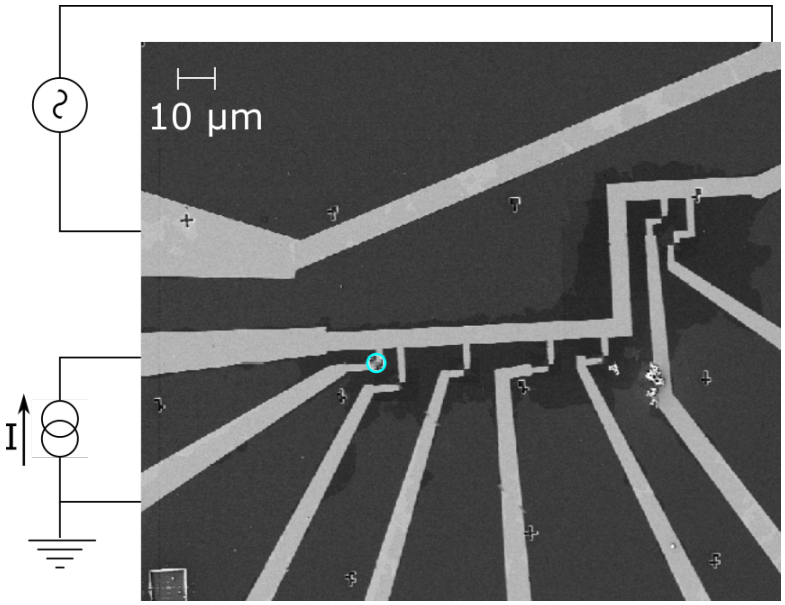


Figure 5.5: **Nanowire Fabrication**. SEM image of all Al pads fabricated as well as the patterned waveguide.

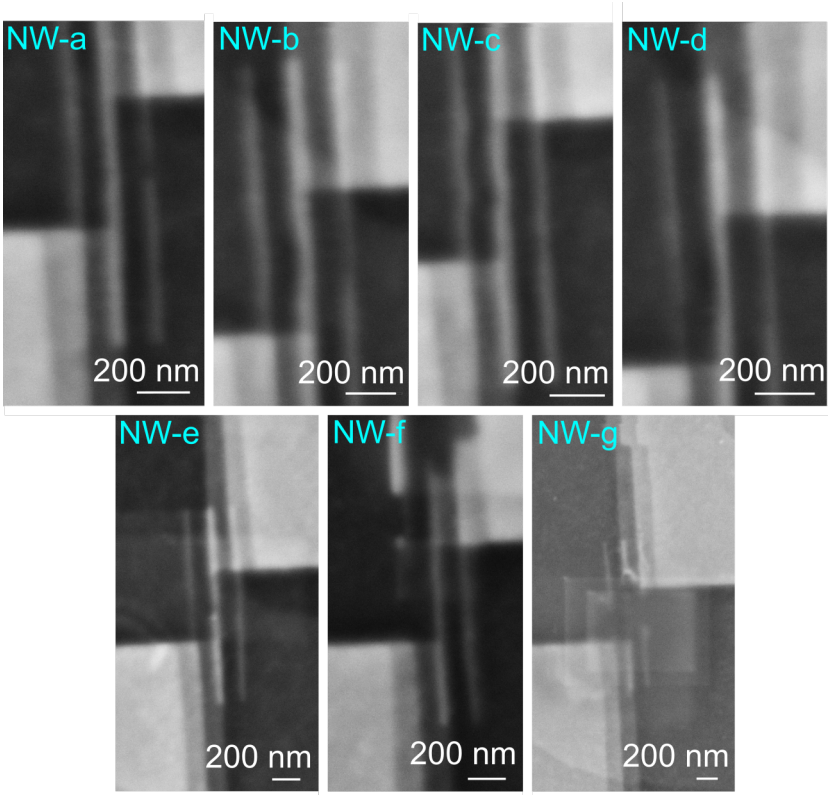


Figure 5.6: **Al nanowire and pads**. Zoom on each nanowire. Nanowire NW-g has exploded in some of the fabrication steps

## 5.3 Measurements at room temperature

### Photoluminescence

We now present the NV vector magnetometry measurements. The photoluminescence of the NV behind the nanowire can be collected despite the Aluminium on the surface because the nanowire length is larger than the spot size of the laser used in the confocal setup. As one can see on Fig. 5.7, some amount of PL is measured on top of the Al pads but a clear bright spot is observed in the center of the nanowire at expected NV location.

The sample is mounted on its PCB holder, as explained in chapter 4 and is wire-bonded to feed a DC current I. One of the nanowires showed up to be shorted and thus, we have continue the experiments with 5 nanowires.

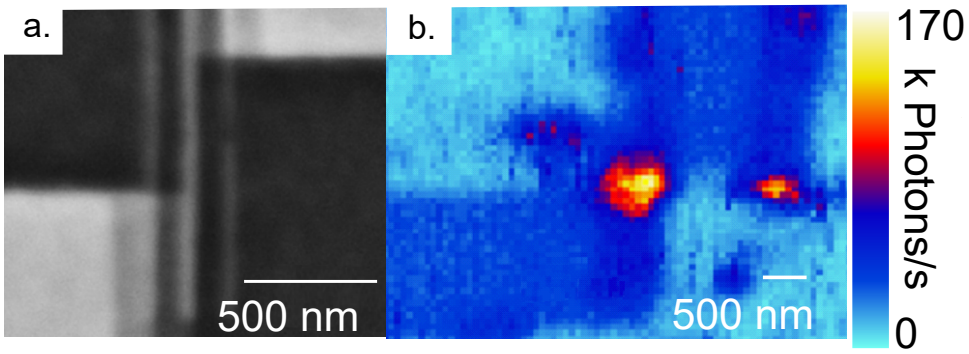


Figure 5.7: **Photoluminescence**. **a.** SEM image of one nanowire and its pads. **b.** Confocal microscope image of this nanowire. The color map corresponds to the number of photons collected per second. Even though the AL pads emits slightly more PL than the diamond surface we can distinguish the NV center brighter spot in the middle of the pads.

### Spectroscopy

The parallel component of the field,n$B_0 \cos\theta$ , was determined with the spectroscopy sequence shown in Fig. 5.10a. Because the applied fields stay lower than 2mT, we will use the approximation that $\Delta\nu = 2\gamma_e \ B_0 \cos\theta$ , as explained in Chapter 3.

It is remarkable, however, that due to the presence of the Al pad the NV photoluminescence can be drastically reduced making impossible the conclusion of the measurements for some NV centers. Fig. 5.9 and Fig. 5.8 show the contrast reduction of NV2 and NV0 respectively. In the first one the contrast reduces from $\sim 15-20\%$ to $\sim 7.5\%$ and the ESR x I could be done without problems. The contrast of NV0, however, had reduced from $\sim 3-4\%$ to $\sim 0.25-0.5\%$ and we could not perform the vector magnetometry. In Another NV center, NV4, no spectroscopy was observed at all after Al nanowire deposition. Therefore, we have continue the measurements with 3 NV center: NV1, NV2 and NV3. Fig. 5.10 correspond to the data of NV1 only. The reader can found the analogous measurement data for NV2

and NV3 in the Appendix A.

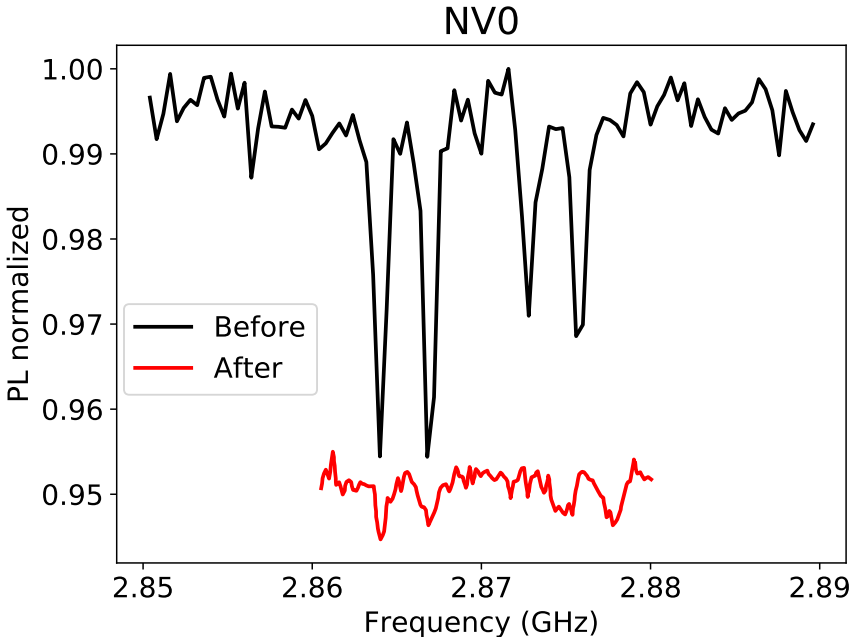


Figure 5.8: **Spectroscopy of NV0.** Black [red] curve is the spectroscopy before [after] the Aluminium evaporation. One can see that the contrast reduces from $\sim 3-4\%$ (before) to $\sim 0.25-0.5\%$

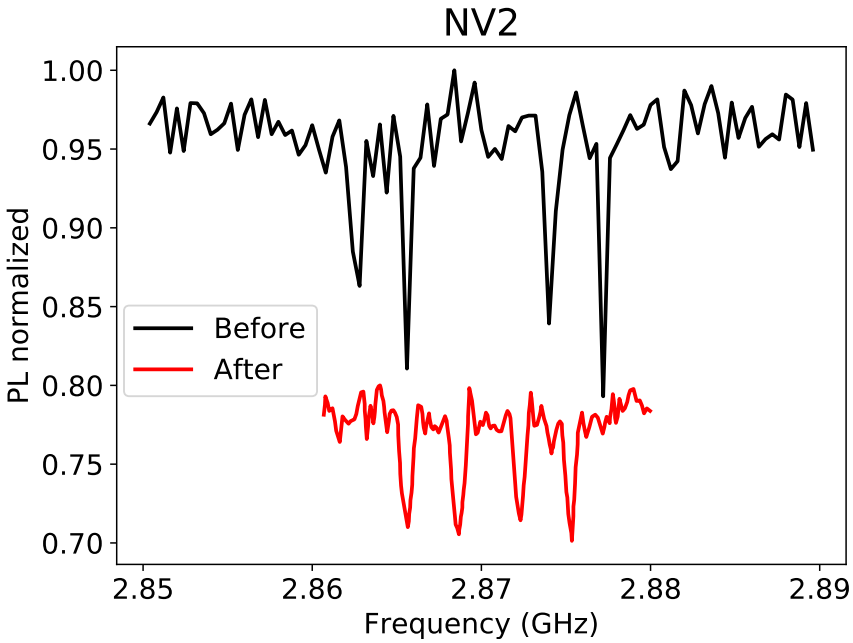


Figure 5.9: **Spectroscopy of NV2.** Black [red] curve is the spectroscopy before [after] the Aluminium evaporation. One can see that the contrast reduces from $\sim 15-20\%$ (before) to $\sim 7.5\%$

The NV spectrum is then measured for several values of I, as shown in Fig. 5.10b.

The frequency of each ESR line is fitted by a sum of Lorentzian, yielding $B_0 \cos\theta$(I). As expected, $B_0 \cos\theta$ is seen to depend linearly on I, $B_0 \cos\theta$ = A I + $B_0 \cos\theta(0)$. The fit yields $A = 14 \pm 0.1 G/mA$, and $B_0 \cos\theta(0)$= 1.2 G is due to the Earth magnetic field.

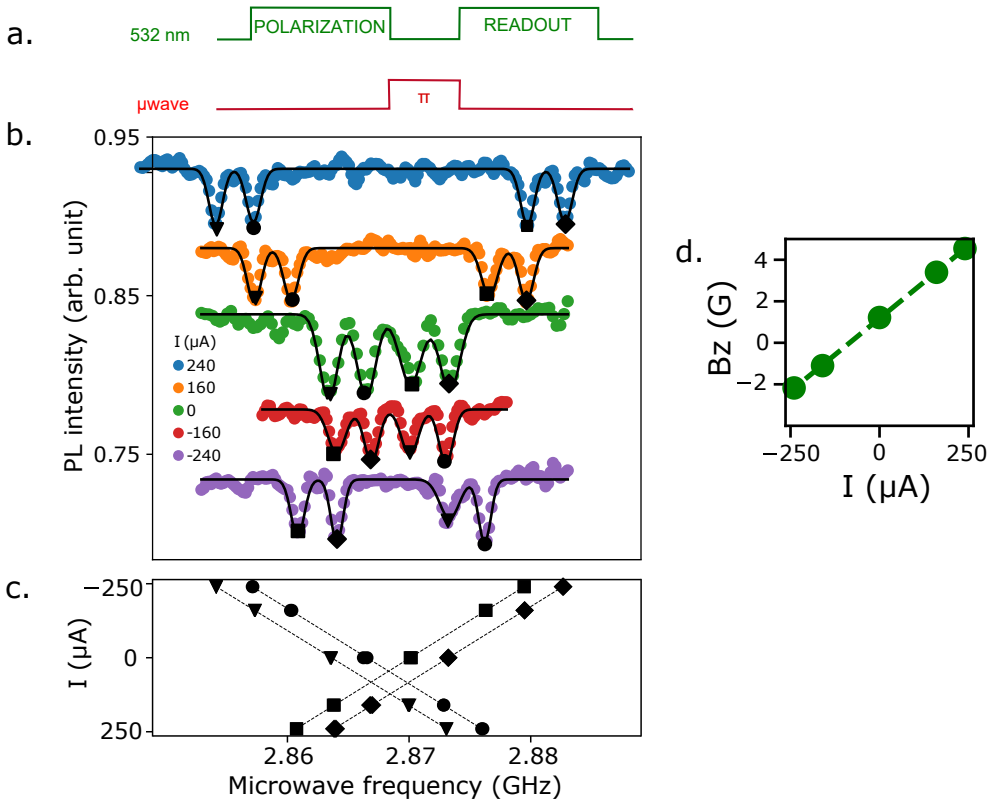


Figure 5.10: $B_0 \cos\theta$ **determination**. **a.** Spectroscopy microwave pulse sequence. **b.** Spectroscopy measured at various DC current applied. **c.** Fit of ESR frequencies versus applied current. **d.** $B_0 \cos\theta$ as a function of the applied DC current

### Nuclear Oscillations

The perpendicular component of $\mathbf{B}_0$ was then determined using the nuclear oscillation pulse sequence, as explained in Chapter 3. Fig. 5.11b shows the oscillations obtained under several currents I. Due to the long $^{15}N$ nuclear spin coherence time in $m_s = 0$, these oscillations can be observed over a range of 100 $\mu s$ without a measurable decay. Each curve were fitted with a sine function to determine their frequency and $B_0 \sin\theta$ was calculated by equation 3.12:

$$\hbar\omega_{NO} = \sqrt{\gamma_n^2 B_0 \cos\theta^2 + \gamma_{n\perp}^2 B_0 \sin\theta^2} \tag{5.5}$$

As for the parallel component, a linear fit of $B_0 \sin\theta$(I) yields the Earth magnetic field $B_0 \sin\theta(0)$ = -1.3 G, as well as the slope (19.1 ±0.3)T/A.

The values of d/dI($B_0 \cos\theta$) and d/dI($B_0 \sin\theta$) measured for all 3 NV centers are summarized in Table 5.1

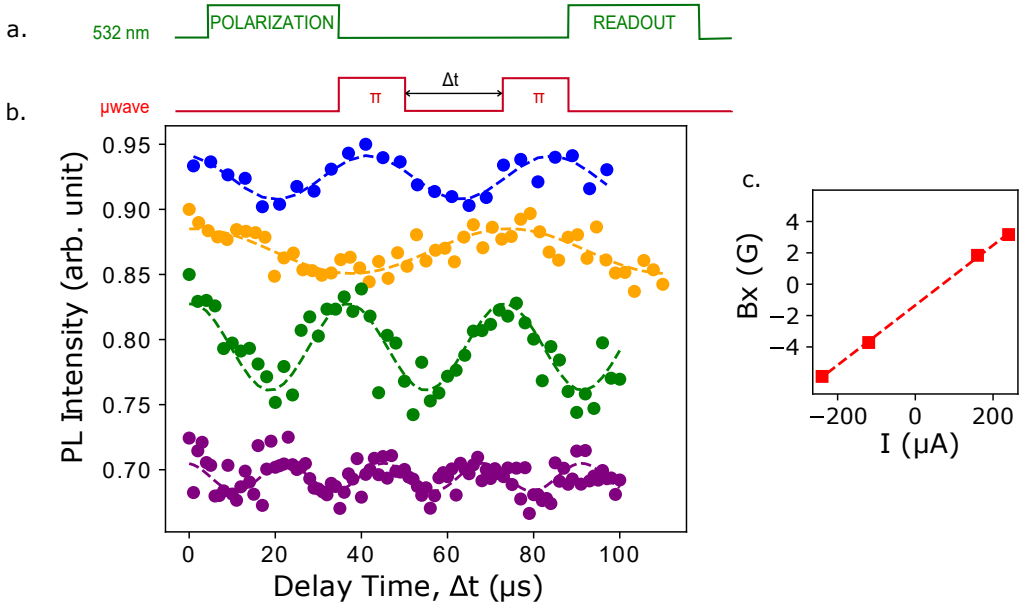


Figure 5.11: **$\mathbf{B}_0\sin\theta$ determination**. **a.** Microwave pulse sequence. **b.** Nuclear Oscillation measured at various DC current applied.**c.** $B_0 \sin\theta$ as a function of the applied DC current

| | $B_0 \cos\theta$ (T/A) | $B_0 \sin\theta$ (T/A) |
|---|---|---|
| NV1 | $1.40 \pm 0.1$ | $1.89 \pm 0.3$ |
| NV2 | $0.85 \pm 0.01$ | $1.30 \pm 0.3$ |
| NV3 | $0.76 \pm 0.1$ | $1.06 \pm -$ |

Table 5.1: Values of dB/dI components

## 5.4 Analysis

### Infinitely-long wire

Using the knowledge of d/dI($B_0 \cos\theta$) and d/dI($B_0 \sin\theta$), we can determine the position of the NV relative to the nanowire. To do so, we compare the measured $\mathbf{B}_0$ with the computed field distribution generated by a given current I.

The nanowire carrying a current $I$ is modelled in Python as infinitely long, with a constant rectangular cross-section of thickness $t$ and width $w$, a geometry for which analytical solutions are available (showed in Appendix A). In this model, the field generated by $I$ has no component along $y'$, the wire direction, and its two components along $x'$ and $z'$ are thus fully constrained by the measured $B_z$ and $B_\perp$. Since we know the orientation of the NV axis, we can uniquely determine the position $(x', z')$ which most closely matches the measured magnetic fields ($B_0 \cos\theta$, $B_0 \sin\theta$).

The precision (error bar) of this positioning is determined using a bootstrapping method: we perform the fitting procedure 5000 times using a wire width $w$ of $36 \pm 5nm$ and a thickness of $20 \pm 2nm$. For the distribution of measured field values we take $\sigma = 0.2\text{G/mA}$, resulting in the position probability density function (pdf) shown in Fig. 5.12a. There, it is represented a 2d graphic of depth (z') versus width (x'), the red line corresponds to the diamond surface, the black rectangle centered in (0,0) is the nanowire cross section, the magnitude of $\mathbf{B}_0$ field is shown in the color scale and finally, the contour distinguish with different colors the position pdf. The positions calculated by this method as well their incertitude are shown in table 6.1 and labeled as $x_1'$ and $z_1'$.

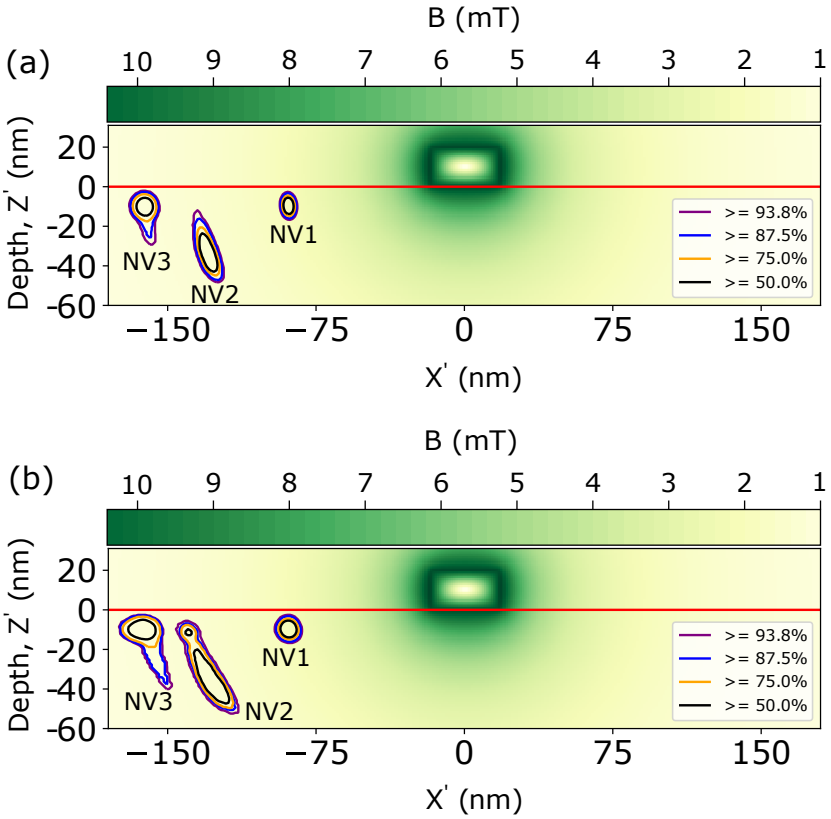


Figure 5.12: **Estimating single NV centers' positions.** The color map represents the magnitude of the magnetic field $\mathbf{B}_0$ due to a DC current passing through the nanowire. The continuous red line at depth = 0 nm corresponds to the diamond surface. The contour at different color lines are the probability density map of the NV's position.**a.** Analytical result; **b.** Finite element simulation correction.

We first note that the three NVs are not located below the nanowire, but at respectively 84, 123, and 152 nm from the nanowire. This indicates that our alignment procedure is not sufficiently accurate. The fact that all 3 NVs are on the same side of the wire seems to suggest that there was a systematic shift of $\sim$ -100nm, possibly due to the uncertainty in the successive alignment steps of the lithography.

We also note that the depth determined for NV1 and NV3 is in qualitative agreement with the $11 \pm 5nm$ depth expected from SRIM simulations given the implantation energy of 7.5 keV, while the larger depth of NV2 may be due to channeling. The standard deviation in lateral positioning of 27 nm can be semi-quantitatively un-

derstood as arising from the finite size of the implantation aperture (with $\sim$ 20 nm diameter) and the straggle upon implantation (also $\sim$ 20 nm diameter). Moreover, considering a position pdf $\geq 75\%$ (orange and black contour), this single-NV vector magnetometry leads to a precision of $\sim 10nm$. [95]

### Finite-length wire

In order to assess the validity of the infinitely-long wire hypothesis, we compute the three-dimensional magnetic field profile using Comsol finite element simulation, using the real pad and wire configuration. The results are shown in Fig. A.2.

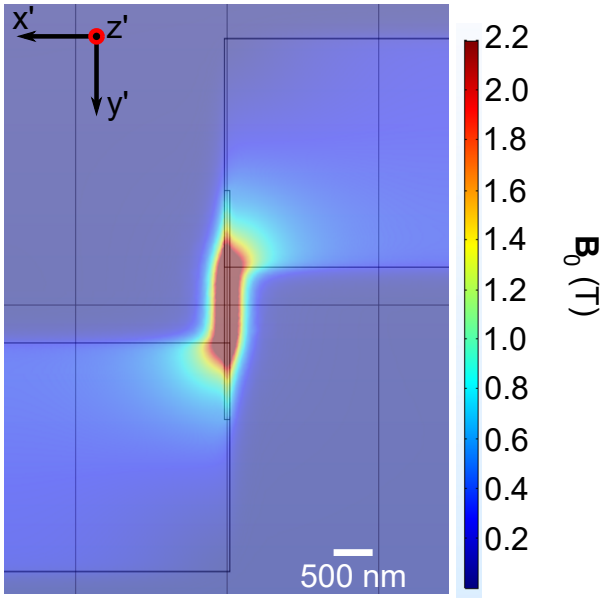


Figure 5.13: **Finite element simulation of $\mathbf{B}_0$ .** The color map represents the $\mathbf{B}_0$ magnitude due to a current of 1A passing through a 500nm long nanowire connected with pads.

The field profile is no longer invariant by translation along y', but instead slightly

| | $x'_1$ (nm) | $z'_1$ (nm) | $x'_2$ (nm) | $z'_2$ (nm) |
|---|---|---|---|---|
| NV1 | $-84 \pm 1$ | $-9 \pm 3$ | $-84 \pm 2$ | $-9 \pm 3$ |
| NV2 | $-123 \pm 3$ | $-30 \pm 8$ | $-122 \pm 7$ | $-29 \pm 11$ |
| NV3 | $-152 \pm 3$ | $-11 \pm 6$ | $-152 \pm 6$ | $-13 \pm 9$ |

Table 5.2: Position of the NV centers relative to the nanowire, assuming an infinitely-long nanowire (left, $[x'_1, z'_1]$) or taking into account finite-length corrections as explained in the text (right, $[x'_2, z'_2]$).

depends on the y' component. This dependence introduces an extra uncertainty in the positioning of the NV centers. We take it into account by computing the relative variation of the magnetic field when y' is varied, at the location fitted by the previous method. Because the alignment precision seems to be of order $\sim$ 100nm, we consider that y' can vary between -150nm and +150nm. We find that on this range, the values of $B_{x'}$ and $B_{y'}$ change by 0.9 and 3.7%. We then repeat the bootstrapping

calculation, taking into account this extra uncertainty in $B_{x'}$ and $B_{z'}$. The result is shown in Fig.1.12b. Even though the uncertainty is indeed larger, the conclusions above are not dramatically modified (table 6.1). We do obtain an rms accuracy of the positioning of $\sim$ 10nm.

## 5.5 Final comments

The vector magnetometry has an interest on itself because the determination of $B_0 \sin\theta$ from room-temperature measurements allowed us to estimate the coupling constant $g$ of a NV to a nanowire resonator, as proposed in [12], for its detection using microwave measurements. From equation 2.8, g is:

$$g = -\gamma_e \langle 0|\mathbf{S}|1\rangle \cdot \delta\mathbf{B_1} = \gamma_e \delta B_{1,\perp} \langle m_S = 0|S_x|m_S = -1\rangle = \frac{\gamma_e \delta B_{1,\perp}}{\sqrt{2}} \tag{5.6}$$

because $\langle m_S = 0|S_x|m_S = -1\rangle = 1/\sqrt{2}$ for a spin 1. Considering for instance the resonator design envisioned in [12], for which quantum fluctuations of the current were estimated as $\delta i = 35\,\mathrm{nA}$, the resulting $\delta B_{1,\perp} = dB_{0\perp}/dI \cdot \delta i$ is directly obtained for each of the 3 NV measured, yielding to a coupling constant of $g/2\pi = 0.6$, 0.7, and 1 kHz.

In this way, we can estimate the measurement time of equation 2.20

$$T_{meas} = \frac{\kappa^2 \Gamma_2^*}{\eta g^4}. \tag{5.7}$$

with $\kappa$ the resonator linewidth, $\gamma_2$ the NV coherence time, and $\eta$ the microwave detection efficiency.

Taking $\eta = 1$, $\kappa = 10^5\, s^{-1}$, $\gamma_2 = 10^5\, s^{-1}$, we get a measurement time between 0.6 and 5 s for unit signal-to-noise ratio, which motivates the need for a better alignment in order to bring the a closer distance between implanted NVs and the nanowire and/or increase $\delta i$. In the future, the method should allow to improve the accuracy of the alignment process, by repeated trial and error. In the following of this project, we have however opted for an "easier" solution. Instead of targeting a single NV center, our idea is to couple it to a small ensemble of NVs (lines), aligned with the nanowire, such that statistically there should be one or a few NVs located closer to the wire. This solution has for extra advantage of alleviating the risk of finding an NV center in the wrong charge state. In the following, we thus explain how we fabricate a resonator on top of lines of implanted NVs, as present in our implantation mask.

# Chapter 6

# The resonator

In this chapter we show the design, fabrication and microwave characterization of the proposed resonator towards single spin detection.

## 6.1 Introduction

As described in Chapter 2, the enhancement of the spin-photon coupling requires to maximize the magnetic field fluctuations at the spin location $\delta B_1$ which in the limit of an infinitely thin and long, can be expressed by Ampère's law: $\delta B_1 = \mu_0 \delta i/(2\pi r)$. Thus, there are two approaches towards coupling enhancement, they are : 1) to reduce the relative distance NV-Nanowire, as described in the previous chapters, and 2) to adapt the resonator geometry getting a shorter inductive wire which increases the $\delta i$ given by eq.2.21

$$\delta i = \omega_0 \sqrt{\frac{\hbar}{2Z_0}}, \tag{6.1}$$

where $Z_0$ is the resonator inductance. To minimize $Z_0$ we opted by a lumped-element geometry where one can pattern small inductors in parallel with long interdigitated capacitors.

The Purcell rate eq. 2.12

$$\Gamma_P = 4g^2/\kappa. \tag{6.2}$$

must also be maximized, as described in chapter 2. This implies minimizing the loss rate $\kappa$. Two types of losses should be distinguished: losses due to the coupling of the resonator to the output line $\kappa_c = \omega_0/Q_c$, and losses due to internal losses of the resonator $\kappa_i = \omega_0/Q_i$, where we have introduced the coupling and internal quality factors, respectively $Q_c$ and $Q_i$. Ideally, one should operate in the over-coupled regime where $Q_i \gg Q_c$, because then all signal photons leak out of the resonator to be detected. In superconducting resonators, the internal losses are due to dielectric losses, quasi-particles, and vortex motion,[96, 97, 98, 99, 100] which should thus be minimized for our experiment.

We have cleaned properly the diamond sample to avoid dielectric losses, as describes in chapter 4. Moreover, since the radiation can be suppressed by confining the sample in a leak-tight metallic box, we chose to enclose the sample in a a high-conductivity copper box whose modes have frequencies above the resonator one. Fig.

6.2a shows a photograph of our box. The diamond sample is installed in the box by gluing it on top of a sapphire chip, as seen in Fig. 6.2b. The planar resonator is capacitively coupled to antennas which in turn is coupled to the measurement lines. The measurements are done in reflection. The frequency modes of the box and the resonator were carefully simulated to optimize the planar resonator design.

## 6.2 Design and electromagnetic simulations

Geometry and box coupling are designed using HFSS, a simulation tool that allows us to reproduce the geometry of the cooper box, the antennas, the diamond sample (relative permittivity = 5.7) as well as the the superconducting resonator. The capacitive part of the resonator, i.e, the large pads and the interdigitated fingers, is made of 100-nm-thick aluminium and and has lateral dimensions larger than 1 $\mu m$. Its kinetic inductance ($L_k$) is negligible [101]. The presence of the nanowire however, implies in a $L_k$ that depends on the nanowire dimensions w,t, and l, [102]. For our particular case with: w = 40 $nm$, t = 25 $nm$ and l = 2 $\mu m$ $L_k$ is 42pH. As the simulations shows below, that is 7.5% of the geometric inductance $L_g$. Thus, this value was added manually into the simulations. The direct consequence of $L_k$ is a shift in the resonator frequency.

The LC resonator simulated geometry is shown in Fig. 6.1. It is composed by an interdigitated capacitance of 104 10-$\mu m$-wide finger spaced by 10 $\mu m$ in parallel with 10 $\mu m$ inductive wire of 100 $\mu m$ length. This short inductance design is based on [8] paper with width and spacing of the fingers adapted to a target resonance frequency as close as possible to the NV center transition energy, i.e., ∼3 GHz.

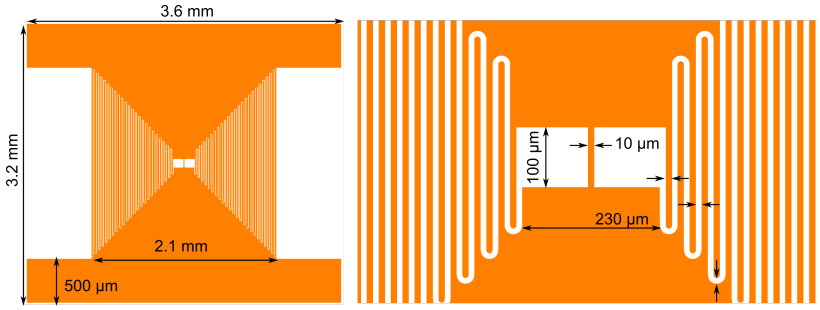


Figure 6.1: **Resonator Layout. left** the full resonator; **right** Zoom in the center at the inductive wire.

Fig. 6.2c shows the HFSS simulation of the first TE box mode whose frequency is 3.34 GHz. Fig. 6.2d shows the resonator surface current distribution, which is indeed localized at the short wire location, as expected from the mode that we wish to use for the spin detection. From these simulations we have extracted resonator capacitance (C), geometric inductance ($L_g$) and then, calculated its resonance frequency ($\omega_0/2\pi$), its impedance ($Z_0$) and $\delta i$. The coupling quality factor ($Q_c$) between the resonator and the box (respectively the box to the measurement lines) can also be estimated. Table 6.1 summarize all this values. As explained in Chapter 1, these values are compatible with a sub-millisecond measurement time for a single spin detection, assuming the alignment is as good as considered there.

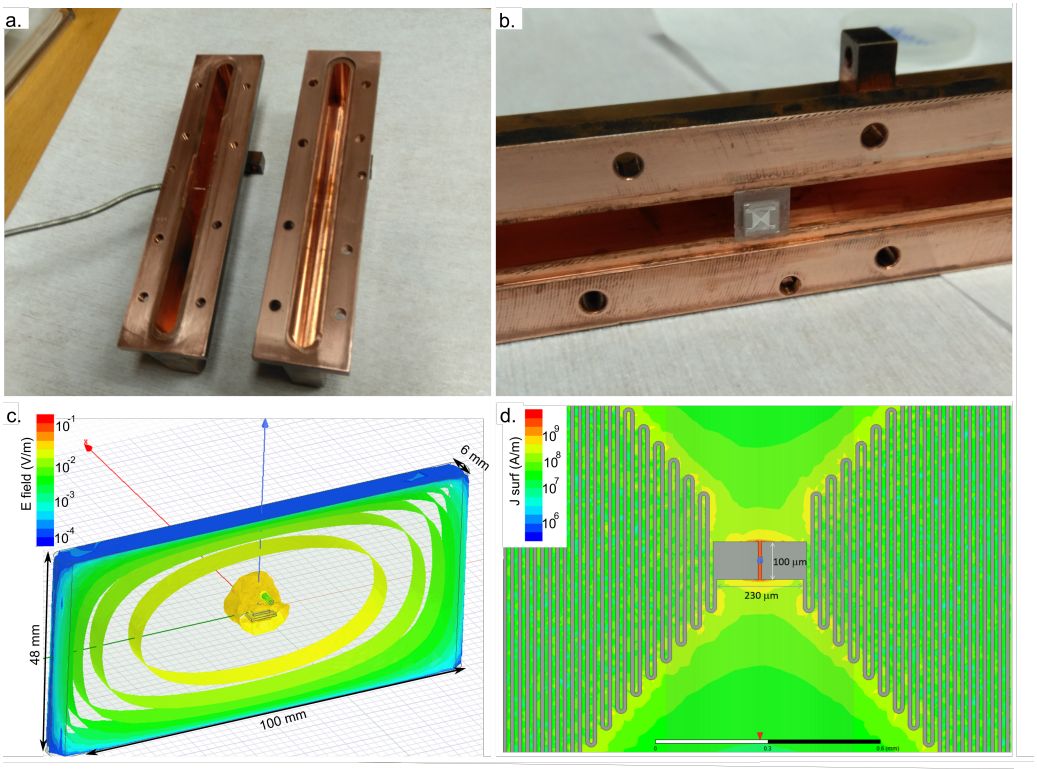


Figure 6.2: **Microwave HFSS simulations a.** Copper box with its antenna; **b.** diamond sample placed on sapphire chip inside the box; **c.** HFSS simulated TE first mode of the box; **d.** Surface current distribution ($J_{surf}$) along the resonator.

| | Resonator | Box |
|---|---|---|
| $\omega_0/2\pi$ | 3.02 GHz | 3.34 GHz |
| $L_g$ | 560pH | - |
| $L_k$ | 42pH | - |
| $C$ | 5pF | - |
| $Z_0$ | 10.6 Ω | - |
| $Z_t = \sqrt{(L_g + L_k)/C}$ | 11 Ω | - |
| $Q_{coupling}$ | $1 \cdot 10^5$ | 955 |

Table 6.1: Resonator simulation parameters

## 6.3 Resonator fabrication

As discussed in the previous chapter, the resonator is desired to have a thin inductive nanowire and thick capacitive fingers and pads. In Chapter 5, we have used a three-angle evaporation process to achieve this. However, when applying this process to the resonator fabrication, we have encountered significant difficulties, in particular due to the very large area that needs to be exposed with electron-beam to pattern the resonator capacitor, leading to charging effects and explosions of the Germanium layer.

We have thus developed another process, inspired by the way modern superconducting qubits are fabricated [103]. In this process, the capacitor is patterned in a first step, by wet etching of an aluminum layer that can thus be deposited on a

very clean substrate. Then, the nanowire is deposited in a second step, by a short e-beam exposure. Finally, contacting of the nanowire and the capacitor is achieved in a third step, in which a window is opened and the aluminum oxide is etched by argon ion milling (the "bandage" step). This process has several advantages. It avoids the problems of substrate charging and germanium explosion. It enables proper cleaning of the substrate. It also makes the alignment more precise, as the e-beam step is very short. More information about the fabrication can be found at:[104] and in Appendix A.

Fig. 6.3 show the optical microscope image of the resonator center, in the left, and a SEM image, in the right, of the nanowire. The nanowire width could vary between 30-40 nm. We remark that due to the fragility of the NV charge state we avoid to perform SEM image of the nanowire fabricated on diamond samples with implanted NVs.

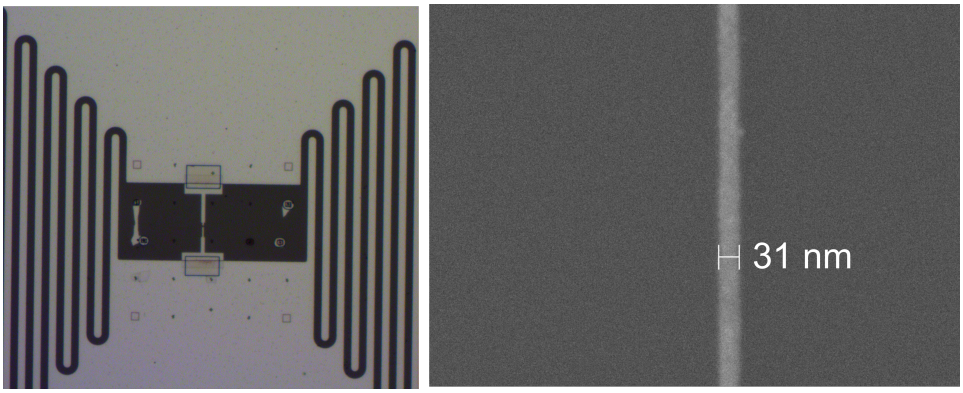


Figure 6.3: **Fabricated resonator**: *left* Optical microscope image, *right* SEM image of the nanowire.

## 6.4 Low temperature characterization

### Sample mounting and microwave setup

The experiment is performed at 10 mK stage of Bluefors cryostat, as seen in Fig. 6.4b. A sketch of the measurement setup is shown in Fig. 6.4a. The sample is measured in reflection. The input signal is attenuated at each stage of the fridge, i.e., at 10mK, 4K and 70K; and we ends up with a final attenuation of 70 dB. We use a low-pass filter with infra-red absorptive material to minimize the quasi-particles responsible to resonator losses. The signal reaches the sample via a double circulator, used to prevent undesired reflections. The total losses of the resonator are obtained by fitting the resonator total quality factor $\kappa = \omega_0/Q_{total}$. Finally, we used a commercial HEMT to amplify the signal at 4K and an usual amplifier at room temperature.

The box with the diamond sample on the sapphire chip, Fig. 6.2b, is closed and placed inside the couple of orthogonal Helmholtz coil. The sample is mounted such that both coils can only apply a magnetic field parallel to the diamond surface. Before cooling down the cryostat, we also install magnetic shielding to prevent vortices.

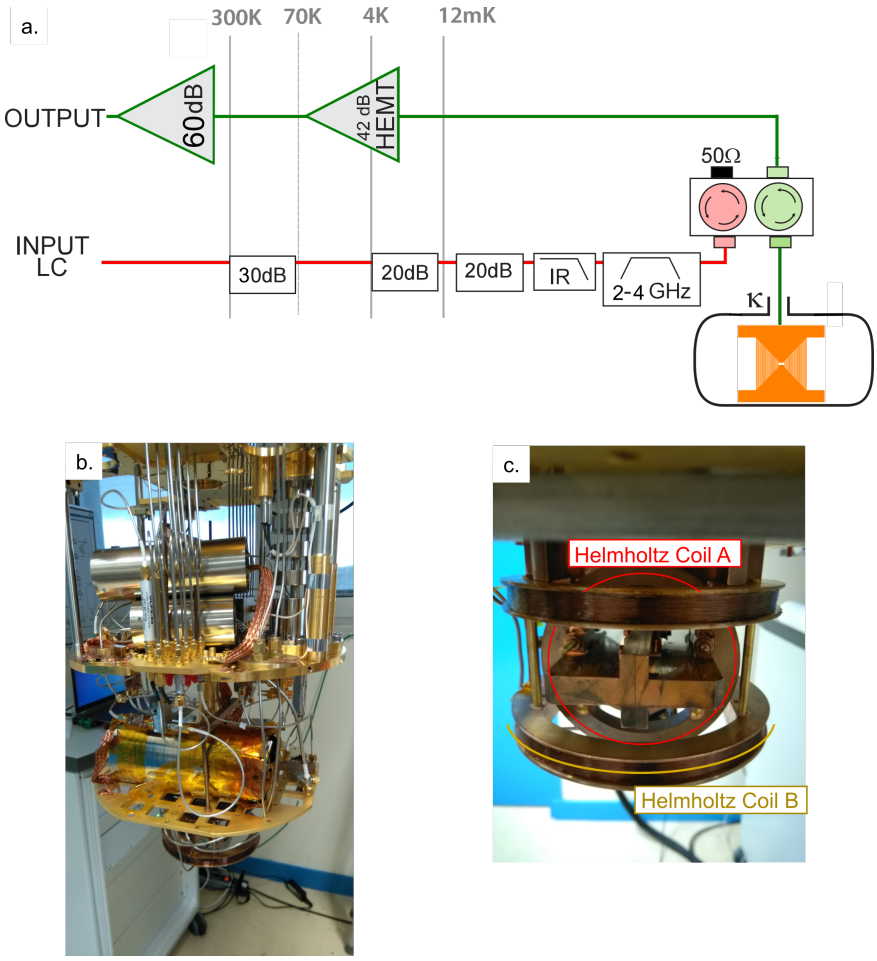


Figure 6.4: **Low Temperature setup.** **a** Microwave cryogenic setup connecting the room-temperature apparatus to the 12 mK experimental stage. **b.** Bluefors dilution fridge photo. **c.** Copper box inside the Helmholtz coil.

### Microwave characterization

Aiming at validate each fabrication step, 3 resonators were fabricated:

| | Sample | Nanowire | NV | $\omega_0/2\pi$(GHz) | $Q_i$ |
|---|---|---|---|---|---|
| Reso1 | *2sideimpl* | *no* | *yes* | 2.8 | $1 \cdot 10^6$ |
| Reso2 | *Diam2* | *yes* | *no* | 2.856 | $1.4 \cdot 10^5$ |
| Reso3 | *d03* | *yes* | *yes* | 2.9762 | $2 \cdot 10^5$ |

Table 6.2: LC Resonators

Reso1 had only the design shown in section 6.2, without nanowire, in order to validate the HFSS simulations. Its full characterization is detailed in [104]. The Reso2 was made in a sample without NV centers with the finality of testing the nanowire resonator. The result was promising and thus we fabricated the resonator on top of the sample with long coherence time spins, *d03*. The resonators summary

is shown in Table 6.2. Now, we describe the microwave characterization of Reso3.

Since all the measurements are done in reflection, the characterization consists in a direct measurement of the S11 parameter. Fig. 6.5 shows the S11 power dependence data for input powers in the range of [-160, -131] dBm, increasing from the blue to the yellow. Two characteristics of this data are remarkable. 1) The resonance frequency is around 2.9762 instead of the simulated 3.02 GHz. This shift down in frequency of $\sim 44$ MHz it is due to the nanowire kinetic inductance. 2) The frequency shifts by increasing the microwave input power and its amplitude appears more and more deformed. That is a consequence of the non-linearity induced by the nanowire.

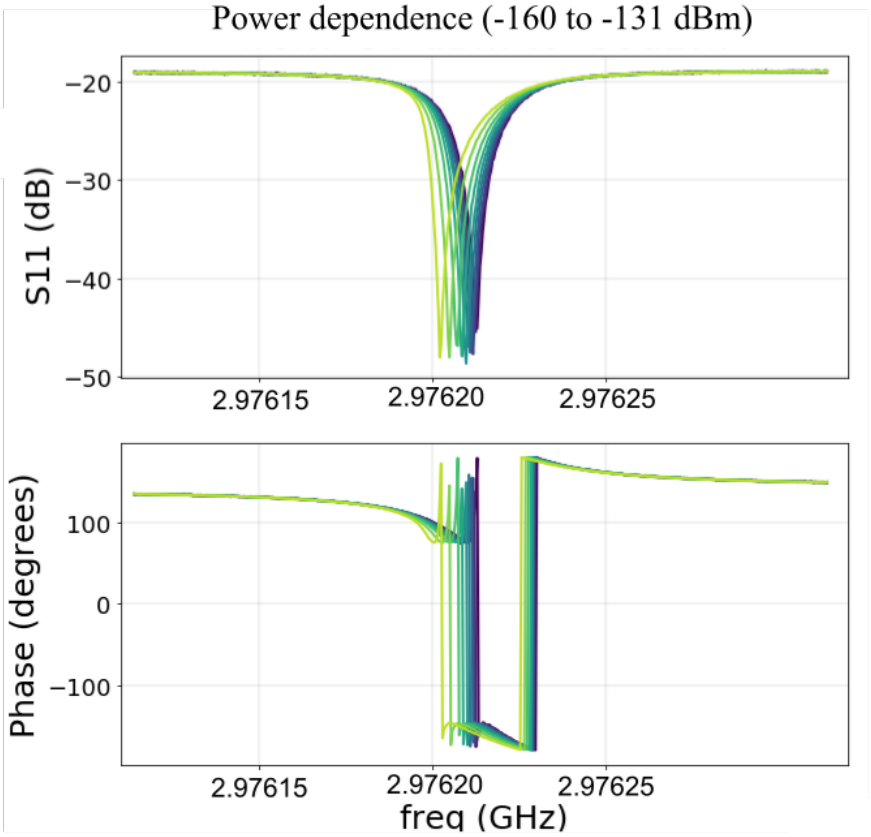


Figure 6.5: **Data.** Power dependence of S11 amplitude and phase at various input power.

### Internal losses

Fitting the data on Fig. 6.5 one can determines the resonator frequency as well as $\kappa_c$ and $\kappa_i$ (and therefore, $Q_c$ and $Q_i$). A complex plane curve fit is shown in Fig. 6.6 with an internal quality factor, $Q_i$, of $\sim 2 \cdot 10^5$.

The average intra-resonator photon number can be expressed as

$$\bar{n} = 4\kappa_c/(\hbar\omega_0(\kappa_c + \kappa_i)^2) \cdot PW \tag{6.3}$$

where PW is the input microwave power in W. Fig. 6.7 shows the $Q_i$, $Q_c$ and $Q_{total}$ dependence with the $\bar{n}$ and the microwave power input. It is remarkable the significant reduction of the $Q_i$ when measured powers corresponds to $\bar{n} \sim 1$. That is

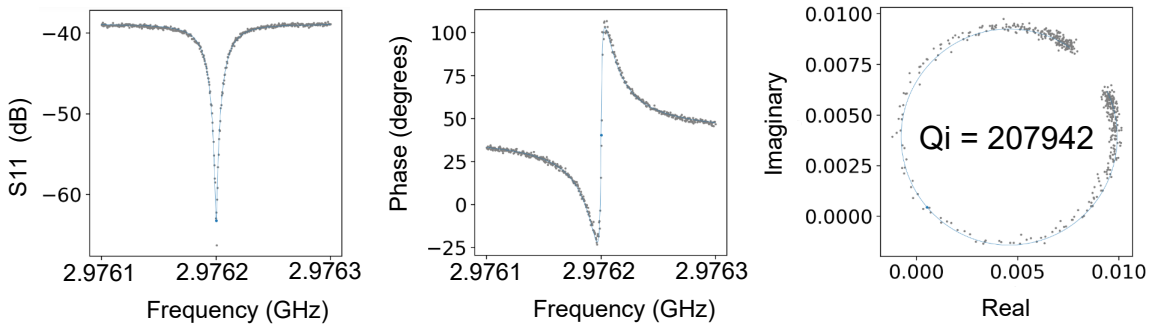


Figure 6.6: **Data Fit** to extract the resonator parameters $\omega_0, Q_i$ and $Q_c$

due to two levels systems (TLS) placed in the metal-substrate interface (dielectric losses). At higher powers the TLS saturates and thus the $Q_i$ presents a plateau. The low-power total loss rate is $\kappa = \omega_0/Q_{total} = 2 \cdot 10^5 s^{-1}$. Even if this is twice larger than the value considered in Chapter 2, we can say that our resonator is close to reaching the objective for single-spin detection.

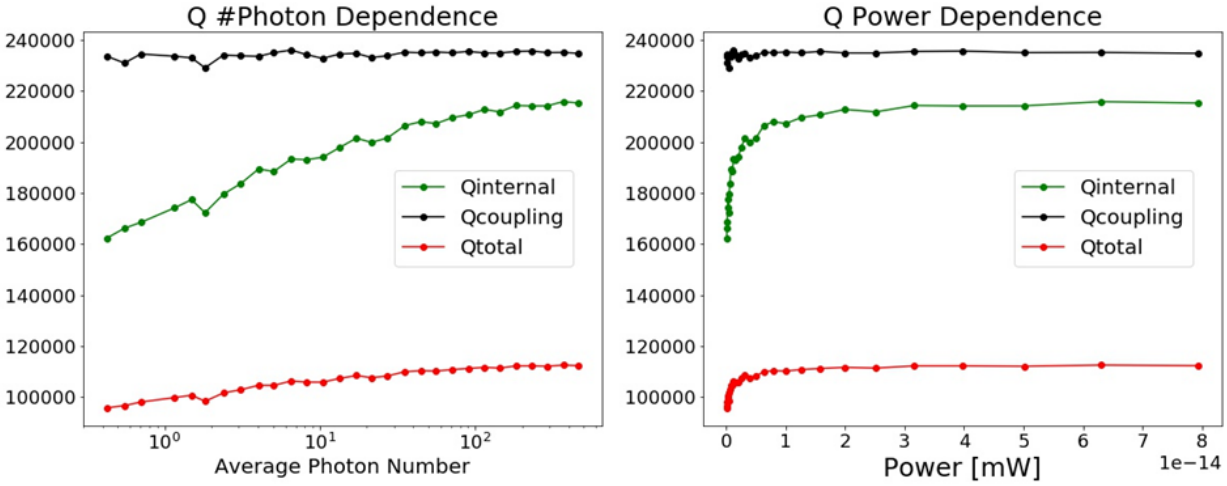


Figure 6.7: **Quality factor** as a function of the average photon number in the cavity (*left*) and its power dependence (*right*)

It is also interesting to point out the difference between the $Q_i$ measured in Reso1 and Reso3, Fig. 6.8, in which the design difference consists in the absence or in the presence of the nanowire, respectively. One possible Hypothesis to explain this behavior is that the bandage process causes additional losses, or that the presence of quasi-particles has a stronger effect in the nanowire resonator.

### Magnetic field dependence of the quality factor

In order to measure the NV centers, we need to tune them in resonance with $\omega_0$ by applying a magnetic field. To do so, we use the Helmholtz coils, Fig. 6.4c, to apply

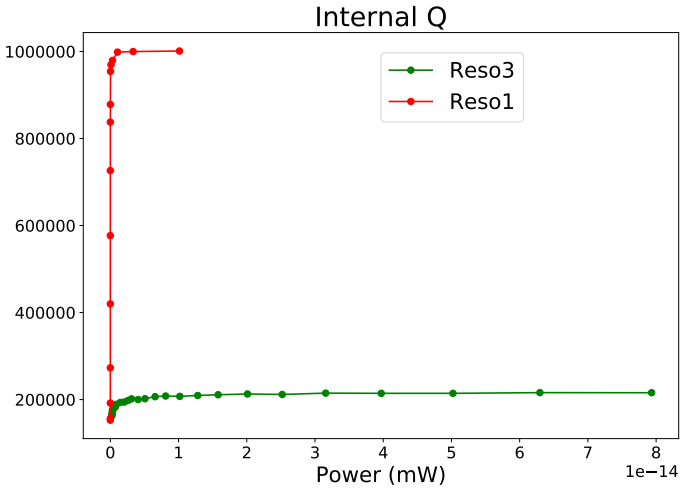


Figure 6.8: $Q_i$ Comparison between Reso1 and Reso3

a static magnetic field $\mathbf{B}_0$ parallel to the diamond surface, as discussed in Chapter 3, and the Al resonator remains superconductor. Assuming the Zeeman shift of the NV resonance in this conditions and the Reso3 $\omega_0/2\pi \sim 2.93GHz$, $\mathbf{B}_0$ has to be $\sim 3.1mT$ as shown in Fig. 6.9.

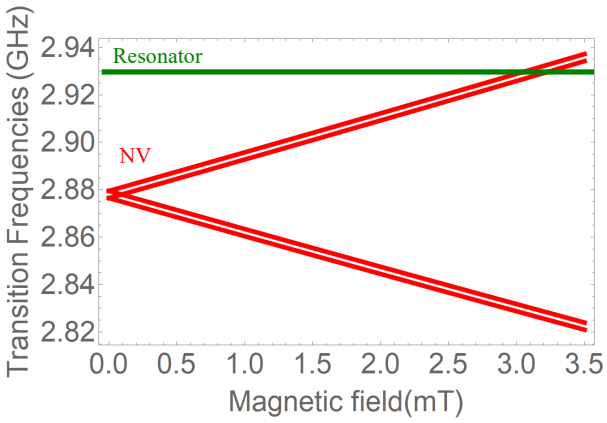


Figure 6.9: **Resonance tuning.** In red it is shown the NV transition frequencies as a function of the applied magnetic field. In Green the resonator frequency. The resonance is tuned at 3.1mT

Unfortunately, Reso3 did not behave as desired: instead of presenting a stable $Q_i$ as a function of $\mathbf{B}_0$ , it presents the behavior showed in Fig. 6.10: a drastic reduction of $Q_i$ after 1mT. That renders impossible proceed with the NV center measurements. We note that this behavior was not anticipated, as we have already applied larger magnetic fields to aluminum resonators (up to 10mT) without significant impact on $Q_i$.

This particular problem may be linked to remaining Josephson junctions in the bandage step, but more work is needed to identify the issue and solve it. Another option would be to turn to superconducting metals more resilient in field, such as

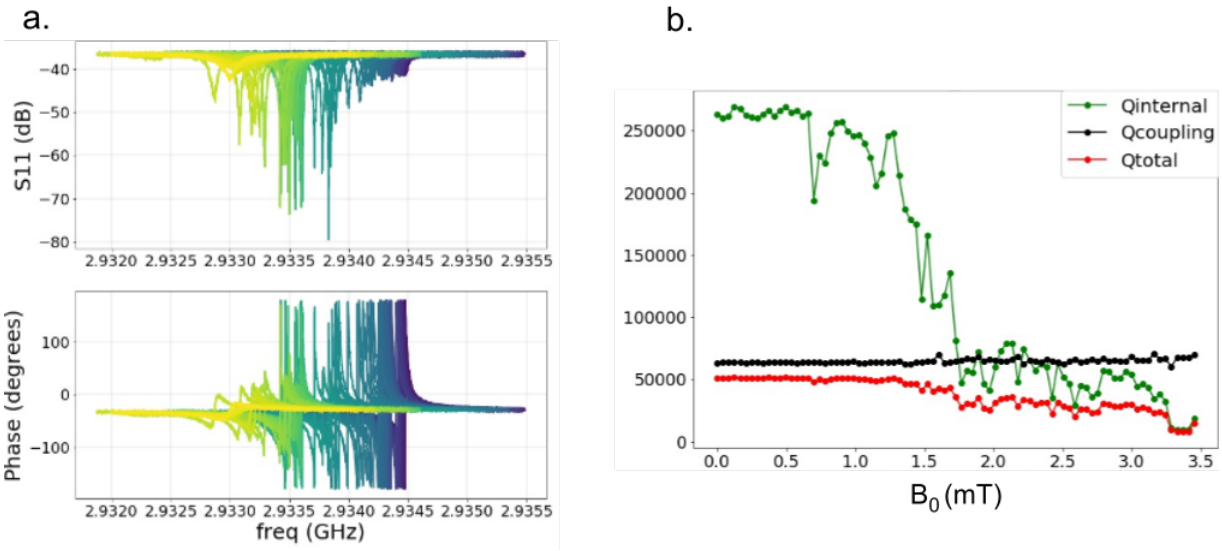


Figure 6.10: **Magnetic field resilience.** Left: power dependence of S11 amplitude and phase. Right: $Q_i$ (green), $Q_c$ (black) and $Q_t otal$ (red) of Reso3 as a function of the applied magnetic field $\mathbf{B}_0$

niobium, but we would need to find a way to protect the diamond surface, i.e. the shallow NV centers during niobium etching.

# Chapter 7

# Conclusions and perspectives

## 7.1 Actual state of the project

This thesis aimed at enhancing the sensitivity of Electron Paramagnetic Resonance spectroscopy up to the detection of a single electron spin, as proposed in [12]. In that goal, we need to enhance the spin-photon coupling, minimize the resonator losses, and use quantum-limited microwave amplifiers. All this can be achieved by combining superconducting quantum technologies with NV centers in diamond. With realistic estimates, measurement times on the order of a millisecond are achievable.

In order to maximize the spin-photon coupling, we propose to fabricate a superconducting resonator including a nanowire of lateral dimension $\sim 25nm$ right on top of a NV center in diamond. The precision of the alignment is essential for the success of the experiment.

The first task was to obtain an array of NV centers in diamond, well localized with respect to alignment marks etched in the sample, and with coherence times as long as $52\mu s$. This achievement is reported in Chapter 4.

In Chapter 5 we developed a process that allowed us to verify the NV-nanowire relative distance ($r_0$) using vector magnetometry, using the optical properties of the NV center at room temperature. We have reached $r_0 = 84$ nm with a precision of 10 nm in our measurements. Besides the interest on its own, this measurement indicated that the accuracy of our alignment was not sufficient for single-NV experiment. We therefore decided to turn to the measurement of a small ($\sim 10$) ensemble of implanted NV centers, which is more tolerant to alignment inaccuracy.

In Chapter 6 we performed the fabrication and characterization of a LC resonator of low impedance ($11\Omega$), internal quality factor as high as $Q_i = 2 \cdot 10^5$ and resonance frequency of $\sim 2.93$ GHz on top of such an ensemble of implanted NVs. Unfortunately, the resonator quality factor dropped when a magnetic field as low as 1mT was applied to the spins, which prevented us from seeing the desired signal as a field of 3.1mT was necessary.

## 7.2 Future directions

To continue the work presented in this thesis, the first obvious task will be to understand the origin of the poor magnetic field resilience displayed by our resonator. This may be related to the specific fabrication process that was developed. Once this problem is solved, it should become possible to detect the EPR signal coming from a small ensemble of $\sim 10$ implanted NV centers. This signal can be observed in microwave absorption, as proposed in Chapter 2, or also using pulse EPR spectroscopy based on Hahn echoes.

Single-spin signal could then be searched. One possible signature would be to observe quantum jumps of the nitrogen nuclear spins, which would be manifested by a telegraphic signal in the EPR spectroscopy. We hope that this can be observed in a near future, using the samples and tools developed in this thesis.

# Appendix A

## A.1 Fabrication Recipies

**Implantation Mask**

1. Diamond sample baked at 156° C for 1 min → to evaporate the water at the diamond surface
2. 950 PMMA type A3 resist (contain 3% of solids in Anisole) spin:
   - 2s, 500 rpm → to spread the spin
   - 60s, 5000 rpm → to get an homogeneous layer of 120 nm
   - 2s, 7000 rpm → reduce the border non-homogeneity
3. Aluminium layer of 20 nm → to avoid the charging effects during the e-beam lithography

**Resonator**

- **Substrate cleaning:** 3 hours in the Piranha acid mixture at 120°$C$ followed by hot acetone bath, IPA bath and Nitrogen blow;
- **Aluminum evaporation:** using the Plassy evaporator deposit 100 nm of Al at 1nm/s;
- **Optical lithography:** All the capacitive part of the resonator is fabricated in this step using the laser writer at ENS.
  - *Resist coating:* 500 nm of S1805 resist (single layer);
  - *Exposure:* first, the pattern is written at a nominal dose of D = 150mJ/cm$^2$; then a second exposure is done along the borders at dose = 3xD to ensure a proper lithography in this thicker resist
  - *Development:* 30s at AZ 726 MIF followed by a water bath and $N_2$ blow.
- **Al etching:** 50s immersed in Transene A at 40°$C$
- **E-beam lithography:** nanowire fabrication.
  - *Resist coating:* bi-layer PMGI-SF85 (400nm) - PMMA (50 nm) with a 12.5-nm-thck aluminium layer deposited by metal evaporation for charge evacuation during the e-beam lithography;

- *Exposure:* first, the nanowire is done at 30 keV and line dose = 2750 $\mu C/cm^2$; then the overlap zone is done with an area dose = 750 $\mu C/cm^2$
- *Development:* 10s in Transene A to remove the Al before developing the PMMA 45s with MIBK:IPA 1:3 mixture at room temperature. Rinse in IPA and $N_2$ blow. The PMGI-SF85, undercut, is developed with a mixture of CD26 : $H_20$ 3:2 for 20s at room temperature. Rinse in water and $N_2$ blow. All residual resist is removed using the Oxygen plasma for 1 min at pressure of 200$\mu bar$ and 50W.

- **Aluminum contact evaporation and liftoff:** 25nm of Al is deposited following by liftoff with remover PG at 60C (from 30-120 min).

- **Bandage:** responsable to the ohmic contact.
  - *Resist coating:* bi-layer PMGI-SF85 (400nm) - PMMA (350 nm);
  - *Exposure:* Large area (50 x 100 $\mu m$) with an area dose = 250 $\mu C/cm^2$
  - *Development:* of the PMMA 45s with MIBK:IPA 1:3 mixture at room temperature. Rinse in IPA and $N_2$ blow.
  - *Al evaporation:* deposited 160 nm of Al
  - *two-step liftoff:* First hot acetone for two hours, only PMMA A6 and aluminum should go away. The PMGI-SF85 layer should stay to protect the nanowire. Then, immerse the sample remover PG at 60C. followed by hot acetone (two hours), IPA bath and $N_2$ blow.

## A.2 Analytical expression of the magnetic field generated by infinite wire with rectangular cross section

$$F_x[p_0,z_0] = \frac{1}{2}\left(p_0 Log\left[1+\frac{t^2+2tz_0}{p_0^2+z_0^2}\right]+2(z_0+t)arctan\left[\frac{p_0}{(z_0+t)}\right]-2z_0 arctan\left[\frac{p_0}{z_0}\right]\right) \tag{A.1}$$

$$\begin{aligned} F_z[p_0,z_0] =& \frac{1}{2}\left(z_0 Log\left[1+\frac{p_0^2}{z_0^2}\right]-(z_0+t)Log\left[1+\frac{p_0^2}{(z_0+t)^2}\right]\right. \\ & \left. -2p_0\left(arctan\left[\frac{(z_0+t)}{p_0}\right]-arctan\left[\frac{z_0}{p_0}\right]\right)\right) \end{aligned} \tag{A.2}$$

$$B_x[x,z] = \gamma(F_x[w/2+x, z-t/2] - F_x[-w/2+x, z-t/2])$$

$$B_z[x,z] = \gamma(F_z[w/2+x, z-t/2] - F_z[-w/2+x, z-t/2])$$

where:

$$\gamma = \frac{\mu_0 j_{wire}}{2\pi}$$

$$j_{wire} = \frac{i_{wire}}{wt}$$

$$\mu_0 P = 4.0\pi 10^-7$$

## A.3 Vector magnetometry of NV2 and NV3

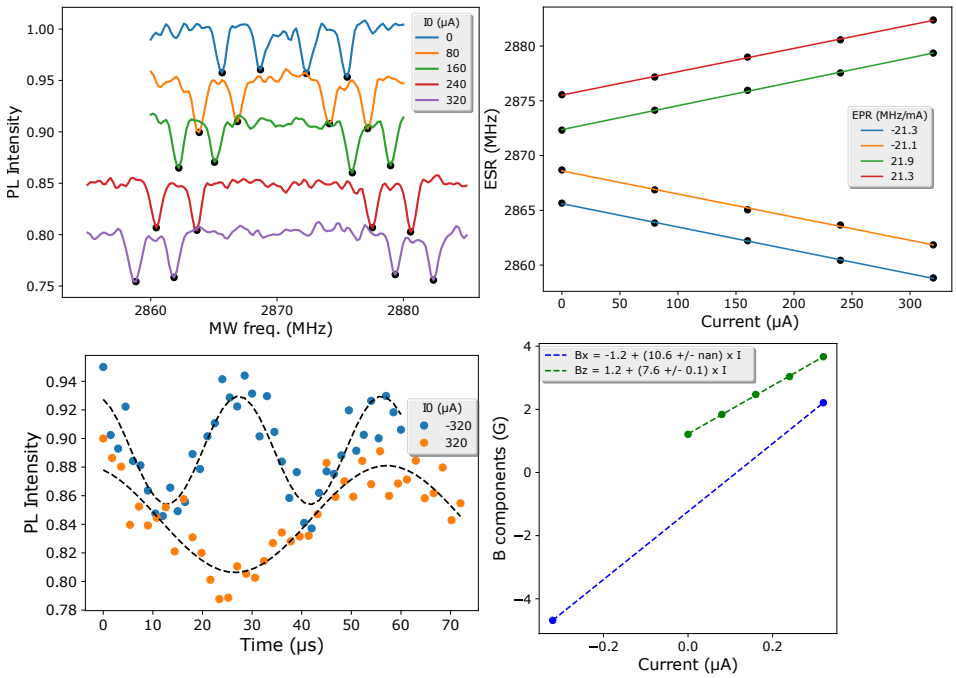


Figure A.1: **vector magnetometry of NV2** Data from chapter 5

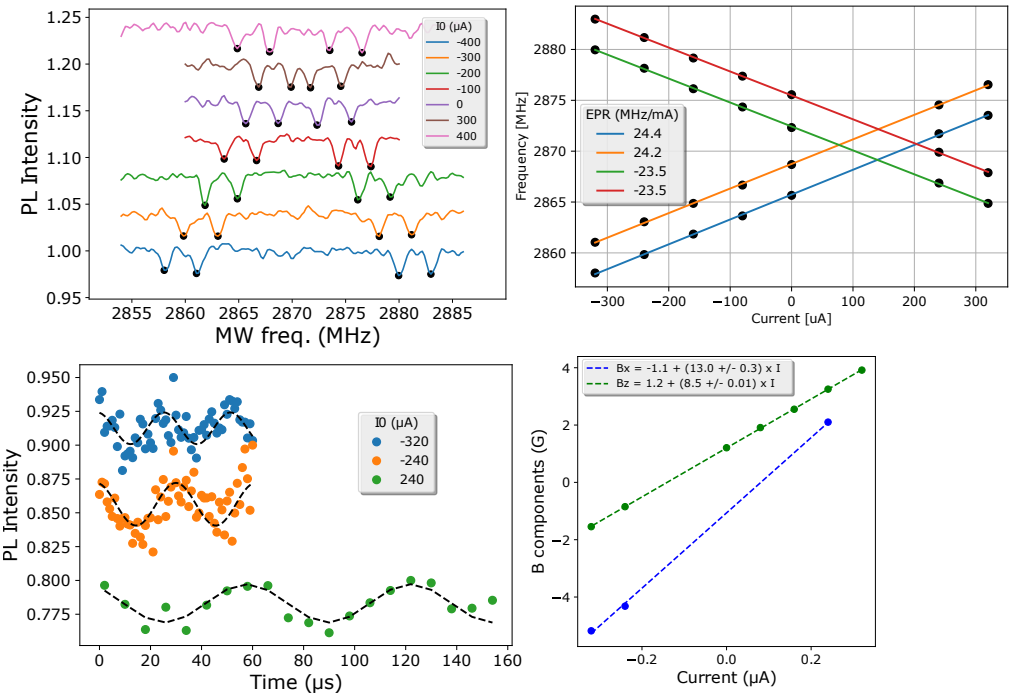


Figure A.2: **vector magnetometry of NV3** Data from chapter 5

# Bibliography


[1] A. Schweiger and G. Jeschke, *Principles of pulse electron paramagnetic resonance*. Oxford University Press on Demand, 2001.

[2] R. Narkowicz, D. Suter, and I. Niemeyer, "Scaling of sensitivity and efficiency in planar microresonators for electron spin resonance," *Review of Scientific Instruments*, vol. 79, no. 8, p. 084702, 2008.

[3] L. Shtirberg, Y. Twig, E. Dikarov, R. Halevy, M. Levit, and A. Blank, "High-sensitivity q-band electron spin resonance imaging system with submicron resolution," *Review of Scientific Instruments*, vol. 82, no. 4, p. 043708, 2011.

[4] Y. Kubo, I. Diniz, C. Grezes, T. Umeda, J. Isoya, H. Sumiya, T. Yamamoto, H. Abe, S. Onoda, T. Ohshima, *et al.*, "Electron spin resonance detected by a superconducting qubit," *Physical Review B*, vol. 86, no. 6, p. 064514, 2012.

[5] A. J. Sigillito, H. Malissa, A. M. Tyryshkin, H. Riemann, N. V. Abrosimov, P. Becker, H.-J. Pohl, M. L. Thewalt, K. M. Itoh, J. J. Morton, *et al.*, "Fast, low-power manipulation of spin ensembles in superconducting microresonators," *Applied Physics Letters*, vol. 104, no. 22, p. 222407, 2014.

[6] A. Bienfait, J. Pla, Y. Kubo, M. Stern, X. Zhou, C. Lo, C. Weis, T. Schenkel, M. Thewalt, D. Vion, *et al.*, "Reaching the quantum limit of sensitivity in electron spin resonance," *Nature nanotechnology*, vol. 11, no. 3, p. 253, 2016.

[7] A. Bienfait, P. Campagne-Ibarcq, A. Kiilerich, X. Zhou, S. Probst, J. Pla, T. Schenkel, D. Vion, D. Esteve, J. Morton, *et al.*, "Magnetic resonance with squeezed microwaves," *Physical Review X*, vol. 7, no. 4, p. 041011, 2017.

[8] C. Eichler, A. Sigillito, S. A. Lyon, and J. R. Petta, "Electron spin resonance at the level of 1 0 4 spins using low impedance superconducting resonators," *Physical review letters*, vol. 118, no. 3, p. 037701, 2017.

[9] M. H. Devoret and R. J. Schoelkopf, "Superconducting circuits for quantum information: an outlook," *Science*, vol. 339, no. 6124, pp. 1169–1174, 2013.

[10] X. Zhou, V. Schmitt, P. Bertet, D. Vion, W. Wustmann, V. Shumeiko, and D. Esteve, "High-gain weakly nonlinear flux-modulated josephson parametric amplifier using a squid array," *Physical Review B*, vol. 89, no. 21, p. 214517, 2014.

[11] A. Bienfait, *Magnetic resonance with quantum microwaves*. PhD thesis, 2016.

[12] P. Haikka, Y. Kubo, A. Bienfait, P. Bertet, and K. Mølmer, "Proposal for detecting a single electron spin in a microwave resonator," *Phys. Rev. A*, vol. 95, p. 022306, Feb 2017.

[13] S. Probst, A. Bienfait, P. Campagne-Ibarcq, J. Pla, B. Albanese, J. Da Silva Barbosa, T. Schenkel, D. Vion, D. Esteve, K. Mølmer, *et al.*, "Inductive-detection electron-spin resonance spectroscopy with 65 spins/hz sensitivity," *Applied Physics Letters*, vol. 111, no. 20, p. 202604, 2017.

[14] H. Malissa, D. Schuster, A. Tyryshkin, A. A. Houck, and S. A. Lyon, "Superconducting coplanar waveguide resonators for low temperature pulsed electron spin resonance spectroscopy," *Review of scientific instruments*, vol. 84, no. 2, p. 025116, 2013.

[15] Y. Twig, E. Dikarov, W. D. Hutchison, and A. Blank, "Note: High sensitivity pulsed electron spin resonance spectroscopy with induction detection," *Review of Scientific Instruments*, vol. 82, no. 7, p. 076105, 2011.

[16] A. Blank, E. Dikarov, R. Shklyar, and Y. Twig, "Induction-detection electron spin resonance with sensitivity of 1000 spins: En route to scalable quantum computations," *Physics Letters A*, vol. 377, no. 31-33, pp. 1937–1942, 2013.

[17] D. Rugar, R. Budakian, H. Mamin, and B. Chui, "Single spin detection by magnetic resonance force microscopy," *Nature*, vol. 430, no. 6997, pp. 329–332, 2004.

[18] A. Morello, J. J. Pla, F. A. Zwanenburg, K. W. Chan, K. Y. Tan, H. Huebl, M. Möttönen, C. D. Nugroho, C. Yang, J. A. van Donkelaar, *et al.*, "Single-shot readout of an electron spin in silicon," *Nature*, vol. 467, no. 7316, pp. 687–691, 2010.

[19] A. Gruber, A. Dräbenstedt, C. Tietz, L. Fleury, J. Wrachtrup, and C. v. Borczyskowski, "Scanning confocal optical microscopy and magnetic resonance on single defect centers," *Science*, vol. 276, no. 5321, pp. 2012–2014, 1997.

[20] C. Durkan and M. Welland, "Electronic spin detection in molecules using scanning-tunneling-microscopy-assisted electron-spin resonance," *Applied physics letters*, vol. 80, no. 3, pp. 458–460, 2002.

[21] A. R. Stegner, C. Boehme, H. Huebl, M. Stutzmann, K. Lips, and M. S. Brandt, "Electrical detection of coherent 31 p spin quantum states," *Nature Physics*, vol. 2, no. 12, pp. 835–838, 2006.

[22] C. Boehme and K. Lips, "Electrical detection of spin coherence in silicon," *Physical review letters*, vol. 91, no. 24, p. 246603, 2003.

[23] F. H. Koppens, C. Buizert, K.-J. Tielrooij, I. T. Vink, K. C. Nowack, T. Meunier, L. Kouwenhoven, and L. Vandersypen, "Driven coherent oscillations of a single electron spin in a quantum dot," *Nature*, vol. 442, no. 7104, pp. 766–771, 2006.

[24] J. Elzerman, R. Hanson, L. W. Van Beveren, B. Witkamp, L. Vandersypen, and L. P. Kouwenhoven, "Single-shot read-out of an individual electron spin in a quantum dot," *nature*, vol. 430, no. 6998, pp. 431–435, 2004.

[25] J. J. Pla, K. Y. Tan, J. P. Dehollain, W. H. Lim, J. J. Morton, D. N. Jamieson, A. S. Dzurak, and A. Morello, "A single-atom electron spin qubit in silicon," *Nature*, vol. 489, no. 7417, pp. 541–545, 2012.

[26] J. T. Muhonen, J. P. Dehollain, A. Laucht, F. E. Hudson, R. Kalra, T. Sekiguchi, K. M. Itoh, D. N. Jamieson, J. C. McCallum, A. S. Dzurak, *et al.*, "Storing quantum information for 30 seconds in a nanoelectronic device," *Nature nanotechnology*, vol. 9, no. 12, pp. 986–991, 2014.

[27] M. Xiao, I. Martin, E. Yablonovitch, and H. Jiang, "Electrical detection of the spin resonance of a single electron in a silicon field-effect transistor," *Nature*, vol. 430, no. 6998, pp. 435–439, 2004.

[28] R. Vincent, S. Klyatskaya, M. Ruben, W. Wernsdorfer, and F. Balestro, "Electronic read-out of a single nuclear spin using a molecular spin transistor," *Nature*, vol. 488, no. 7411, pp. 357–360, 2012.

[29] S. Thiele, F. Balestro, R. Ballou, S. Klyatskaya, M. Ruben, and W. Wernsdorfer, "Electrically driven nuclear spin resonance in single-molecule magnets," *Science*, vol. 344, no. 6188, pp. 1135–1138, 2014.

[30] J. Wrachtrup, C. Von Borczyskowski, J. Bernard, M. Orrit, and R. Brown, "Optical detection of magnetic resonance in a single molecule," *Nature*, vol. 363, no. 6426, p. 244, 1993.

[31] A. Sipahigil, K. D. Jahnke, L. J. Rogers, T. Teraji, J. Isoya, A. S. Zibrov, F. Jelezko, and M. D. Lukin, "Indistinguishable photons from separated silicon-vacancy centers in diamond," *Physical review letters*, vol. 113, no. 11, p. 113602, 2014.

[32] Y. Manassen, R. Hamers, J. Demuth, and A. Castellano Jr, "Direct observation of the precession of individual paramagnetic spins on oxidized silicon surfaces," *Physical review letters*, vol. 62, no. 21, p. 2531, 1989.

[33] Y. Manassen, I. Mukhopadhyay, and N. R. Rao, "Electron-spin-resonance stm on iron atoms in silicon," *Physical Review B*, vol. 61, no. 23, p. 16223, 2000.

[34] S. Baumann, W. Paul, T. Choi, C. P. Lutz, A. Ardavan, and A. J. Heinrich, "Electron paramagnetic resonance of individual atoms on a surface," *Science*, vol. 350, no. 6259, pp. 417–420, 2015.

[35] S. Müllegger, S. Tebi, A. K. Das, W. Schöfberger, F. Faschinger, and R. Koch, "Radio frequency scanning tunneling spectroscopy for single-molecule spin resonance," *Physical review letters*, vol. 113, no. 13, p. 133001, 2014.

[36] S. Haroche and J.-M. Raimond, *Exploring the Quantum*. Oxford University Press, 2006.

[37] E. L. Hahn, "Spin echoes," *Physical review*, vol. 80, no. 4, p. 580, 1950.

[38] B. W. Shore and P. L. Knight, "The jaynes-cummings model," *Journal of Modern Optics*, vol. 40, no. 7, pp. 1195–1238, 1993.

[39] E. M. Purcell, "Spontaneous transition probabilities in radio-frequency spectroscopy," *Phys. Rev*, vol. 69, p. 681, 1946.

[40] C. M. Caves, "Quantum limits on noise in linear amplifiers," *Physical Review D*, vol. 26, no. 8, p. 1817, 1982.

[41] B. Yurke, L. Corruccini, P. Kaminsky, L. Rupp, A. Smith, A. Silver, R. Simon, and E. Whittaker, "Observation of parametric amplification and deamplification in a josephson parametric amplifier," *Physical Review A*, vol. 39, no. 5, p. 2519, 1989.

[42] N. Bergeal, F. Schackert, M. Metcalfe, R. Vijay, V. Manucharyan, L. Frunzio, D. Prober, R. Schoelkopf, S. Girvin, and M. Devoret, "Phase-preserving amplification near the quantum limit with a josephson ring modulator," *Nature*, vol. 465, no. 7294, pp. 64–68, 2010.

[43] L. Du Preez, *Electron paramagnetic resonance and optical investigations of defect centres in diamond*. PhD thesis, University of the Witwatersrand, Johannesburg, 1965.

[44] A. Gruber, A. Dräbenstedt, C. Tietz, L. Fleury, J. Wrachtrup, and C. Von Borczyskowski, "Scanning confocal optical microscopy and magnetic resonance on single defect centers," *Science*, vol. 276, no. 5321, pp. 2012–2014, 1997.

[45] R. Brouri, A. Beveratos, J.-P. Poizat, and P. Grangier, "Photon antibunching in the fluorescence of individual color centers in diamond," *Optics letters*, vol. 25, no. 17, pp. 1294–1296, 2000.

[46] C. Kurtsiefer, S. Mayer, P. Zarda, and H. Weinfurter, "Stable solid-state source of single photons," *Physical review letters*, vol. 85, no. 2, p. 290, 2000.

[47] P. G. Baranov, H. J. Von Bardeleben, F. Jelezko, and J. Wrachtrup, *Magnetic resonance of semiconductors and their nanostructures*. Springer, 2017.

[48] G. Balasubramanian, P. Neumann, D. Twitchen, M. Markham, R. Kolesov, N. Mizuochi, J. Isoya, J. Achard, J. Beck, J. Tissler, V. Jacques, P. R. Hemmer, F. Jelezko, and J. Wrachtrup, "Ultralong spin coherence time in isotopically engineered diamond," *Nature Materials*, vol. 8, pp. 383–387, May 2009.

[49] L. Childress and R. Hanson, "Diamond NV centers for quantum computing and quantum networks," *MRS Bulletin*, vol. 38, pp. 134–138, Feb. 2013.

[50] T. Gaebel, M. Domhan, I. Popa, C. Wittmann, P. Neumann, F. Jelezko, J. R. Rabeau, N. Stavrias, A. D. Greentree, S. Prawer, J. Meijer, J. Twamley, P. R. Hemmer, and J. Wrachtrup, "Room-temperature coherent coupling of single spins in diamond," *Nature Phys*, vol. 2, pp. 408–413, June 2006.

[51] M. G. Dutt, L. Childress, L. Jiang, E. Togan, J. Maze, F. Jelezko, A. Zibrov, P. Hemmer, and M. Lukin, "Quantum register based on individual electronic and nuclear spin qubits in diamond," *Science*, vol. 316, no. 5829, pp. 1312–1316, 2007.

[52] P. Neumann, N. Mizuochi, F. Rempp, P. Hemmer, H. Watanabe, S. Yamasaki, V. Jacques, T. Gaebel, F. Jelezko, and J. Wrachtrup, "Multipartite entanglement among single spins in diamond," *science*, vol. 320, no. 5881, pp. 1326–1329, 2008.

[53] L. Jiang, J. Hodges, J. Maze, P. Maurer, J. Taylor, D. Cory, P. Hemmer, R. L. Walsworth, A. Yacoby, A. S. Zibrov, *et al.*, "Repetitive readout of a single electronic spin via quantum logic with nuclear spin ancillae," *Science*, vol. 326, no. 5950, pp. 267–272, 2009.

[54] H. Bernien, B. Hensen, W. Pfaff, G. Koolstra, M. S. Blok, L. Robledo, T. H. Taminiau, M. Markham, D. J. Twitchen, L. Childress, and R. Hanson, "Heralded entanglement between solid-state qubits separated by three metres," *Nature*, vol. 497, pp. 86–90, May 2013.

[55] Y. Kubo, F. R. Ong, P. Bertet, D. Vion, V. Jacques, D. Zheng, A. Dréau, J.-F. Roch, A. Auffeves, F. Jelezko, J. Wrachtrup, M. F. Barthe, P. Bergonzo, and D. Esteve, "Strong Coupling of a Spin Ensemble to a Superconducting Resonator," *Phys. Rev. Lett.*, vol. 105, p. 140502, Sept. 2010.

[56] C. L. Degen, "Scanning magnetic field microscope with a diamond single-spin sensor," *Appl. Phys. Lett.*, vol. 92, p. 243111, June 2008.

[57] J. R. Maze, P. L. Stanwix, J. S. Hodges, S. Hong, J. M. Taylor, P. Cappellaro, L. Jiang, M. V. G. Dutt, E. Togan, A. S. Zibrov, A. Yacoby, R. L. Walsworth, and M. D. Lukin, "Nanoscale magnetic sensing with an individual electronic spin in diamond," *Nature*, vol. 455, pp. 644–647, Oct. 2008.

[58] J. M. Taylor, P. Cappellaro, L. Childress, L. Jiang, D. Budker, P. R. Hemmer, A. Yacoby, R. Walsworth, and M. D. Lukin, "High-sensitivity diamond magnetometer with nanoscale resolution," *Nature Phys*, vol. 4, pp. 810–816, Oct. 2008.

[59] T. Staudacher, F. Shi, S. Pezzagna, J. Meijer, J. Du, C. A. Meriles, F. Reinhard, and J. Wrachtrup, "Nuclear Magnetic Resonance Spectroscopy on a (5-Nanometer)3 Sample Volume," *Science*, vol. 339, pp. 561–563, Feb. 2013.

[60] N. Aslam, M. Pfender, P. Neumann, R. Reuter, A. Zappe, F. F. d. Oliveira, A. Denisenko, H. Sumiya, S. Onoda, J. Isoya, and J. Wrachtrup, "Nanoscale nuclear magnetic resonance with chemical resolution," *Science*, vol. 357, pp. 67–71, July 2017.

[61] J.-P. Tetienne, T. Hingant, J.-V. Kim, L. H. Diez, J.-P. Adam, K. Garcia, J.-F. Roch, S. Rohart, A. Thiaville, D. Ravelosona, and V. Jacques, "Nanoscale imaging and control of domain-wall hopping with a nitrogen-vacancy center microscope," *Science*, vol. 344, pp. 1366–1369, June 2014.

[62] L. Thiel, D. Rohner, M. Ganzhorn, P. Appel, E. Neu, B. Müller, R. Kleiner, D. Koelle, and P. Maletinsky, "Quantitative nanoscale vortex imaging using a cryogenic quantum magnetometer," *Nature Nanotechnology*, vol. 11, pp. 677–681, Aug. 2016.

[63] I. Gross, W. Akhtar, V. Garcia, L. J. Martínez, S. Chouaieb, K. Garcia, C. Carrétéro, A. Barthélémy, P. Appel, P. Maletinsky, J.-V. Kim, J. Y. Chauleau, N. Jaouen, M. Viret, M. Bibes, S. Fusil, and V. Jacques, "Real-space imaging of non-collinear antiferromagnetic order with a single-spin magnetometer," *Nature*, vol. 549, pp. 252–256, Sept. 2017.

[64] L. Thiel, Z. Wang, M. A. Tschudin, D. Rohner, I. Gutiérrez-Lezama, N. Ubrig, M. Gibertini, E. Giannini, A. F. Morpurgo, and P. Maletinsky, "Probing magnetism in 2D materials at the nanoscale with single-spin microscopy," *Science*, vol. 364, pp. 973–976, June 2019.

[65] E. Togan, Y. Chu, A. S. Trifonov, L. Jiang, J. Maze, L. Childress, M. V. G. Dutt, A. S. Sorensen, P. R. Hemmer, A. S. Zibrov, and M. D. Lukin, "Quantum entanglement between an optical photon and a solid-state spin qubit," *Nature*, vol. 466, no. 7307, pp. 730–734, 2010.

[66] N. Kalb, A. A. Reiserer, P. C. Humphreys, J. J. W. Bakermans, S. J. Kamerling, N. H. Nickerson, S. C. Benjamin, D. J. Twitchen, M. Markham, and R. Hanson, "Entanglement distillation between solid-state quantum network nodes," *Science*, vol. 356, pp. 928–932, June 2017.

[67] S. Wehner, D. Elkouss, and R. Hanson, "Quantum internet: A vision for the road ahead," *Science*, vol. 362, Oct. 2018.

[68] A. M. Zaitsev, *Optical properties of diamond: a data handbook*. Springer Science & Business Media, 2013.

[69] J. R. Maze, A. Gali, E. Togan, Y. Chu, A. Trifonov, E. Kaxiras, and M. D. Lukin, "Properties of nitrogen-vacancy centers in diamond: the group theoretic approach," *New Journal of Physics*, vol. 13, no. 2, p. 025025, 2011.

[70] A. Dréau, *Spins individuels dans le diamant pour l'information quantique*. thesis, Cachan, Ecole normale supérieure, Dec. 2013.

[71] A. Dréau, M. Lesik, L. Rondin, P. Spinicelli, O. Arcizet, J.-F. Roch, and V. Jacques, "Avoiding power broadening in optically detected magnetic resonance of single nv defects for enhanced dc magnetic field sensitivity," *Physical Review B*, vol. 84, no. 19, p. 195204, 2011.

[72] F. Jelezko, T. Gaebel, I. Popa, A. Gruber, and J. Wrachtrup, "Observation of coherent oscillations in a single electron spin," *Physical review letters*, vol. 92, no. 7, p. 076401, 2004.

[73] P. Jamonneau, M. Lesik, J. Tetienne, I. Alvizu, L. Mayer, A. Dréau, S. Kosen, J.-F. Roch, S. Pezzagna, J. Meijer, *et al.*, "Competition between electric field and magnetic field noise in the decoherence of a single spin in diamond," *Physical Review B*, vol. 93, no. 2, p. 024305, 2016.

[74] X.-D. Chen, F.-W. Sun, C.-L. Zou, J.-M. Cui, L.-M. Zhou, and G.-C. Guo, "Vector magnetic field sensing by a single nitrogen vacancy center in diamond," *EPL*, vol. 101, p. 67003, Mar. 2013.

[75] S. Hong, M. S. Grinolds, L. M. Pham, D. Le Sage, L. Luan, R. L. Walsworth, and A. Yacoby, "Nanoscale magnetometry with nv centers in diamond," *MRS bulletin*, vol. 38, no. 2, p. 155, 2013.

[76] G. Balasubramanian, I. Y. Chan, R. Kolesov, M. Al-Hmoud, J. Tisler, C. Shin, C. Kim, A. Wojcik, P. R. Hemmer, A. Krueger, T. Hanke, A. Leitenstorfer, R. Bratschitsch, F. Jelezko, and J. Wrachtrup, "Nanoscale imaging magnetometry with diamond spins under ambient conditions," *Nature*, vol. 455, pp. 648–651, Oct. 2008.

[77] P. Maletinsky, S. Hong, M. S. Grinolds, B. Hausmann, M. D. Lukin, R. L. Walsworth, M. Loncar, and A. Yacoby, "A robust scanning diamond sensor for nanoscale imaging with single nitrogen-vacancy centres," *Nature Nanotech*, vol. 7, pp. 320–324, May 2012.

[78] V. M. Acosta, E. Bauch, A. Jarmola, L. J. Zipp, M. P. Ledbetter, and D. Budker, "Broadband magnetometry by infrared-absorption detection of nitrogen-vacancy ensembles in diamond," *Appl. Phys. Lett.*, vol. 97, p. 174104, Oct. 2010.

[79] N. Zhao, S.-W. Ho, and R.-B. Liu, "Decoherence and dynamical decoupling control of nitrogen vacancy center electron spins in nuclear spin baths," *Physical Review B*, vol. 85, no. 11, p. 115303, 2012.

[80] R. Hanson, V. Dobrovitski, A. Feiguin, O. Gywat, and D. Awschalom, "Coherent dynamics of a single spin interacting with an adjustable spin bath," *Science*, vol. 320, no. 5874, pp. 352–355, 2008.

[81] G. de Lange, T. van der Sar, M. Blok, Z.-H. Wang, V. Dobrovitski, and R. Hanson, "Controlling the quantum dynamics of a mesoscopic spin bath in diamond," *Scientific Reports*, vol. 2, p. 382, Apr. 2012.

[82] N. Mizuochi, P. Neumann, F. Rempp, J. Beck, V. Jacques, P. Siyushev, K. Nakamura, D. J. Twitchen, H. Watanabe, S. Yamasaki, F. Jelezko, and J. Wrachtrup, "Coherence of single spins coupled to a nuclear spin bath of varying density," *Phys. Rev. B*, vol. 80, p. 041201, July 2009.

[83] G. Balasubramanian, P. Neumann, D. Twitchen, M. Markham, R. Kolesov, N. Mizuochi, J. Isoya, J. Achard, J. Beck, J. Tissler, *et al.*, "Ultralong spin coherence time in isotopically engineered diamond," *Nature materials*, vol. 8, no. 5, p. 383, 2009.

[84] B. A. Myers, A. Das, M. C. Dartiailh, K. Ohno, D. D. Awschalom, and A. C. Bleszynski Jayich, "Probing Surface Noise with Depth-Calibrated Spins in Diamond," *Phys. Rev. Lett.*, vol. 113, p. 027602, July 2014.

[85] M. Hauf, B. Grotz, B. Naydenov, M. Dankerl, S. Pezzagna, J. Meijer, F. Jelezko, J. Wrachtrup, M. Stutzmann, F. Reinhard, *et al.*, "Chemical control of the charge state of nitrogen-vacancy centers in diamond," *Physical Review B*, vol. 83, no. 8, p. 081304, 2011.

[86] J. Wrachtrup, F. Jelezko, B. Grotz, and L. McGuinness, "Nitrogen-vacancy centers close to surfaces," *MRS bulletin*, vol. 38, no. 2, p. 149, 2013.

[87] J. Meijer, S. Pezzagna, T. Vogel, B. Burchard, H. Bukow, I. Rangelow, Y. Sarov, H. Wiggers, I. Plümel, F. Jelezko, J. Wrachtrup, F. Schmidt-Kaler, W. Schnitzler, and K. Singer, "Towards the implanting of ions and positioning of nanoparticles with nm spatial resolution," *Appl. Phys. A*, vol. 91, pp. 567–571, June 2008.

[88] S. Pezzagna, D. Wildanger, P. Mazarov, A. D. Wieck, Y. Sarov, I. Rangelow, B. Naydenov, F. Jelezko, S. W. Hell, and J. Meijer, "Nanoscale Engineering and Optical Addressing of Single Spins in Diamond," *Small*, vol. 6, pp. 2117–2121, Oct. 2010.

[89] D. M. Toyli, C. D. Weis, G. D. Fuchs, T. Schenkel, and D. D. Awschalom, "Chip-Scale Nanofabrication of Single Spins and Spin Arrays in Diamond," *Nano Lett.*, vol. 10, pp. 3168–3172, Aug. 2010.

[90] D. Scarabelli, M. Trusheim, O. Gaathon, D. Englund, and S. J. Wind, "Nanoscale Engineering of Closely-Spaced Electronic Spins in Diamond," *Nano Lett.*, vol. 16, pp. 4982–4990, Aug. 2016.

[91] M. Lesik, P. Spinicelli, S. Pezzagna, P. Happel, V. Jacques, O. Salord, B. Rasser, A. Delobbe, P. Sudraud, A. Tallaire, J. Meijer, and J.-F. Roch, "Maskless and targeted creation of arrays of colour centres in diamond using focused ion beam technology," *physica status solidi (a)*, vol. 210, no. 10, pp. 2055–2059, 2013.

[92] J. Rabeau, P. Reichart, G. Tamanyan, D. Jamieson, S. Prawer, F. Jelezko, T. Gaebel, I. Popa, M. Domhan, and J. Wrachtrup, "Implantation of labelled single nitrogen vacancy centers in diamond using n 15," *Applied Physics Letters*, vol. 88, no. 2, p. 023113, 2006.

[93] S. Pezzagna, B. Naydenov, F. Jelezko, J. Wrachtrup, and J. Meijer, "Creation efficiency of nitrogen-vacancy centres in diamond," *New Journal of Physics*, vol. 12, no. 6, p. 065017, 2010.

[94] S. Sangtawesin, B. L. Dwyer, S. Srinivasan, J. J. Allred, L. V. Rodgers, K. De Greve, A. Stacey, N. Dontschuk, K. M. O'Donnell, D. Hu, *et al.*, "Origins of diamond surface noise probed by correlating single-spin measurements with surface spectroscopy," *Physical Review X*, vol. 9, no. 3, p. 031052, 2019.

[95] J. da Silva Barbosa, M. Lee, P. Campagne-Ibarcq, P. Jamonneau, Y. Kubo, S. Pezzagna, J. Meijer, T. Teraji, D. Vion, D. Esteve, *et al.*, "Determining the position of a single spin relative to a metallic nanowire," *Journal of Applied Physics*, vol. 129, no. 14, p. 144301, 2021.

[96] C. Song, M. P. DeFeo, K. Yu, and B. L. Plourde, "Reducing microwave loss in superconducting resonators due to trapped vortices," *Applied Physics Letters*, vol. 95, no. 23, p. 232501, 2009.

[97] R. Barends, J. Wenner, M. Lenander, Y. Chen, R. C. Bialczak, J. Kelly, E. Lucero, P. O'Malley, M. Mariantoni, D. Sank, *et al.*, "Minimizing quasiparticle generation from stray infrared light in superconducting quantum circuits," *Applied Physics Letters*, vol. 99, no. 11, p. 113507, 2011.

[98] A. D. O'Connell, M. Ansmann, R. C. Bialczak, M. Hofheinz, N. Katz, E. Lucero, C. McKenney, M. Neeley, H. Wang, E. M. Weig, *et al.*, "Microwave dielectric loss at single photon energies and millikelvin temperatures," *Applied Physics Letters*, vol. 92, no. 11, p. 112903, 2008.

[99] D. S. Wisbey, J. Gao, M. R. Vissers, F. C. da Silva, J. S. Kline, L. Vale, and D. P. Pappas, "Effect of metal/substrate interfaces on radio-frequency loss in superconducting coplanar waveguides," *Journal of Applied Physics*, vol. 108, no. 9, p. 093918, 2010.

[100] A. Houck, J. Schreier, B. Johnson, J. Chow, J. Koch, J. Gambetta, D. Schuster, L. Frunzio, M. Devoret, S. Girvin, *et al.*, "Controlling the spontaneous emission of a superconducting transmon qubit," *Physical review letters*, vol. 101, no. 8, p. 080502, 2008.

[101] J. De Vries, "Temperature and thickness dependence of the resistivity of thin polycrystalline aluminium, cobalt, nickel, palladium, silver and gold films," *Thin Solid Films*, vol. 167, no. 1-2, pp. 25–32, 1988.

[102] A. Ferguson, R. Clark, *et al.*, "Energy gap measurement of nanostructured aluminium thin films for single cooper-pair devices," *Superconductor Science and Technology*, vol. 21, no. 1, p. 015013, 2007.

[103] L. Grünhaupt, U. von Lüpke, D. Gusenkova, S. T. Skacel, N. Maleeva, S. Schlör, A. Bilmes, H. Rotzinger, A. V. Ustinov, M. Weides, *et al.*, "An argon ion beam milling process for native alox layers enabling coherent superconducting contacts," *Applied Physics Letters*, vol. 111, no. 7, p. 072601, 2017.

[104] M. Lee, "Ultrahigh-quality-factor superconducting microwave resonator on diamond for quantum information processing," *Japanese Journal of Applied Physics*, vol. 58, no. 10, p. 100914, 2019.

université PARIS-SACLAY

ÉCOLE DOCTORALE
Physique en l'Île-de-France (PIF)

**Titre:** Fabrication et caractérisation d'un dispositif quantique hybride pour la détection micro-onde à simple spin

**Mots clés :** Centre NV dans le diamant, magnétométrie vectorielle, dispositif quantique hybride

**Résumé :** Le contexte de cette thèse est une proposition théorique par Haikka et al [1] qui vise à détecter des spins individuels avec des micro-ondes, en utilisant un micro-résonateur supraconducteur incorporant une constriction nanométrique proche du spin, refroidi au millikelvin. Les spins utilisés sont des centres NV du diamant, implantés à une faible profondeur (20nm) dans un échantillon de diamant purifié isotopiquement en $^{12}$C. Sa fréquence de transition est $\sim 2.88$ GHz. Nous démontrons la fabrication d'une grille de NV unique avec de longs temps de cohérence et bien localisée par rapport aux marques d'alignement gravées dans le diamant. Nous démontrons une méthode pour déterminer la position de centres NV par rapport à un nanofil métallique déposé sur du diamant. Nous utilisons le centre NV comme magnétomètre vectoriel [2, 3] pour mesurer le champ généré par le passage d'un courant continu à travers le fil, permettant d'inférer la position des centres NV par rapport au fil avec une précision de ~ 10 nm.

Nous avons fabriqué et réalisé la caractérisation d'un résonateur LC de faible impédance 11Ω, d'un facteur de qualité interne atteignant $2.10^5$ et d'une fréquence de résonance d'environ 2,93 GHz au-dessus d'un tel ensemble de NV implantés.
La résistance en champ magnétique de ce résonateur n'a cependant pas été suffisante pour voir le signal de spin.

[1] P. Haikka, Y. Kubo, A. Bienfait, P. Bertet, and K. Mølmer, "Proposal for detecting a single electron spin in a microwave resonator,"Phys. Rev. A, vol. 95,p. 022306, Feb 2017.
[2] J. M. Taylor, P. Cappellaro, L. Childress, L. Jiang, D. Budker, P. R. Hemmer, A. Yacoby,R. Walsworth, and M. D. Lukin, "High-sensitivity diamond magnetometer with nanoscaleresolution,"Nature Phys, vol. 4, pp. 810–816, Oct. 2008.
[3] X.-D. Chen, F.-W. Sun, C.-L. Zou, J.-M. Cui, L.-M. Zhou, and G.-C. Guo, "Vector magneticfield sensing by a single nitrogen vacancy center in diamond,"EPL, vol. 101, p. 67003, Mar.2013.

**Title:** Fabrication and characterization of a hybrid quantum device for single spin microwave detection

**Keywords :** NV center in diamond, vectorial magnetometry, hybrid quantum device

**Abstract :** The context of this thesis is a proposal by Haikka et al. [1] that aims at detecting individual spins with microwaves, using a superconducting micro-resonator that incorporates a nanometric constriction located close to the spin, cooled down to millikelvin temperatures. The electron spins of choice are shallow implanted $\sim 20\,nm$ depth single Nitrogen - Vacancy (NV) centers in an isotopically purified $^{12}$C diamond. Their transition frequency is $\sim 2.88$ GHz We report the fabrication of a single NV center grid with long coherence times and well localized with respect to alignment marks etched in the diamond. We demonstrate a method to determine the position of shallow individual implanted nitrogen-vacancy (NV) centers with respect to a metallic nanowire deposited on diamond. We use the NV center as a vector magnetometer [2, 3] to measure the field generated by passing a DC current through the wire, enabling to infer the NV centers position relative to the wire with a precision of $\sim 10\,nm$.

We fabricated and performed the characterization of a LC resonator of low impedance 11Ω, internal quality factor as high as $2.10^5$ and resonance frequency of $\sim$ 2.93 GHz on top of such an ensemble of implanted NVs. The magnetic field resilience of the resonator was however not sufficient to observe the spin signal.

[1] P. Haikka, Y. Kubo, A. Bienfait, P. Bertet, and K. Mølmer, "Proposal for detecting a single electron spin in a microwave resonator,"Phys. Rev. A, vol. 95,p. 022306, Feb 2017.
[2] J. M. Taylor, P. Cappellaro, L. Childress, L. Jiang, D. Budker, P. R. Hemmer, A. Yacoby,R. Walsworth, and M. D. Lukin, "High-sensitivity diamond magnetometer with nanoscaleresolution,"Nature Phys, vol. 4, pp. 810–816, Oct. 2008.
[3] X.-D. Chen, F.-W. Sun, C.-L. Zou, J.-M. Cui, L.-M. Zhou, and G.-C. Guo, "Vector magneticfield sensing by a single nitrogen vacancy center in diamond,"EPL, vol. 101, p. 67003, Mar.2013

**Université Paris-Saclay**
Espace Technologique / Immeuble Discovery
Route de l'Orme aux Merisiers RD 128 / 91190 Saint-Aubin, France